Ph.D. Dissertation

Measurement of angular and momentum distributions in multi-jet final states at $\sqrt{s} = 8$ TeV and 13 TeV at the LHC

by

Hyunyong Kim

Department of Physics

The Graduate School of the University of Seoul

August 2018

Measurement of angular and momentum distributions in multi-jet final states at $\sqrt{s} = 8$ TeV and 13 TeV at the LHC

by

Hyunyong Kim

A Ph.D. Dissertation submitted to the Department of Physics at the Graduate School of the University of Seoul in partial fulfillment of the requirements for the degree of Doctor of Philosophy

June 2018

Approved by

Inkyu Park

Advisor

This certifies that Ph.D. Dissertation of Hyunyong Kim is approved.

Thesis Committee Chair: Hyunsoo Min

Thesis Committee Member: Inkyu Park

Thesis Committee Member: Jason Sang Hun Lee

Thesis Committee Member: Suyong choi

Thesis Committee Member: Hyunsoo Kim

The Graduate School of the University of Seoul

June 2018

Abstract

Measurement of angular and momentum distributions in multi-jet final states at $\sqrt{s} = 8$ TeV and 13 TeV at the LHC

We study two kinematic observables that test jet correlations using multi-jet events collected in pp collisions at the LHC. Using events with three or more jets, we study the ratio of the transverse momentum of the third jet to the second jet and the angular separation between the second and third jet. The data are compared to theoretical predictions from event generators. The measurements use 19.8 fb^{-1} and 2.29 fb^{-1} of data collected by the CMS experiment at the center-of-mass energies of 8 TeV and 13 TeV, respectively.

Keyword: LHC, CMS, QCD, jet, QCD coherence

Ph.D. Dissertation

Measurement of angular and momentum distributions in multi-jet final states at $\sqrt{s} = 8$ TeV and 13 TeV at the LHC

by

Hyunyong Kim

Department of Physics

The Graduate School of the University of Seoul

August 2018

Contents

Abstract

Contents **i**

List of Figures **iii**

List of Tables **xvi**

1. Introduction and Literature Review **1**

2. QCD Coherence **9**

2.1 Angular Ordering 9
2.2 The Lund Model 11
2.3 Color Coherence 13
2.4 MC updates on color coherence at $\sqrt{s} = 7\,\text{TeV}$ 17
2.5 New Motivation 24

3. CERN LHC and CMS Experiment **29**

3.1 LHC 29
3.2 CMS 33

4. Event Selection **37**

4.1 Data Samples 37
4.1.1 Data and MC sets for $\sqrt{s} = 8$ TeV 38
4.1.2 Data and MC sets for $\sqrt{s} = 13$ TeV 39

4.2 Jet reconstruction and event selection 41

5. Detector effects: Data Unfolding 47

5.1 Detector level comparison 47

5.1.1 $\sqrt{s} = 8$ TeV 48

5.1.2 $\sqrt{s} = 13$ TeV 59

5.2 Unfolding 70

5.2.1 Response matrix 70

5.2.2 Purity, stability, acceptance, and background 73

5.2.3 Iteration test 79

5.2.4 Unfolding MC 82

5.2.5 Closure test 85

5.2.6 Comparison response matrix 88

5.2.7 Unfolding data 91

5.2.8 Fractional statistical error 94

5.2.9 Bottom line test 97

6. Systematic Uncertainties 103

6.1 Jet Energy Scale 103

6.2 Jet Energy Resolution 107

6.3 Pileup 110

6.4 Physics Model 113

6.5 Unfolding Method 116

6.6 Summary of Systemic Uncertainties 119

7. Results 125

7.1 Theoretical prediction 125

7.2 Comparison of data and predictions 126

7.3 Chi-Square Fitting 130

8. Summary and Conclusions 135

Bibliography 139

Abstract (in Korean) 145

List of Figures

2.1 Schematic representation of soft emissions in QED and QCD. The angular ordered emissions along an external leg in QED (top) and in QCD (bottom) [1]. 10
2.2 Observed η_3 distribution compared to the predictions of (a) HERWIG; (b) ISAJET; (c) PYTHIA; (d) PYTHIA + [2]. 11
2.3 In QCD, for large charge separation, field lines are supposed to be compressed to a tubelike region: string [3]. 12
2.4 The full QCD potential needs to consider nonperturbative string breaking [3]. 12
2.5 (a) String break up in a $q\bar{q}$ event. (b) String drawing in a $q\bar{q}g$ event [4]. 13
2.6 3-jet event structure for (a) string fragmetation (SF), (b) independent fragmentation (IF), and (c) cluster fragmentation (CF) models. In (a) and (b), the arrow indicate the momentum space distribution of particles. The dashed curve in (a) represent strings stretched between the partons, in (b) they represent the parton directions. (c) shows the CF model quark-gluon shower (solid and curly lines) and clusters (dashed ellipses). The motion of the clusters is indicated by arrows; the resulting momentum space distribution of particles is similar to that in (a) for CF models exhibiting a depletion effect [5]. 14

2.7 Particle density distribution $(1/N)dN/d\phi$ in 3-jet events for (a) all charged particles and photons, for (b) those charged particles and photons satisfying $0.3 < p_{out} < 0.5$ GeV/c and for (c) a heavy particle sample of charged and neutral kaons, protons, and lambdas. Also shown are the predictions of SF, IF_1, and CF models with full detector simulation [5]. 15
2.8 $\Delta\eta_{23}$ distributions for PYTHIA 8, MADGRAPH, POWHEG, and PYTHIA 6, (a) central ($|\eta_2| < 0.8$) and (b) the forward ($0.8 < |\eta_2| < 2.5$) regions. 21
2.9 $\Delta\phi_{23}$ distributions for PYTHIA 8, MADGRAPH, POWHEG, and PYTHIA 6, (a) central ($|\eta_2| < 0.8$) and (b) the forward ($0.8 < |\eta_2| < 2.5$) regions. 22
2.10 The β distributions of the unfolded data and their systematic and statistical uncertainties in yellow bands for the (a) central ($|\eta_2| < 0.8$) and (b) the forward ($0.8 < |\eta_2| < 2.5$) regions. MC models are compared at the particle level. 23
2.11 Four different cases in parton radiation. (a) soft p_T radiation with a small angle: small $p_{\mathrm{T}3}/p_{\mathrm{T}2}$, small ΔR_{23}, (b) hard p_T radiation with a small angle: large $p_{\mathrm{T}3}/p_{\mathrm{T}2}$, small ΔR_{23}, (c) large angle radiation with soft p_T: small $p_{\mathrm{T}3}/p_{\mathrm{T}2}$, large ΔR_{23}, (d) large angle radiation with hard p_T: large $p_{\mathrm{T}3}/p_{\mathrm{T}2}$, large ΔR_{23}. 26

3.1 Illustration of the CERN accelerator complex [6]. 32

5.1 $\sqrt{s} = 8$ TeV data and theoretical predictions comparisons. (a) $p_{\mathrm{T}1}$ distribution for the events with a small angle radiation ($\Delta R_{23} < 1.0$), (b) $p_{\mathrm{T}1}$ distribution for the events with a large angle radiation ($\Delta R_{23} > 1.0$), (c) $p_{\mathrm{T}1}$ distribution for soft p_T radiation case ($p_{\mathrm{T}3}/p_{\mathrm{T}2} < 0.3$), (d) $p_{\mathrm{T}1}$ distribution for hard p_T radiation case ($p_{\mathrm{T}3}/p_{\mathrm{T}2} > 0.6$). 49

5.2 $\sqrt{s} = 8$ TeV data and theoretical predictions comparisons. (a) p_{T2} distribution for the events with a small angle radiation ($\Delta R_{23} < 1.0$), (b) p_{T2} distribution for the events with a large angle radiation ($\Delta R_{23} > 1.0$), (c) p_{T2} distribution for soft p_T radiation case ($p_{T3}/p_{T2} < 0.3$), (d) p_{T2} distribution for hard p_T radiation case ($p_{T3}/p_{T2} > 0.6$). 50
5.3 $\sqrt{s} = 8$ TeV data and theoretical predictions comparisons. (a) p_{T3} distribution for the events with a small angle radiation ($\Delta R_{23} < 1.0$), (b) p_{T3} distribution for the events with a large angle radiation ($\Delta R_{23} > 1.0$), (c) p_{T3} distribution for soft p_T radiation case ($p_{T3}/p_{T2} < 0.3$), (d) p_{T3} distribution for hard p_T radiation case ($p_{T3}/p_{T2} > 0.6$). 51
5.4 $\sqrt{s} = 8$ TeV data and theoretical predictions comparisons. (a) y_1 distribution for the events with a small angle radiation ($\Delta R_{23} < 1.0$), (b) y_1 distribution for the events with a large angle radiation ($\Delta R_{23} > 1.0$), (c) y_1 distribution for soft p_T radiation case ($p_{T3}/p_{T2} < 0.3$), (d) y_1 distribution for hard p_T radiation case ($p_{T3}/p_{T2} > 0.6$). 52
5.5 $\sqrt{s} = 8$ TeV data and theoretical predictions comparisons. (a) y_2 distribution for the events with a small angle radiation ($\Delta R_{23} < 1.0$), (b) y_2 distribution for the events with a large angle radiation ($\Delta R_{23} > 1.0$), (c) y_2 distribution for soft p_T radiation case ($p_{T3}/p_{T2} < 0.3$), (d) y_2 distribution for hard p_T radiation case ($p_{T3}/p_{T2} > 0.6$). 53
5.6 $\sqrt{s} = 8$ TeV data and theoretical predictions comparisons. (a) y_3 distribution for the events with a small angle radiation ($\Delta R_{23} < 1.0$), (b) y_3 distribution for the events with a large angle radiation ($\Delta R_{23} > 1.0$), (c) y_3 distribution for soft p_T radiation case ($p_{T3}/p_{T2} < 0.3$), (d) y_3 distribution for hard p_T radiation case ($p_{T3}/p_{T2} > 0.6$). 54

5.7 $\sqrt{s} = 8$ TeV data and theoretical predictions comparisons. (a) Number of jet distribution for the events with a small angle radiation ($\Delta R_{23} < 1.0$), (b) Number of jet distribution for the events with a large angle radiation ($\Delta R_{23} > 1.0$), (c) Number of jet distribution for soft p_{T} radiation case ($p_{\mathrm{T3}}/p_{\mathrm{T2}} < 0.3$), (d) Number of jet distribution for hard p_{T} radiation case ($p_{\mathrm{T3}}/p_{\mathrm{T2}} > 0.6$). . . 55
5.8 $\sqrt{s} = 8$ TeV data and theoretical predictions comparisons. (a) Number of vertex distribution for the events with a small angle radiation ($\Delta R_{23} < 1.0$), (b) Number of vertex distribution for the events with a large angle radiation ($\Delta R_{23} > 1.0$), (c) Number of vertex distribution for soft p_{T} radiation case ($p_{\mathrm{T3}}/p_{\mathrm{T2}} < 0.3$), (d) Number of vertex distribution for hard p_{T} radiation case ($p_{\mathrm{T3}}/p_{\mathrm{T2}} > 0.6$). 56
5.9 $\sqrt{s} = 8$ TeV data and theoretical predictions comparisons. (a) $p_{\mathrm{T3}}/p_{\mathrm{T2}}$ distribution for the events with a small angle radiation ($\Delta R_{23} < 1.0$), (b) $p_{\mathrm{T3}}/p_{\mathrm{T2}}$ distribution for the events with a large angle radiation ($\Delta R_{23} > 1.0$), (c) ΔR_{23} distribution for soft p_{T} radiation case ($p_{\mathrm{T3}}/p_{\mathrm{T2}} < 0.3$), (d) ΔR_{23} distribution for hard p_{T} radiation case ($p_{\mathrm{T3}}/p_{\mathrm{T2}} > 0.6$). 57
5.10 $\sqrt{s} = 13$ TeV data and theoretical predictions comparisons. (a) p_{T1} distribution for the events with a small angle radiation ($\Delta R_{23} < 1.0$), (b) p_{T1} distribution for the events with a large angle radiation ($\Delta R_{23} > 1.0$), (c) p_{T1} distribution for soft p_{T} radiation case ($p_{\mathrm{T3}}/p_{\mathrm{T2}} < 0.3$), (d) p_{T1} distribution for hard p_{T} radiation case ($p_{\mathrm{T3}}/p_{\mathrm{T2}} > 0.6$). 60
5.11 $\sqrt{s} = 13$ TeV data and theoretical predictions comparisons. (a) p_{T2} distribution for the events with a small angle radiation ($\Delta R_{23} < 1.0$), (b) p_{T2} distribution for the events with a large angle radiation ($\Delta R_{23} > 1.0$), (c) p_{T2} distribution for soft p_{T} radiation case ($p_{\mathrm{T3}}/p_{\mathrm{T2}} < 0.3$), (d) p_{T2} distribution for hard p_{T} radiation case ($p_{\mathrm{T3}}/p_{\mathrm{T2}} > 0.6$). 61

5.12 $\sqrt{s} = 13$ TeV data and theoretical predictions comparisons. (a) $p_{\mathrm{T}3}$ distribution for the events with a small angle radiation ($\Delta R_{23} < 1.0$), (b) $p_{\mathrm{T}3}$ distribution for the events with a large angle radiation ($\Delta R_{23} > 1.0$), (c) $p_{\mathrm{T}3}$ distribution for soft p_{T} radiation case ($p_{\mathrm{T}3}/p_{\mathrm{T}2} < 0.3$), (d) $p_{\mathrm{T}3}$ distribution for hard p_{T} radiation case ($p_{\mathrm{T}3}/p_{\mathrm{T}2} > 0.6$). 62
5.13 $\sqrt{s} = 13$ TeV data and theoretical predictions comparisons. (a) y_1 distribution for the events with a small angle radiation ($\Delta R_{23} < 1.0$), (b) y_1 distribution for the events with a large angle radiation ($\Delta R_{23} > 1.0$), (c) y_1 distribution for soft p_{T} radiation case ($p_{\mathrm{T}3}/p_{\mathrm{T}2} < 0.3$), (d) y_1 distribution for hard p_{T} radiation case ($p_{\mathrm{T}3}/p_{\mathrm{T}2} > 0.6$). 63
5.14 $\sqrt{s} = 13$ TeV data and theoretical predictions comparisons. (a) y_2 distribution for the events with a small angle radiation ($\Delta R_{23} < 1.0$), (b) y_2 distribution for the events with a large angle radiation ($\Delta R_{23} > 1.0$), (c) y_2 distribution for soft p_{T} radiation case ($p_{\mathrm{T}3}/p_{\mathrm{T}2} < 0.3$), (d) y_2 distribution for hard p_{T} radiation case ($p_{\mathrm{T}3}/p_{\mathrm{T}2} > 0.6$). 64
5.15 $\sqrt{s} = 13$ TeV data and theoretical predictions comparisons. (a) y_3 distribution for the events with a small angle radiation ($\Delta R_{23} < 1.0$), (b) y_3 distribution for the events with a large angle radiation ($\Delta R_{23} > 1.0$), (c) y_3 distribution for soft p_{T} radiation case ($p_{\mathrm{T}3}/p_{\mathrm{T}2} < 0.3$), (d) y_3 distribution for hard p_{T} radiation case ($p_{\mathrm{T}3}/p_{\mathrm{T}2} > 0.6$). 65
5.16 $\sqrt{s} = 13$ TeV data and theoretical predictions comparisons. (a) Number of jet distribution for the events with a small angle radiation ($\Delta R_{23} < 1.0$), (b) Number of jet distribution for the events with a large angle radiation ($\Delta R_{23} > 1.0$), (c) Number of jet distribution for soft p_{T} radiation case ($p_{\mathrm{T}3}/p_{\mathrm{T}2} < 0.3$), (d) Number of jet distribution for hard p_{T} radiation case ($p_{\mathrm{T}3}/p_{\mathrm{T}2} > 0.6$). . . 66

5.17 $\sqrt{s} = 13$ TeV data and theoretical predictions comparisons. (a) Number of vertex distribution for the events with a small angle radiation ($\Delta R_{23} < 1.0$), (b) Number of vertex distribution for the events with a large angle radiation ($\Delta R_{23} > 1.0$), (c) Number of vertex distribution for soft p_{T} radiation case ($p_{\mathrm{T3}}/p_{\mathrm{T2}} < 0.3$), (d) Number of vertex distribution for hard p_{T} radiation case ($p_{\mathrm{T3}}/p_{\mathrm{T2}} > 0.6$). 67
5.18 $\sqrt{s} = 13$ TeV data and theoretical predictions comparisons. (a) $p_{\mathrm{T3}}/p_{\mathrm{T2}}$ distribution for the events with a small angle radiation ($\Delta R_{23} < 1.0$), (b) $p_{\mathrm{T3}}/p_{\mathrm{T2}}$ distribution for the events with a large angle radiation ($\Delta R_{23} > 1.0$), (c) ΔR_{23} distribution for soft p_{T} radiation case ($p_{\mathrm{T3}}/p_{\mathrm{T2}} < 0.3$), (d) ΔR_{23} distribution for hard p_{T} radiation case ($p_{\mathrm{T3}}/p_{\mathrm{T2}} > 0.6$). 68
5.19 $\sqrt{s} = 8$ TeV response matrices. (a) $p_{\mathrm{T3}}/p_{\mathrm{T2}}$ distribution response matrix for the events with a small angle radiation ($\Delta R_{23} < 1.0$), (b) $p_{\mathrm{T3}}/p_{\mathrm{T2}}$ distribution response matrix for the events with a large angle radiation ($\Delta R_{23} > 1.0$), (c) ΔR_{23} distribution response matrix for soft p_{T} radiation case ($p_{\mathrm{T3}}/p_{\mathrm{T2}} < 0.3$), (d) ΔR_{23} distribution response matrix for hard p_{T} radiation case ($p_{\mathrm{T3}}/p_{\mathrm{T2}} > 0.6$). 71
5.20 $\sqrt{s} = 13$ TeV response matrices. (a) $p_{\mathrm{T3}}/p_{\mathrm{T2}}$ distribution response matrix for the events with a small angle radiation ($\Delta R_{23} < 1.0$), (b) $p_{\mathrm{T3}}/p_{\mathrm{T2}}$ distribution response matrix for the events with a large angle radiation ($\Delta R_{23} > 1.0$), (c) ΔR_{23} distribution response matrix for soft p_{T} radiation case ($p_{\mathrm{T3}}/p_{\mathrm{T2}} < 0.3$), (d) ΔR_{23} distribution response matrix for hard p_{T} radiation case ($p_{\mathrm{T3}}/p_{\mathrm{T2}} > 0.6$). 72
5.21 $\sqrt{s} = 8$ TeV the purity. (a) $p_{\mathrm{T3}}/p_{\mathrm{T2}}$ distribution purity for the events with a small angle radiation ($\Delta R_{23} < 1.0$), (b) $p_{\mathrm{T3}}/p_{\mathrm{T2}}$ distribution purity for the events with a large angle radiation ($\Delta R_{23} > 1.0$), (c) ΔR_{23} distribution purity for soft p_{T} radiation case ($p_{\mathrm{T3}}/p_{\mathrm{T2}} < 0.3$), (d) ΔR_{23} distribution purity for hard p_{T} radiation case ($p_{\mathrm{T3}}/p_{\mathrm{T2}} > 0.6$). 75

5.22 $\sqrt{s} = 13$ TeV the purity. (a) p_{T3}/p_{T2} distribution purity for the events with a small angle radiation ($\Delta R_{23} < 1.0$), (b) p_{T3}/p_{T2} distribution purity for the events with a large angle radiation ($\Delta R_{23} > 1.0$), (c) ΔR_{23} distribution purity for soft p_T radiation case ($p_{T3}/p_{T2} < 0.3$), (d) ΔR_{23} distribution purity for hard p_T radiation case ($p_{T3}/p_{T2} > 0.6$). 75
5.23 $\sqrt{s} = 8$ TeV the stability. (a) p_{T3}/p_{T2} distribution stability for the events with a small angle radiation ($\Delta R_{23} < 1.0$), (b) p_{T3}/p_{T2} distribution stability for the events with a large angle radiation ($\Delta R_{23} > 1.0$), (c) ΔR_{23} distribution stability for soft p_T radiation case ($p_{T3}/p_{T2} < 0.3$), (d) ΔR_{23} distribution stability for hard p_T radiation case ($p_{T3}/p_{T2} > 0.6$). 76
5.24 $\sqrt{s} = 13$ TeV the stability. (a) p_{T3}/p_{T2} distribution stability for the events with a small angle radiation ($\Delta R_{23} < 1.0$), (b) p_{T3}/p_{T2} distribution stability for the events with a large angle radiation ($\Delta R_{23} > 1.0$), (c) ΔR_{23} distribution stability for soft p_T radiation case ($p_{T3}/p_{T2} < 0.3$), (d) ΔR_{23} distribution stability for hard p_T radiation case ($p_{T3}/p_{T2} > 0.6$). 76
5.25 $\sqrt{s} = 8$ TeV the acceptance. (a) p_{T3}/p_{T2} distribution acceptance for the events with a small angle radiation ($\Delta R_{23} < 1.0$), (b) p_{T3}/p_{T2} distribution acceptance for the events with a large angle radiation ($\Delta R_{23} > 1.0$), (c) ΔR_{23} distribution acceptance for soft p_T radiation case ($p_{T3}/p_{T2} < 0.3$), (d) ΔR_{23} distribution acceptance for hard p_T radiation case ($p_{T3}/p_{T2} > 0.6$). 77
5.26 $\sqrt{s} = 13$ TeV the acceptance. (a) p_{T3}/p_{T2} distribution acceptance for the events with a small angle radiation ($\Delta R_{23} < 1.0$), (b) p_{T3}/p_{T2} distribution acceptance for the events with a large angle radiation ($\Delta R_{23} > 1.0$), (c) ΔR_{23} distribution acceptance for soft p_T radiation case ($p_{T3}/p_{T2} < 0.3$), (d) ΔR_{23} distribution acceptance for hard p_T radiation case ($p_{T3}/p_{T2} > 0.6$). 77

5.27 $\sqrt{s} = 8$ TeV the background. (a) p_{T3}/p_{T2} distribution background for the events with a small angle radiation ($\Delta R_{23} < 1.0$), (b) p_{T3}/p_{T2} distribution background for the events with a large angle radiation ($\Delta R_{23} > 1.0$), (c) ΔR_{23} distribution background for soft p_T radiation case ($p_{T3}/p_{T2} < 0.3$), (d) ΔR_{23} distribution background for hard p_T radiation case ($p_{T3}/p_{T2} > 0.6$). 78
5.28 $\sqrt{s} = 13$ TeV the background. (a) p_{T3}/p_{T2} distribution background for the events with a small angle radiation ($\Delta R_{23} < 1.0$), (b) p_{T3}/p_{T2} distribution background for the events with a large angle radiation ($\Delta R_{23} > 1.0$), (c) ΔR_{23} distribution background for soft p_T radiation case ($p_{T3}/p_{T2} < 0.3$), (d) ΔR_{23} distribution background for hard p_T radiation case ($p_{T3}/p_{T2} > 0.6$). 78
5.29 $\sqrt{s} = 8$ TeV the iteration test results. (a) p_{T3}/p_{T2} distribution for the events with a small angle radiation ($\Delta R_{23} < 1.0$), (b) p_{T3}/p_{T2} distribution for the events with a large angle radiation ($\Delta R_{23} > 1.0$), (c) ΔR_{23} distribution for soft p_T radiation case ($p_{T3}/p_{T2} < 0.3$), (d) ΔR_{23} distribution for hard p_T radiation case ($p_{T3}/p_{T2} > 0.6$). 80
5.30 $\sqrt{s} = 13$ TeV the iteration test results. (a) p_{T3}/p_{T2} distribution for the events with a small angle radiation ($\Delta R_{23} < 1.0$), (b) p_{T3}/p_{T2} distribution for the events with a large angle radiation ($\Delta R_{23} > 1.0$), (c) ΔR_{23} distribution for soft p_T radiation case ($p_{T3}/p_{T2} < 0.3$), (d) ΔR_{23} distribution for hard p_T radiation case ($p_{T3}/p_{T2} > 0.6$). 81
5.31 $\sqrt{s} = 8$ TeV the unfolded MC results. (a) p_{T3}/p_{T2} distribution for the events with a small angle radiation ($\Delta R_{23} < 1.0$), (b) p_{T3}/p_{T2} distribution for the events with a large angle radiation ($\Delta R_{23} > 1.0$), (c) ΔR_{23} distribution for soft p_T radiation case ($p_{T3}/p_{T2} < 0.3$), (d) ΔR_{23} distribution for hard p_T radiation case ($p_{T3}/p_{T2} > 0.6$). 83

5.32 $\sqrt{s} = 13$ TeV the unfolded MC results. (a) p_{T3}/p_{T2} distribution for the events with a small angle radiation ($\Delta R_{23} < 1.0$), (b) p_{T3}/p_{T2} distribution for the events with a large angle radiation ($\Delta R_{23} > 1.0$), (c) ΔR_{23} distribution for soft p_T radiation case ($p_{T3}/p_{T2} < 0.3$), (d) ΔR_{23} distribution for hard p_T radiation case ($p_{T3}/p_{T2} > 0.6$). 84
5.33 $\sqrt{s} = 8$ TeV the closure test results. (a) p_{T3}/p_{T2} distribution for the events with a small angle radiation ($\Delta R_{23} < 1.0$), (b) p_{T3}/p_{T2} distribution for the events with a large angle radiation ($\Delta R_{23} > 1.0$), (c) ΔR_{23} distribution for soft p_T radiation case ($p_{T3}/p_{T2} < 0.3$), (d) ΔR_{23} distribution for hard p_T radiation case ($p_{T3}/p_{T2} > 0.6$). 86
5.34 $\sqrt{s} = 13$ TeV the closure test results. (a) p_{T3}/p_{T2} distribution for the events with a small angle radiation ($\Delta R_{23} < 1.0$), (b) p_{T3}/p_{T2} distribution for the events with a large angle radiation ($\Delta R_{23} > 1.0$), (c) ΔR_{23} distribution for soft p_T radiation case ($p_{T3}/p_{T2} < 0.3$), (d) ΔR_{23} distribution for hard p_T radiation case ($p_{T3}/p_{T2} > 0.6$). 87
5.35 $\sqrt{s} = 8$ TeV the results of comparison response matrices. (a) p_{T3}/p_{T2} distribution for the events with a small angle radiation ($\Delta R_{23} < 1.0$), (b) p_{T3}/p_{T2} distribution for the events with a large angle radiation ($\Delta R_{23} > 1.0$), (c) ΔR_{23} distribution for soft p_T radiation case ($p_{T3}/p_{T2} < 0.3$), (d) ΔR_{23} distribution for hard p_T radiation case ($p_{T3}/p_{T2} > 0.6$). 89
5.36 $\sqrt{s} = 13$ TeV the results of comparison response matrices. (a) p_{T3}/p_{T2} distribution for the events with a small angle radiation ($\Delta R_{23} < 1.0$), (b) p_{T3}/p_{T2} distribution for the events with a large angle radiation ($\Delta R_{23} > 1.0$), (c) ΔR_{23} distribution for soft p_T radiation case ($p_{T3}/p_{T2} < 0.3$), (d) ΔR_{23} distribution for hard p_T radiation case ($p_{T3}/p_{T2} > 0.6$). 90

5.37 $\sqrt{s} = 8$ TeV the unfolded data. (a) p_{T3}/p_{T2} distribution for the events with a small angle radiation ($\Delta R_{23} < 1.0$), (b) p_{T3}/p_{T2} distribution for the events with a large angle radiation ($\Delta R_{23} > 1.0$), (c) ΔR_{23} distribution for soft p_T radiation case ($p_{T3}/p_{T2} < 0.3$), (d) ΔR_{23} distribution for hard p_T radiation case ($p_{T3}/p_{T2} > 0.6$). 92
5.38 $\sqrt{s} = 13$ TeV the unfolded data. (a) p_{T3}/p_{T2} distribution for the events with a small angle radiation ($\Delta R_{23} < 1.0$), (b) p_{T3}/p_{T2} distribution for the events with a large angle radiation ($\Delta R_{23} > 1.0$), (c) ΔR_{23} distribution for soft p_T radiation case ($p_{T3}/p_{T2} < 0.3$), (d) ΔR_{23} distribution for hard p_T radiation case ($p_{T3}/p_{T2} > 0.6$). 93
5.39 $\sqrt{s} = 8$ TeV the fractional statistical error. (a) p_{T3}/p_{T2} distribution for the events with a small angle radiation ($\Delta R_{23} < 1.0$), (b) p_{T3}/p_{T2} distribution for the events with a large angle radiation ($\Delta R_{23} > 1.0$), (c) ΔR_{23} distribution for soft p_T radiation case ($p_{T3}/p_{T2} < 0.3$), (d) ΔR_{23} distribution for hard p_T radiation case ($p_{T3}/p_{T2} > 0.6$). 95
5.40 $\sqrt{s} = 13$ TeV the fractional statistical error. (a) p_{T3}/p_{T2} distribution for the events with a small angle radiation ($\Delta R_{23} < 1.0$), (b) p_{T3}/p_{T2} distribution for the events with a large angle radiation ($\Delta R_{23} > 1.0$), (c) ΔR_{23} distribution for soft p_T radiation case ($p_{T3}/p_{T2} < 0.3$), (d) ΔR_{23} distribution for hard p_T radiation case ($p_{T3}/p_{T2} > 0.6$). 96

6.1 $\sqrt{s} = 8$ TeV JES systematic uncertainty. (a) p_{T3}/p_{T2} distribution for the events with a small angle radiation ($\Delta R_{23} < 1.0$), (b) p_{T3}/p_{T2} distribution for the events with a large angle radiation ($\Delta R_{23} > 1.0$), (c) ΔR_{23} distribution for soft p_T radiation case ($p_{T3}/p_{T2} < 0.3$), (d) ΔR_{23} distribution for hard p_T radiation case ($p_{T3}/p_{T2} > 0.6$). 105

6.2 $\sqrt{s} = 13$ TeV JES systematic uncertainty. (a) p_{T3}/p_{T2} distribution for the events with a small angle radiation ($\Delta R_{23} < 1.0$), (b) p_{T3}/p_{T2} distribution for the events with a large angle radiation ($\Delta R_{23} > 1.0$), (c) ΔR_{23} distribution for soft p_T radiation case ($p_{T3}/p_{T2} < 0.3$), (d) ΔR_{23} distribution for hard p_T radiation case ($p_{T3}/p_{T2} > 0.6$). 106
6.3 $\sqrt{s} = 8$ TeV JER systematic uncertainty. (a) p_{T3}/p_{T2} distribution for the events with a small angle radiation ($\Delta R_{23} < 1.0$), (b) p_{T3}/p_{T2} distribution for the events with a large angle radiation ($\Delta R_{23} > 1.0$), (c) ΔR_{23} distribution for soft p_T radiation case ($p_{T3}/p_{T2} < 0.3$), (d) ΔR_{23} distribution for hard p_T radiation case ($p_{T3}/p_{T2} > 0.6$). 108
6.4 $\sqrt{s} = 13$ TeV JER systematic uncertainty. (a) p_{T3}/p_{T2} distribution for the events with a small angle radiation ($\Delta R_{23} < 1.0$), (b) p_{T3}/p_{T2} distribution for the events with a large angle radiation ($\Delta R_{23} > 1.0$), (c) ΔR_{23} distribution for soft p_T radiation case ($p_{T3}/p_{T2} < 0.3$), (d) ΔR_{23} distribution for hard p_T radiation case ($p_{T3}/p_{T2} > 0.6$). 109
6.5 $\sqrt{s} = 8$ TeV PU systematic uncertainty. (a) p_{T3}/p_{T2} distribution for the events with a small angle radiation ($\Delta R_{23} < 1.0$), (b) p_{T3}/p_{T2} distribution for the events with a large angle radiation ($\Delta R_{23} > 1.0$), (c) ΔR_{23} distribution for soft p_T radiation case ($p_{T3}/p_{T2} < 0.3$), (d) ΔR_{23} distribution for hard p_T radiation case ($p_{T3}/p_{T2} > 0.6$). 111
6.6 $\sqrt{s} = 13$ TeV PU systematic uncertainty. (a) p_{T3}/p_{T2} distribution for the events with a small angle radiation ($\Delta R_{23} < 1.0$), (b) p_{T3}/p_{T2} distribution for the events with a large angle radiation ($\Delta R_{23} > 1.0$), (c) ΔR_{23} distribution for soft p_T radiation case ($p_{T3}/p_{T2} < 0.3$), (d) ΔR_{23} distribution for hard p_T radiation case ($p_{T3}/p_{T2} > 0.6$). 112

6.7 $\sqrt{s} = 8$ TeV MOD systematic uncertainty. (a) $p_{\mathrm{T3}}/p_{\mathrm{T2}}$ distribution for the events with a small angle radiation ($\Delta R_{23} < 1.0$), (b) $p_{\mathrm{T3}}/p_{\mathrm{T2}}$ distribution for the events with a large angle radiation ($\Delta R_{23} > 1.0$), (c) ΔR_{23} distribution for soft p_{T} radiation case ($p_{\mathrm{T3}}/p_{\mathrm{T2}} < 0.3$), (d) ΔR_{23} distribution for hard p_{T} radiation case ($p_{\mathrm{T3}}/p_{\mathrm{T2}} > 0.6$). 114
6.8 $\sqrt{s} = 13$ TeV MOD systematic uncertainty. (a) $p_{\mathrm{T3}}/p_{\mathrm{T2}}$ distribution for the events with a small angle radiation ($\Delta R_{23} < 1.0$), (b) $p_{\mathrm{T3}}/p_{\mathrm{T2}}$ distribution for the events with a large angle radiation ($\Delta R_{23} > 1.0$), (c) ΔR_{23} distribution for soft p_{T} radiation case ($p_{\mathrm{T3}}/p_{\mathrm{T2}} < 0.3$), (d) ΔR_{23} distribution for hard p_{T} radiation case ($p_{\mathrm{T3}}/p_{\mathrm{T2}} > 0.6$). 115
6.9 $\sqrt{s} = 8$ TeV UNFOLD systematic uncertainty. (a) $p_{\mathrm{T3}}/p_{\mathrm{T2}}$ distribution for the events with a small angle radiation ($\Delta R_{23} < 1.0$), (b) $p_{\mathrm{T3}}/p_{\mathrm{T2}}$ distribution for the events with a large angle radiation ($\Delta R_{23} > 1.0$), (c) ΔR_{23} distribution for soft p_{T} radiation case ($p_{\mathrm{T3}}/p_{\mathrm{T2}} < 0.3$), (d) ΔR_{23} distribution for hard p_{T} radiation case ($p_{\mathrm{T3}}/p_{\mathrm{T2}} > 0.6$). 117
6.10 $\sqrt{s} = 13$ TeV UNFOLD systematic uncertainty. (a) $p_{\mathrm{T3}}/p_{\mathrm{T2}}$ distribution for the events with a small angle radiation ($\Delta R_{23} < 1.0$), (b) $p_{\mathrm{T3}}/p_{\mathrm{T2}}$ distribution for the events with a large angle radiation ($\Delta R_{23} > 1.0$), (c) ΔR_{23} distribution for soft p_{T} radiation case ($p_{\mathrm{T3}}/p_{\mathrm{T2}} < 0.3$), (d) ΔR_{23} distribution for hard p_{T} radiation case ($p_{\mathrm{T3}}/p_{\mathrm{T2}} > 0.6$). 118
6.11 $\sqrt{s} = 8$ TeV the summary of systematic uncertainties. (a) $p_{\mathrm{T3}}/p_{\mathrm{T2}}$ distribution for the events with a small angle radiation ($\Delta R_{23} < 1.0$), (b) $p_{\mathrm{T3}}/p_{\mathrm{T2}}$ distribution for the events with a large angle radiation ($\Delta R_{23} > 1.0$), (c) ΔR_{23} distribution for soft p_{T} radiation case ($p_{\mathrm{T3}}/p_{\mathrm{T2}} < 0.3$), (d) ΔR_{23} distribution for hard p_{T} radiation case ($p_{\mathrm{T3}}/p_{\mathrm{T2}} > 0.6$). 122

6.12 $\sqrt{s} = 13$ TeV the summary of systematic uncertainties. (a) p_{T3}/p_{T2} distribution for the events with a small angle radiation ($\Delta R_{23} < 1.0$), (b) p_{T3}/p_{T2} distribution for the events with a large angle radiation ($\Delta R_{23} > 1.0$), (c) ΔR_{23} distribution for soft p_T radiation case ($p_{T3}/p_{T2} < 0.3$), (d) ΔR_{23} distribution for hard p_T radiation case ($p_{T3}/p_{T2} > 0.6$). 124

7.1 $\sqrt{s} = 8$ TeV data and theoretical predictions comparisons. (a) p_{T3}/p_{T2} distribution for the events with a small angle radiation ($\Delta R_{23} < 1.0$), (b) p_{T3}/p_{T2} distribution for the events with a large angle radiation ($\Delta R_{23} > 1.0$), (c) ΔR_{23} distribution for soft p_T radiation case ($p_{T3}/p_{T2} < 0.3$), (d) ΔR_{23} distribution for hard p_T radiation case ($p_{T3}/p_{T2} > 0.6$). 128

7.2 $\sqrt{s} = 13$ TeV data and theoretical predictions comparisons. (a) p_{T3}/p_{T2} distribution for the events with a small angle radiation ($\Delta R_{23} < 1.0$), (b) p_{T3}/p_{T2} distribution for the events with a large angle radiation ($\Delta R_{23} > 1.0$), (c) ΔR_{23} distribution for soft p_T radiation case ($p_{T3}/p_{T2} < 0.3$), (d) ΔR_{23} distribution for hard p_T radiation case ($p_{T3}/p_{T2} > 0.6$). 129

7.3 $\sqrt{s} = 8$ TeV the fractional statistical error of MC. (a) p_{T3}/p_{T2} distribution for the events with a small angle radiation ($\Delta R_{23} < 1.0$), (b) p_{T3}/p_{T2} distribution for the events with a large angle radiation ($\Delta R_{23} > 1.0$), (c) ΔR_{23} distribution for soft p_T radiation case ($p_{T3}/p_{T2} < 0.3$), (d) ΔR_{23} distribution for hard p_T radiation case ($p_{T3}/p_{T2} > 0.6$). 132

7.4 $\sqrt{s} = 13$ TeV the fractional statistical error of MC. (a) p_{T3}/p_{T2} distribution for the events with a small angle radiation ($\Delta R_{23} < 1.0$), (b) p_{T3}/p_{T2} distribution for the events with a large angle radiation ($\Delta R_{23} > 1.0$), (c) ΔR_{23} distribution for soft p_T radiation case ($p_{T3}/p_{T2} < 0.3$), (d) ΔR_{23} distribution for hard p_T radiation case ($p_{T3}/p_{T2} > 0.6$). 133

List of Tables

1.1 Quark and lepton: respective masses and electric charge (Q) [7]. . 4

1.2 Mediator bosons carrying the four type of interactions with their boson mass and the relative magnitude [7]. 7

2.1 Summary of the event selection 19

2.2 χ^2 deviations from data for the different MC models. 20

2.3 The PS and ME dominant region. 27

3.1 Energy of the Accelerators 33

4.1 List of $\sqrt{s} = 8\,\text{TeV}$ CMS Data sets and luminosity block 40

4.2 List of $\sqrt{s} = 8\,\text{TeV}$ Data sets 40

4.3 List of $\sqrt{s} = 8\,\text{TeV}$ CMS MC sets 40

4.4 List of PYTHIA 8 sets ($\sqrt{s} = 8\,\text{TeV}$) 40

4.5 List of MADGRAPH sets ($\sqrt{s} = 8\,\text{TeV}$) 41

4.6 List of $\sqrt{s} = 13\,\text{TeV}$ CMS Data sets and luminosity block 41

4.7 List of $\sqrt{s} = 13\,\text{TeV}$ Data sets 45

4.8 List of $\sqrt{s} = 13\,\text{TeV}$ CMS MC sets 45

4.9 List of PYTHIA 8 sets ($\sqrt{s} = 13\,\text{TeV}$) 45

4.10 List of MADGRAPH sets ($\sqrt{s} = 13\,\text{TeV}$) 45

4.11 Trigger 46

4.12 Selection criteria 46

4.13 Number of selected events 46

5.1 $\sqrt{s} = 8\,\text{TeV}$ detector level systematic uncertainties 58

5.2 $\sqrt{s} = 13\,\text{TeV}$ detector level systematic uncertainties 69
5.3 $\sqrt{s} = 8\,\text{TeV}$ Bottom line test 98
5.4 $\sqrt{s} = 13\,\text{TeV}$ Bottom line test 98
5.5 $\sqrt{s} = 8\,\text{TeV}$ the statistical covariance matrix, Cov^{Stat}, taking into account the correlations due to unfolding in $p_{\text{T3}}/p_{\text{T2}}$, $\Delta R_{23} < 1.0$ (PS dominant region) 99
5.6 $\sqrt{s} = 8\,\text{TeV}$ the statistical covariance matrix, Cov^{Stat}, taking into account the correlations due to unfolding in $p_{\text{T3}}/p_{\text{T2}}$, $< \Delta R_{23} >$ 1.0 (ME dominant region) 99
5.7 $\sqrt{s} = 8\,\text{TeV}$ the statistical covariance matrix, Cov^{Stat}, taking into account the correlations due to unfolding in ΔR_{23}, $p_{\text{T3}}/p_{\text{T2}} < 0.3$ (PS dominant region) 100
5.8 $\sqrt{s} = 8\,\text{TeV}$ the statistical covariance matrix, Cov^{Stat}, taking into account the correlations due to unfolding in ΔR_{23}, $p_{\text{T3}}/p_{\text{T2}} > 0.6$ (ME dominant region) 100
5.9 $\sqrt{s} = 13\,\text{TeV}$ the statistical covariance matrix, Cov^{Stat}, taking into account the correlations due to unfolding in $p_{\text{T3}}/p_{\text{T2}}$, $\Delta R_{23} < 1.0$ (PS dominant region) 101
5.10 $\sqrt{s} = 13\,\text{TeV}$ the statistical covariance matrix, Cov^{Stat}, taking into account the correlations due to unfolding in $p_{\text{T3}}/p_{\text{T2}}$, $\Delta R_{23} > 1.0$ (ME dominant region) 101
5.11 $\sqrt{s} = 13\,\text{TeV}$ the statistical covariance matrix, Cov^{Stat}, taking into account the correlations due to unfolding in ΔR_{23}, $p_{\text{T3}}/p_{\text{T2}} < 0.3$ (PS dominant region) 102
5.12 $\sqrt{s} = 13\,\text{TeV}$ the statistical covariance matrix, Cov^{Stat}, taking into account the correlations due to unfolding in ΔR_{23}, $p_{\text{T3}}/p_{\text{T2}} > 0.6$ (ME dominant region) 102

6.1 The scale factors for $\sqrt{s} = 8\,\text{TeV}$ (13 TeV) JER 107
6.2 $\sqrt{s} = 8\,\text{TeV}$ Summary of systematic uncertainties 121
6.3 $\sqrt{s} = 13\,\text{TeV}$ Summary of systematic uncertainties 123

7.1 event classification according to the radiation type 126
7.2 Summary of χ^2/NDF for $\sqrt{s} = 8\,\text{TeV}$ 131

7.3 Summary of χ^2/NDF for $\sqrt{s} = 13\,\text{TeV}$ 131

1 Introduction and Literature Review

The Standard Model (SM) successfully explains and predicts most of the phenomena related to particle physics [8]. The SM is the result of centuries of ideas and research which started from basic questions that were asked from ancient Greece. The Greek philosopher Democritus and his teacher Leucippus considered the basic elements of nature in the 9th century B.C. They conjectured the existence of tiny objects that he called “atoms” for the Greek word “indivisible.” In 1897, J. J. Thomson discovered negatively charged particles which are now called *electrons* [9]. From this discovery, Thomson built the famous model of the atomic structure: the “plum pudding” model in 1898. However, this model was rejected by E. Rutherford’s famous scattering experiment, which was performed by Geiger and Marsden in 1909 and interpreted by Rutherford [10]. With the coming of quantum mechanics in the 1920s, the Heisenberg principle and the wave-particle duality of matter changed the classical concepts of position and velocity. With these basic principles, several breakthroughs happened very quickly and the 20th century was an incredibly successful time in terms of particle discoveries: from the neutron, discovered by Chadwick in 1932, to the quarks (the last one of which was discovered in 1995), leptons, and gauge bosons, which have been interpreted as mediators of the interactions between the elementary particles. All these pieces constitute the building blocks of the SM which were formulated in 1970–1973. The SM is described by a SU(3)×SU(2)×U(1) gauge symmetry [11]. The Lagrangian density of the QCD can be obtained by requiring symmetry under local SU(3) gauge transformations. Each quark appears in three different color states, therefore belonging to a SU(3) triplet. The SU(3) has eight generators, which are associated to the eight gluons. The Lagrangian density of the EWK is obtained using the local SU(2)×U(1) gauge transformations. It has four generators: The long-range electromagnetic interaction is interfered by the massless photon, while the short-range weak force carriers are the massive $\mathbf{W}^{+}$, $\mathbf{W}^{-}$, and $\mathbf{Z}^{0}$ bosons. Between the three observed vector bosons of the EWK interaction, only the photon is massless, while **W** and **Z** bosons are massive, meaning that the gauge symmetry is broken. To give them mass, a spontaneous symmetry breaking mechanism is introduced. It predicts the existence of another fundamental boson which must have spin 0. This boson is usually referred to as the Higgs boson, named after Peter Higgs, who was one of the first to predict its existence [12, 13, 14]. However, this theory is incomplete, as there are several missing pieces. For instance, gravity needs to be introduced to achieve a coherent picture of particles and interactions. Some experimental observations, like neutrino oscillations, or the existence of dark matter and dark energy, along with the matter-antimatter asymmetry, are unresolved in the SM framework [15].

A fermion is a particle that has a half-integer spin satisfying the Fermi-Dirac statistics. In contrast, a boson is a particle that has an integer spin and follows Bose-Einstein statistics. The particles of the SM are described by wave functions which change in space-time and have the nature of quantum fields. A physical quantity which propagates and extends to every point in space-time and a system characterized by quantized numbers define a quantum field. The wave functions for fermions and bosons have different features and consider different symmetries. The fermionic wave function is antisymmetric under the exchange of two particles, while the bosonic wave function is symmetric if two bosons of the system are swapped. The Dirac equation describes the space-time evolution of the fermions. This equation follows the laws of special relativity and admits two solutions of positive and negative energy. The positive energy solutions are the matter particles, while the negative energy solutions are antiparticles. Thus, all fermions have to consider

Table 1.1: Quark and lepton: respective masses and electric charge (Q) [7].

	1st generation	2nd generation	3rd generation	Q
Quark	u $\simeq$ 2.2 MeV	c $\simeq$ 1.28 GeV	t $\simeq$ 173.1 GeV	2/3
	d $\simeq$ 4.7 MeV	s $\simeq$ 96 MeV	b $\simeq$ 4.18 MeV	-1/3
Lepton	e $\simeq$ 0.511 MeV	$\mu \simeq$ 105.7 MeV	$\tau \simeq$ 1.777 GeV	-1
	$\nu_{\mathrm{e}} <$ 2 eV	$\nu_{\mu} <$ 0.19 MeV	$\nu_{\tau} <$ 18.2 MeV	0

their identical antiparticles. The space-time evolution of a boson follows the Klein-Gordon equation [16].

The SM acknowledges two different types of fermions: quarks and leptons. They identify into three groups which are called "generations." For the quarks, the up-type generations have positive charge ($+\frac{2}{3}$), while the down-types are negatively charged ($-\frac{1}{3}$). The first generations are the up-quark (u) and the down-quark (d) which are the lightest, first observed in 1969. The second generations are the strange-quark (s) and the charm-quark (c), while the bottom-quark (b) and the top-quark (t) are included in the third generation. The observations of strange particles in cosmic rays lead to the observation of the strange quark, while the bottom and the charm quark appeared in electron-positron collisions. The top quark was discovered in 1995 in proton-antiproton ($p\bar{p}$) collisions. The "hadrons" are a composition of three or two quarks. "Baryons" are composed of three quarks while the "meson" are composed of two quarks. The three generations of leptons have a negative charge or a neutral charge. The SM framework describes the interactions as an exchange of gauge bosons between interacting particles. Every interaction is identified by a dimensionless coupling, which is equivalent to the strength of the force used by the interaction, and by an interaction range which represents the maximum distance that the virtual state of the exchanged boson is able to travel within the bounds set by the uncertainty principle.

The Quantum Electrodynamics (QED) describes the electromagnetic interaction based on a symmetry group $U(1)_{EM}$. The mediator of the electromagnetic interaction is the photon (γ) which coupled to only electronic charged particles. The coupling strength of the electromagnetic interaction is $\alpha_{EM} = \frac{e^2}{4\pi\epsilon_0\hbar c} \simeq \frac{1}{137}$. The QED can be treated within a perturbative framework because α_{EM} is smaller than 1.

The weak interaction is based on SU(2) symmetry, and the mediator forms a set of three gauge bosons: $\mathbf{W}^{\pm}$ and $\mathbf{Z}^0$. Since the mediators have different electric charges, different types of processes are identified: those mediated by a W boson, where the particles interact via a charged current, and those mediated by a Z boson, which is a neutral current. The two different weak currents present some differences: while the neutral current couples only to quarks of the same flavor, quarks of different generations can interact via charged current. This means that, when a quark is produced as a mass eigenstate in a certain generation, it may decay via weak interaction into a quark of another family, because its weak eigenstate is a superposition of quarks of all three generations. The Cabibbo-Kobayashi-Maskawa (CKM) matrix V_{CKM} in (1.1) is a 3 × 3 unitary complex matrix with most diagonalized coefficients [17, 18].

$$\begin{pmatrix} d' \\ s' \\ t' \end{pmatrix} = V_{\text{CKM}} \begin{pmatrix} d \\ s \\ t \end{pmatrix} = \begin{pmatrix} V_{\text{ud}} & V_{\text{us}} & V_{\text{ub}} \\ V_{\text{cd}} & V_{\text{cs}} & V_{\text{cb}} \\ V_{\text{td}} & V_{\text{ts}} & V_{\text{tb}} \end{pmatrix} \begin{pmatrix} d \\ s \\ t \end{pmatrix} \tag{1.1}$$

This CKM matrix translates to a higher probability for a charged current to change the quark flavor within the same generation and a non-zero probability to access the other generations. Another important feature of the weak interaction charge-parity (CP) violation implies that right-handed and left-handed particles behave differently under weak interaction, as well as particles and antiparticles.

The Quantum Chromodynamics (QCD) describes and explains the strong interaction in SU(3) symmetry. The mediators of the strong interaction are the massless gluons particles with spin 1. In strong interactions, color charged particles couple with the gluons. Even though the gluon is massless, the range of the strong interaction is short because gluon can interact with itself. The strong coupling depends on the scale of the interaction and the QCD behavior at high energy likes "asymptotic freedom" but at low energy is "confinement." The strong coupling is very low at high energy, and

Table 1.2: Mediator bosons carrying the four type of interactions with their boson mass and the relative magnitude [7].

Interaction	Gauge Boson	Mass	Charge
electromagnetic	γ	0	electrical
weak	$\mathbf{W}^{\pm}$ $\mathbf{Z}^{0}$	80.385 GeV 91.1876 GeV	weak isospin
strong	glouns	0	color (r, g, b)

dramatically grows up when going to low energy. At the high energy, perturbative calculations can be analytically performed since the α_S is smaller than 1. For the low energy (scales ∼3 GeV), α_S becomes greater than 1, and nonperturbative studies are need to understand phenomenology.

2 QCD Coherence

The successful explanation of the jets[1] in the QCD framework has been improved. The several models well describe the three-jet event productions from e^+e^- annihilation. These models are preformed in the Monte Carlo model calculation as fragmentation and hadronization. This chapter shows the historical development of QCD coherence calculation and their success.

2.1 Angular Ordering

A simple model of the jet cascade, namely, the radiation pattern of soft photons produced by relativistic e^+e^- pair in a QED shower explains the physical origin of angular ordering. The angle between the bremsstrahlung photon radiation from the e^+e^- production and the electron or the position is smaller than the angle between the electron and the position pair produc-

[1]The jet is a collimated bunch of hadrons from the initial parton after fragmentation and hadronization.

tion (Chudakov effect) [19].

A similar physical picture can be drawn for QCD cascades of soft gluon radiation [20]. There are several different ways to resolve the solution of QCD coherence. One method is angular ordering while the other mothds are mass and p_{T} ordering.

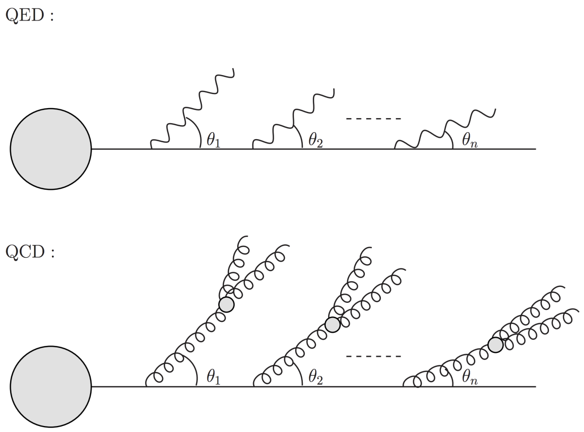

Figure 2.1: Schematic representation of soft emissions in QED and QCD. The angular ordered emissions along an external leg in QED (top) and in QCD (bottom) [1].

A good example of angular ordering calculation implementing is the CDF color coherence research [2]. The third jet pseudorapidity (η_3) distribution is well explained with angular ordering calculation. The distribution of HERWIG and PYTHIA + were in good agreement with data than other without angular ordering calculations (Figure 2.2).

This comparison shows that the angular ordering calculation changes the pseudorapidity (η_3) distribution of the third jet from soft gluon radia-

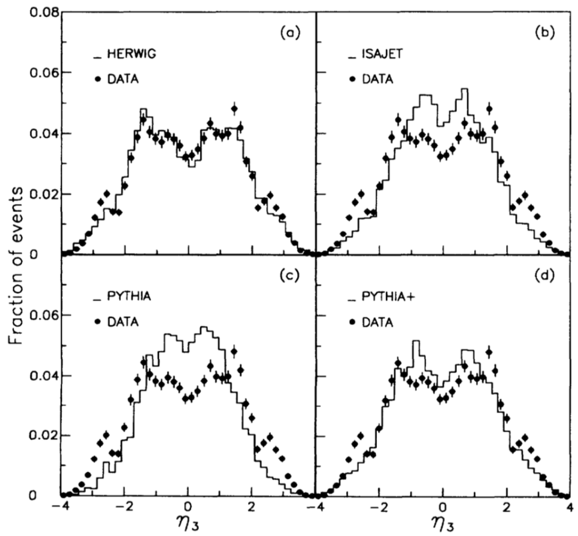

Figure 2.2: Observed η_3 distribution compared to the predictions of (a) HERWIG; (b) ISAJET; (c) PYTHIA; (d) PYTHIA + [2].

tion. This result shows the success of angular ordering calculation and its sanctification of QCD coherence.

2.2 The Lund Model

The hadronization is purely nonperturbative QCD. The popular models are the string and cluster model. This section focuses on the string model (Lund model) for explaining the QCD coherence phenomena. The basic idea of the string model starts from a color dipole which are compressed to a tubelike region (Figure 2.3).

The force between the dipoles is $V(r) \simeq kr$, where $k \simeq 1\,\text{GeV/fm}$. The full QCD should consider virtual fluctuation gluon and this gluons make

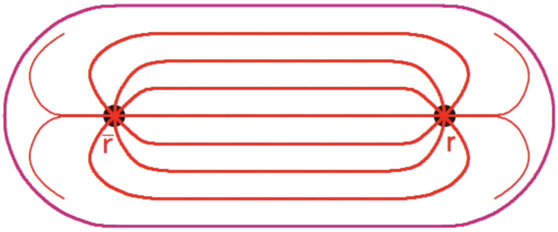

Figure 2.3: In QCD, for large charge separation, field lines are supposed to be compressed to a tubelike region: string [3].

nonperturbative string breaking (Figure 2.4). The Lund model repeats these string breakings for a large system and motion of quarks and anti-quarks in a $q\bar{q}$ systems and gives a simple but powerful picture of hadron production (Figure 2.5 (a)).

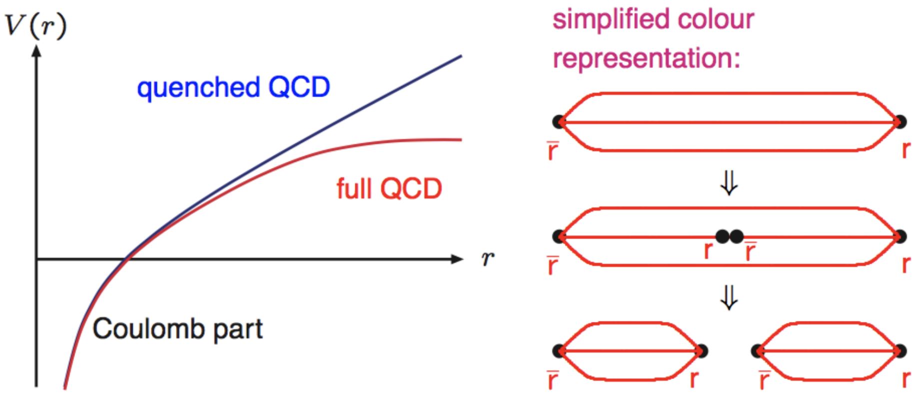

Figure 2.4: The full QCD potential needs to consider nonperturbative string breaking [3].

Another crucially important figure of the Lund model is the Lund gluon picture (Figure 2.5 (b)). The strings stretched from q (or $\bar{q}$) endpoint via

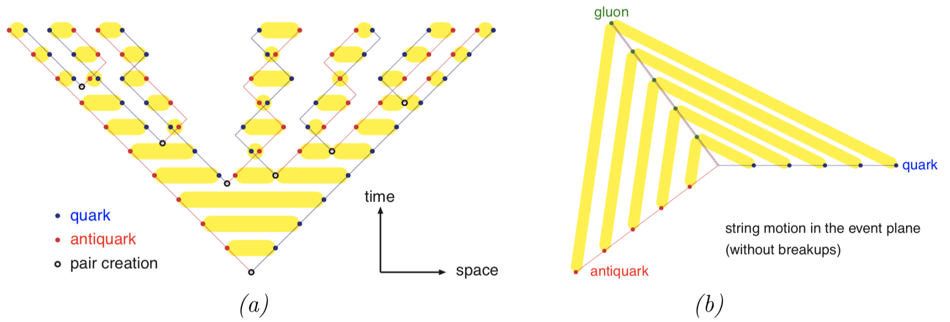

Figure 2.5: (a) String break up in a q$\bar{q}$ event. (b) String drawing in a q$\bar{q}$g event [4].

a number of gluons to $\bar{q}$ (or q) endpoint. This Lund gluon model successfully described q$\bar{q}$g 3-jet events. Figure 2.7 shows particle density distribution $(1/N)dN/d\phi$ in 3-jet events (q$\bar{q}$g). The comparison of three different models (string, independent, and cluster fragmentation) and data shows the string fragmentation model (Lund model) exactly describing the 3-jet events. Figure 2.6 shows 3-jet event structure for three different models.

2.3 Color Coherence

An important feature of quantum chromodynamics (QCD) is the effects of color coherence. Color coherence manifests as a color connection between the outgoing partons produced in hard interactions, leading to a suppression of particle radiation between the two leading jets of a three-jet event. The angular distribution of the third jet around the second jet was measured in e^-e^+ and pp collisions.

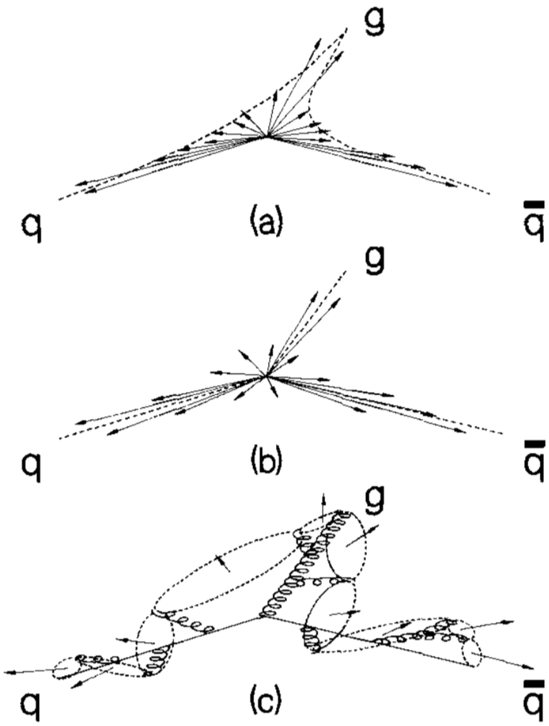

Figure 2.6: 3-jet event structure for (a) string fragmetation (SF), (b) independent fragmentation (IF), and (c) cluster fragmentation (CF) models. In (a) and (b), the arrow indicate the momentum space distribution of particles. The dashed curve in (a) represent strings stretched between the partons, in (b) they represent the parton directions. (c) shows the CF model quark-gluon shower (solid and curly lines) and clusters (dashed ellipses). The motion of the clusters is indicated by arrows; the resulting momentum space distribution of particles is similar to that in (a) for CF models exhibiting a depletion effect [5].

The color coherence effect was first observed from lepton collisions producing three-jet events. These three-jet events showed a suppression of particle radiation in the region between the two leading jets, but between the region of the second and third jets, an abundance of soft radiation existed [21]. This phenomenon was explained by using the color coherence effect. In hadron

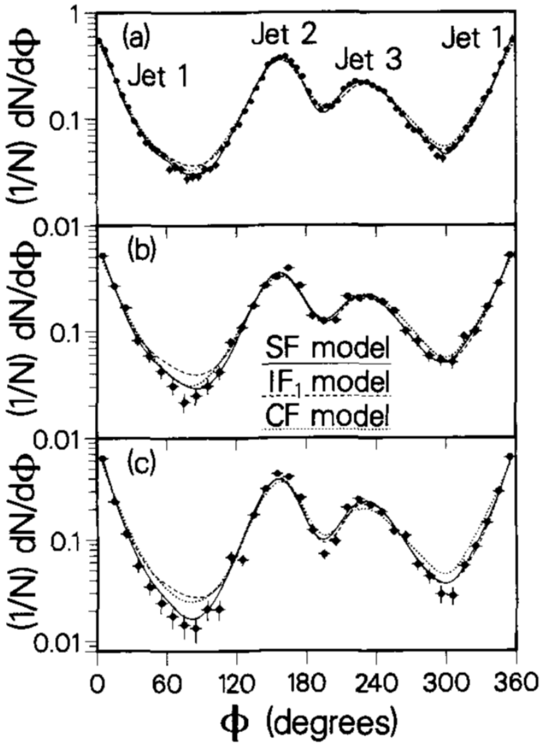

Figure 2.7: Particle density distribution $(1/N)dN/d\phi$ in 3-jet events for (a) all charged particles and photons, for (b) those charged particles and photons satisfying $0.3 < p_{out} < 0.5$ GeV/c and for (c) a heavy particle sample of charged and neutral kaons, protons, and lambdas. Also shown are the predictions of SF, IF_1, and CF models with full detector simulation [5].

collisions, the first color coherence effect was observed at the Tevatron [22]. The results from the Tevatron showed that the incoherent parton shower models were not describing the data well. However, the parton shower model which used angular ordering was shown to have a better agreement with the data. The result of the color coherence effect at $\sqrt{s} = 7\,\text{TeV}$ from the Compact Muon Solenoid (CMS) experiment [23] showed again that the Monte

Carlo (MC) models were not describing the data satisfactorily.

In both the Tevatron and the CMS analyses, the color coherence effect was measured using an angle observable β, which was shown to be sensitive to color coherence effects. The observable β is defined as the azimuthal angle of the third jet with respect to the second jet in (η, ϕ) space. Implicitly, this can be expressed as

$$\tan\beta = \frac{|\Delta\phi_{23}|}{\Delta\eta_{23}} \tag{2.1}$$

where the subscript number denotes a jet in p_T order, $\Delta\phi_{23} = \phi_3 - \phi_2$ (defined so that $-\pi \leq \Delta\phi_{23} \leq \pi$), $\Delta\eta_{23} = \text{sign}(\eta_2) \cdot (\eta_3 - \eta_2)$, and $0 \leq \beta \leq \pi$. The absolute value of $\Delta\phi_{23}$ in equation 2.1 and the sign of the pseudorapidity of the second jet, $\text{sign}(\eta_2)$, in the definition of $\Delta\eta_{23}$ are introduced to map symmetric configurations around $\Delta\phi_{23} = 0$ or $\eta = 0$ onto the same β value.

In a naive leading-order QCD model, when two partons are produced back-to-back in the transverse plane where of the two partons can radiate a third parton. Without the color coherence effects, the radiated third parton does not have a preferred direction. However, with the color coherence effects present, the third parton will tend to radiate in the event plane defined by the emitting parton and the beam's axis. Thus, the third jet population along the event plane (in particular near $\beta \approx 0$) will be enhanced while the population out of the plane ($\beta \approx \pi/2$) will be suppressed. The color coherence effects are expected to become stronger in the region between the second jet and the remnant when the angle between them becomes smaller. Therefore, a study of the β variable was performed in two situations: when the second jet was rather central ($|\eta_2| < 0.8$) and when the second jet was forward ($0.8 < |\eta_2| < 2.5$).

2.4 MC updates on color coherence at $\sqrt{s} = 7\,\text{TeV}$

The latest result for the color coherence effect is from the CMS experiment with a center-of-mass energy of 7 TeV. At the time, none of the MC models were shown to be able to describe the data successfully. This study shows the results of the latest MC models describing the color coherence effect and compares them to the CMS $\sqrt{s} = 7\,\text{TeV}$ data [24]. The latest MC models are able to describe the CMS data much more satisfactorily.

MC models at the particle level were compared with the unfolded data from the $\sqrt{s} = 7\,\text{TeV}$ CMS analysis. The anti-k_T [25] jet algorithm with cluster radius $R = 0.5$ (AK5) was used for jet clustering. PYTHIA 8 [26] (version 8.212) is a standard tool for the generation of events in high-energy collisions and includes soft and hard QCD processes using the standard $2 \rightarrow 2$ processes. The initial state radiation (ISR) and the final state radiation (FSR) algorithms are implemented for parton shower (PS) models based on a dipole-style p_T-ordered evolution. In this study, PYTHIA 8 was generated using the latest CUETP8M1 tune [27]. The CUETP8M1 tune is an alias for the MonashStar tune based on LHC data with the NNPDF2.34LO parton distribution function (PDF). MadGraph [28] (version 5.2.4) is a generator based on the matrix element (ME) method. In this study, the QCD processes $2 \rightarrow 3$ of MadGraph were done at a leading-order (LO) calculation by using the PS from pythia 8 tune CUETP8M1. powheg BOX [29, 30, 31] (version 2) is a generator based on the next-leading-order (NLO) ME method. A di-jet ($2 \rightarrow 2$ configuration) NLO calculation was done using the PS from pythia 8 tune CUETP8M1. Additionally, pythia 6 (version 6.424) was generated with tune Z2. This is the same tune used in the CMS $\sqrt{s} = 7\,\text{TeV}$ analysis for the comparison with the MC pythia 6 to data, but our pythia 6 version is updated. The pythia 6 generator results were similar to the CMS $\sqrt{s} = 7\,\text{TeV}$ results so we used it as a reference to show how much the other generators have improved. The color coherence effect has become an inherent feature of modern MC generators, such that the color coherence effect can no longer be disentangled in a simple manner as was the case with previous versions of pythia 6.

The color coherence effect is observed by using the β variable. The β variable is calculated by using the angle between the second jet and the third jet in $\eta - \phi$ space. Events with at least three jets with $p_{\text{T}} > 30\,\text{GeV}$ are selected, and selected jets are sorted by using their transverse momenta.

Table 2.1: Summary of the event selection

Event selection
$p_{T1} > 100\,\mathrm{GeV} > p_{T2} > p_{T3} > 30\,\mathrm{GeV}$
$\lvert\eta_1, \eta_2\rvert < 2.5$
$M_{12} > 220\,\mathrm{GeV}$
$0.5 < \Delta R_{23} < 1.5$

The leading jet and the second jet have a η cut of $|\eta_1|, |\eta_2| < 2.5$. A back-to-back di-jet event topology is selected by using the invariant mass of the leading jet and the second jet. To ensure that the second jet and the third jet are separated and well defined, we employed a cut in the $\eta - \phi$ space of $0.5 < \Delta R_{23} < 1.5$. The CMS $\sqrt{s} = 7\,\mathrm{TeV}$ data were selected in an integrated luminosity of 36 pb^{-1} with five different p_{T} threshold single-jet triggers, 30, 50, 70, 100 and 140 GeV. The leading jet was required to have a minimum p_{T} of 100 GeV for the 30 GeV single jet-trigger to be in the 99 % efficiency region. In the CMS $\sqrt{s} = 7\,\mathrm{TeV}$ data, 193,131 events were selected with the above event selections, of which events were in the central region ($|\eta_2| < 0.8$) and 105,621 events were in the forward region ($0.8 < |\eta_2| < 2.5$). The event selection is summarized in Table 2.1.

The $\Delta\eta_{23}$ and the $\Delta\phi_{23}$ MC distributions are shown in figures 2.8 and 2.9. The $\Delta\eta_{23}$ distribution is asymmetric. The negative $\Delta\eta_{23}$ is enhanced, especially in the forward region. This means that the third jet prefers to be produced between the second jet and the beam line as the second jet be-

Table 2.2: χ^2 deviations from data for the different MC models.

	$\lvert\eta_2\rvert < 0.8$	$0.8 < \lvert\eta_2\rvert < 2.5$
PYTHIA 8 CUETP8M1	2.0	3.2
MADGRAPH + PYTHIA 8	0.4	1.1
POWHEG + PYTHIA 8	1.1	1.5
PYTHIA 6 Z2	3.5	10.9

comes closer the beam line. The β distributions in the central ($\lvert\eta_2\rvert < 0.8$) and the forward ($0.8 < \lvert\eta_2\rvert < 2.5$) regions are shown in figure 2.10. The unfolded data with systematic and statistical uncertainties and the data from the latest MC models were compared at the particle level. The number of events for all MC data samples are much higher than the number of selected data event, so the MC statistical uncertainties are not visible in the figures. ME method-based MC generators are able to describe the data well. MADGRAPH has improved dramatically with the updated version. The POWHEG-generated $2 \rightarrow 2$ QCD process showed the performance of the NLO calculation. POWHEG is able to describe the data better in the forward region, rather than the central region. PYTHIA 8 has improved in the forward region, but the $\Delta\phi_{23}$ distribution is different from the other MC models. The $\Delta\phi_{23}$ distribution of PYTHIA 8 alone has an excess near 0, which enhanced the β distribution near 0 and π, particularly for the central region. The χ^2 values of the data and of the results from the MC models are summarized in Table 2.2.

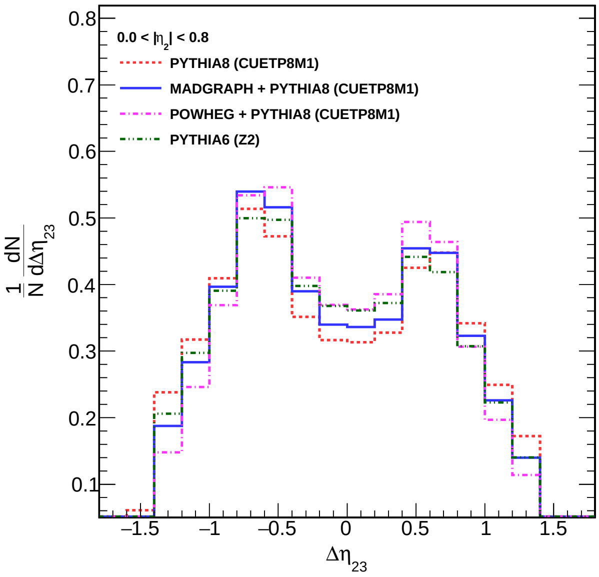

(a)

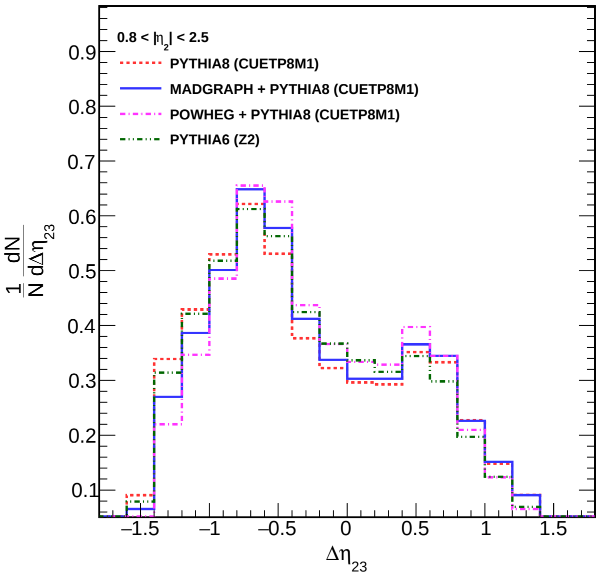

(b)

Figure 2.8: $\Delta\eta_{23}$ distributions for PYTHIA 8, MADGRAPH, POWHEG, and PYTHIA 6, (a) central ($|\eta_2| < 0.8$) and (b) the forward ($0.8 < |\eta_2| < 2.5$) regions.

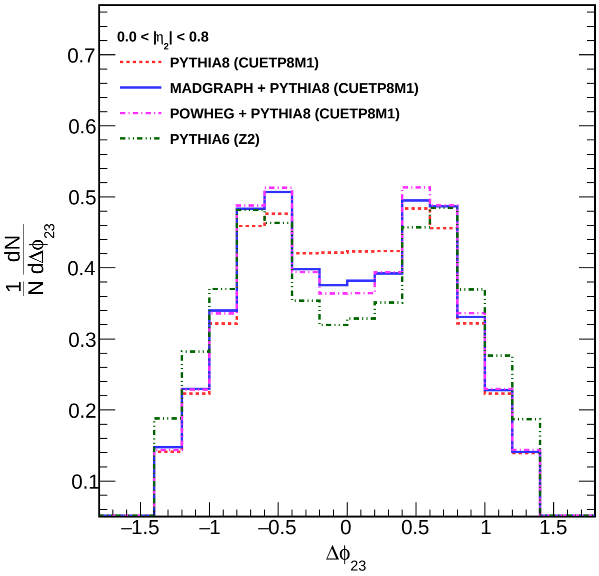

(a)

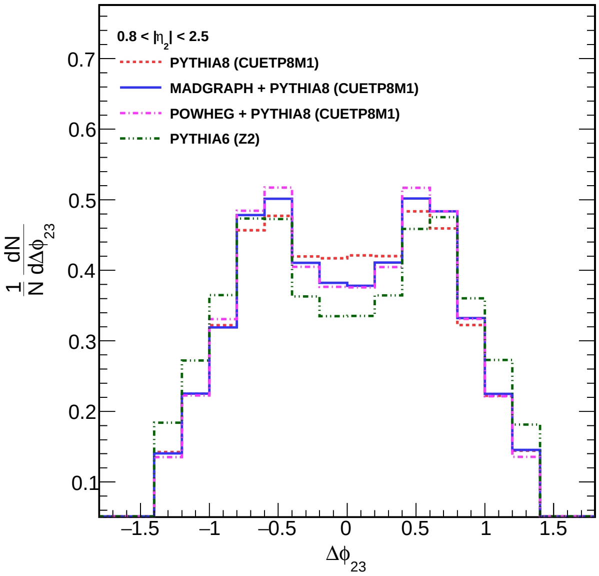

(b)

Figure 2.9: $\Delta\phi_{23}$ distributions for PYTHIA 8, MADGRAPH, POWHEG, and PYTHIA 6, (a) central ($|\eta_2| < 0.8$) and (b) the forward ($0.8 < |\eta_2| < 2.5$) regions.

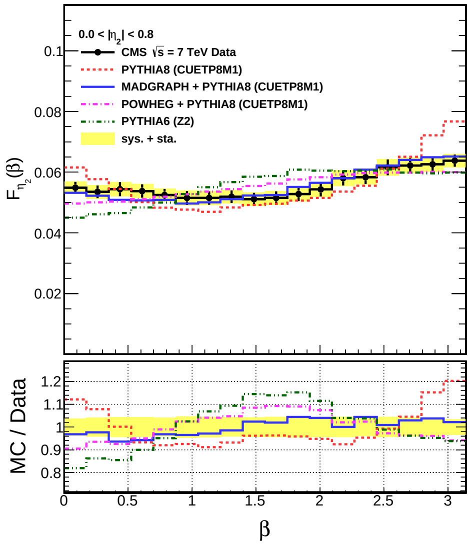

(a)

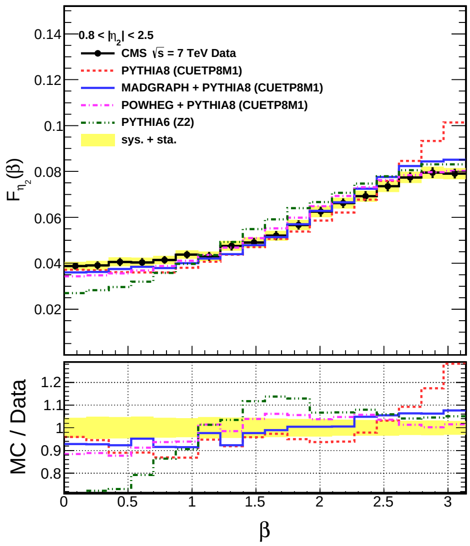

(b)

Figure 2.10: The β distributions of the unfolded data and their systematic and statistical uncertainties in yellow bands for the (a) central ($|\eta_2| < 0.8$) and (b) the forward ($0.8 < |\eta_2| < 2.5$) regions. MC models are compared at the particle level.

The results obtained using the latest MC models are compared to the $\sqrt{s} = 7\,\text{TeV}$ CMS color coherence results. Both the ME method generators MadGraph and powheg show better agreement with the data compared to pythia 8. MadGraph generated with a $2 \rightarrow 3$ QCD process for the LO calculation describes the data well in the central ($|\eta_2| < 0.8$) region. powheg with a $2 \rightarrow 2$ QCD process for the NLO calculation showed results comparable to those obtained using MadGraph, even though it was only generated with the $2 \rightarrow 2$ process. The latest ME-method-based MC generators have improved and describe the data much more successfully.

2.5 New Motivation

In perturbative QCD, calculation of the matrix element method is difficult and limited in multi-parton systems. When a quark pair is produced, one of the jets can radiate a gluon and in the fragmentation phase, the outgoing partons continue to interact with each other. The calculation for three jet event works well in the hard scattering region using the matrix element (ME) method, but the collinear and soft p_{T} radiation cases are limited. The parton shower (PS) method based on QED bremsstrahlung works will in the collinear and soft radiation cases, but is poor with hard scattering. Typically, both ME and PS are used together to accommodate both hard and soft p_{T} radiation cases. This study examines the PS and ME dominant regions. The

PS dominant regions are expected to be collinear and with soft p_{T} radiations, while the ME dominant region will produce hard p_{T} radiations with a large opening angle of radiation.

Three jet events were selected, with all jets having a requirement of $p_{\mathrm{T}} > 30$ GeV and $|y_{1,2}| < 2.5$. A much higher p_{T} requirement on the leading jet of 510 GeV was applied due to the trigger used in the CMS data. Ordering the three jets in descending transverse momentum, the kinematics of the second and third jets are used to make two observables which are used to separate the events into PS or ME dominant regions. The two observables are the second jet and the third jet p_{T} ratio and ΔR_{23} on rapidity - phi $(y - \phi)$ space.

According to these classifications, one can expect that the events in the soft p_{T} and small angle radiation region, as shown in figure 2.11 (a), can be well described by the PS scheme, while the events in the hard p_{T} and large angle radiation region, as shown in figure 2.11 (d), are to be described with the ME scheme. The events in figure 2.11 (b) and (c) are also of interest as both PS and ME affect the multi-jet phase space.

$$\frac{p_{\mathrm{T3}}}{p_{\mathrm{T2}}} \tag{2.2}$$

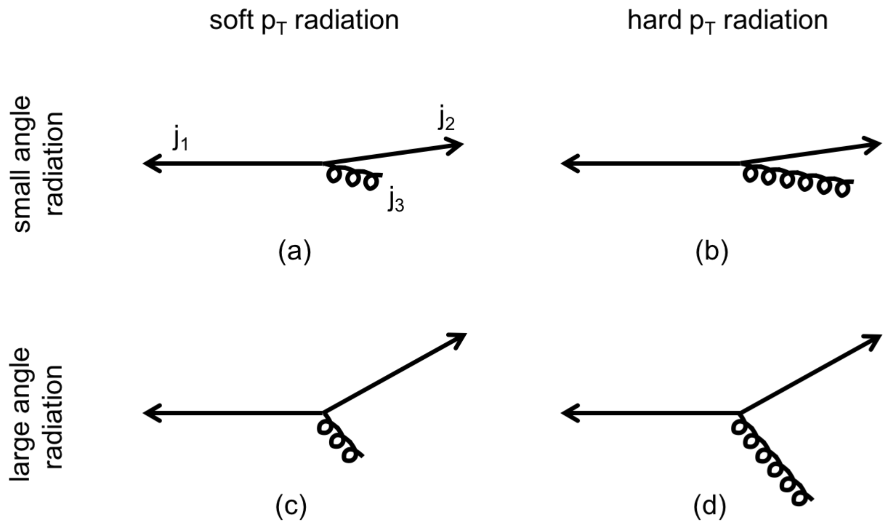

Figure 2.11: Four different cases in parton radiation. (a) soft p_T radiation with a small angle: small p_{T3}/p_{T2}, small ΔR_{23}, (b) hard p_T radiation with a small angle: large p_{T3}/p_{T2}, small ΔR_{23}, (c) large angle radiation with soft p_T: small p_{T3}/p_{T2}, large ΔR_{23}, (d) large angle radiation with hard p_T: large p_{T3}/p_{T2}, large ΔR_{23}.

$$\Delta R_{23} = \sqrt{(y_3 - y_2)^2 + (\phi_3 - \phi_2)^2} \tag{2.3}$$

The p_T ratio of the second jet and the third jet is used to classify the parton radiation as either soft near 0 or hard near 1. The ΔR_{23} is a representation of the parton radiation opening angle. Small ΔR_{23} is in the PS dominant and large ΔR_{23} is in the ME dominant regions. Using these observables, the PS and ME dominant region can be defined.

The table 2.3 shows each dominant region definition. The first PS dominant region is defined by ΔR_{23} smaller than 1, and the second PS dominant region is defined by jet p_{T} ratio smaller than 0.3. The first ME dominant region is defined by ΔR_{23} larger than 1. The second ME dominant region is defined by jet p_{T} ratio is grater than 0.6.

Table 2.3: The PS and ME dominant region.

region	observable	selection
PS dominant region	$p_{\mathrm{T3}}/p_{\mathrm{T2}}$	$\Delta R_{23} < 1$
	ΔR_{23}	$p_{\mathrm{T3}}/p_{\mathrm{T2}} < 0.3$
ME dominant region	$p_{\mathrm{T3}}/p_{\mathrm{T2}}$	$\Delta R_{23} > 1.0$
	ΔR_{23}	$p_{\mathrm{T3}}/p_{\mathrm{T2}} > 0.6$

The CMS detector collected the data used in this study at the LHC at the center of mass energy of 8 TeV and 13 TeV. The $\sqrt{s} = 8\,\mathrm{TeV}$ dataset contains 19.8 fb^{-1} taken during LHC run 1 in 2012 and the $\sqrt{s} = 13\,\mathrm{TeV}$ dataset contains 2.29 fb^{-1} taken during LHC run 2 in 2015.

3 CERN LHC and CMS Experiment

3.1 LHC

The Large Hadron Collider (LHC) [32] is a two-ring-superconducting-hadron accelerator and collider installed in the existing 26.7 km tunnel that was constructed between 1984 and 1989 for the CERN LEP machine. The LEP tunnel consists eight straight sections and eight arcs and lies between 45 m and 170 m below the surface on a plane inclined at 1.4 % sloping towards the Leman lake. Broadly speaking, the underground and surface structures at Points 1 and 5 for ATLAS and CMS, respectively, are new, while those for ALICE and LHCb, at Points 2 and 8, respectively, were originally built for LEP. A proton-proton and heavy ions accelerator and collider built by the European Organisation for Nuclear Research (CERN) in the Geneva region under the border between France and Switzerland. The main goal of the LHC is the expected discovery of the Higgs boson in order to complete the Standard Model (SM) and to study Beyond the Standard Model (BSM) scenarios, in particular to verify or refute the hypothesis of the existence of Super-symmetric particles and to search for new phenomena such as Dark Matter. At the LHC, part of the physics program is also dedicated to heavy ion physics with the main goal of studying the weak bound among quarks and gluons under conditions similar to those in the early universe, the so-called quark-gluon plasma. The former is important in order to produce new potentially heavy particles and to study their features in depth, while the latter is related to the rate of interactions occurring, and therefore with the production of rare particles. Being a particle-particle collider, there are two rings with counter-rotating beams, unlike particle-antiparticle colliders that can have both beams sharing the same phase space in a single ring. The tunnel geometry was originally designed for the electron-positron machine LEP, and there were eight crossing points flanked by long straight sections of RF cavities that compensated the high synchrotron radiation losses. A proton machine such as LHC does not have the same synchrotron radiation problem and would, ideally, have longer arcs and shorter straight sections for the same circumference, but accepting the tunnel "as built" was the cost-effective solution. The tunnel in the arcs has a finished internal diameter of 3.7 m, which makes it extremely difficult to install two completely separate proton rings. This hard limit on space led to the adoption of the twinbore magnet design that was proposed by John Blewett at the Brookhaven laboratory in 1971. At that time, it was known as the "two-in-one" superconducting magnet design and was put forward as a cost-saving measure, but in the case of the LHC, the overriding reason for adopting this solution is the lack of space in the tunnel. However, research was moving towards operation at 2 K and lower, to take advantage of the increased temperature margins and the enhanced heat transfer at the solid-liquid interface and in the bulk liquid.

The LHC luminosity design desires to performance as

$$L = \frac{N_b^2 n_b f_{\text{rev}} \gamma_r}{4\pi \varepsilon_n \beta_*} F \tag{3.1}$$

where N_b is the number of particles per bunch, n_b the number of bunches per beam, f_{rev} the revolution frequency, $\gamma_r = 1/\sqrt{1 - v^2/c^2}$ the relativistic gamma factor, ε_n the normalized transverse beam emittance, β_* the beta function at the collision point, and F the geometric luminosity reduction factor due to the crossing angle at the interaction point (IP):

$$F = \left(1 + \left(\frac{\theta_c \sigma_z}{2\sigma_*}\right)^2\right)^{-1/2} \tag{3.2}$$

Where θ_c is the full crossing angle at the IP, σ_z the RMS bunch length, and σ_* the transverse RMS beam size at the IP. The above expression assumes round beams, with $\sigma_z \ll \beta$, and with equal beam parameters for both

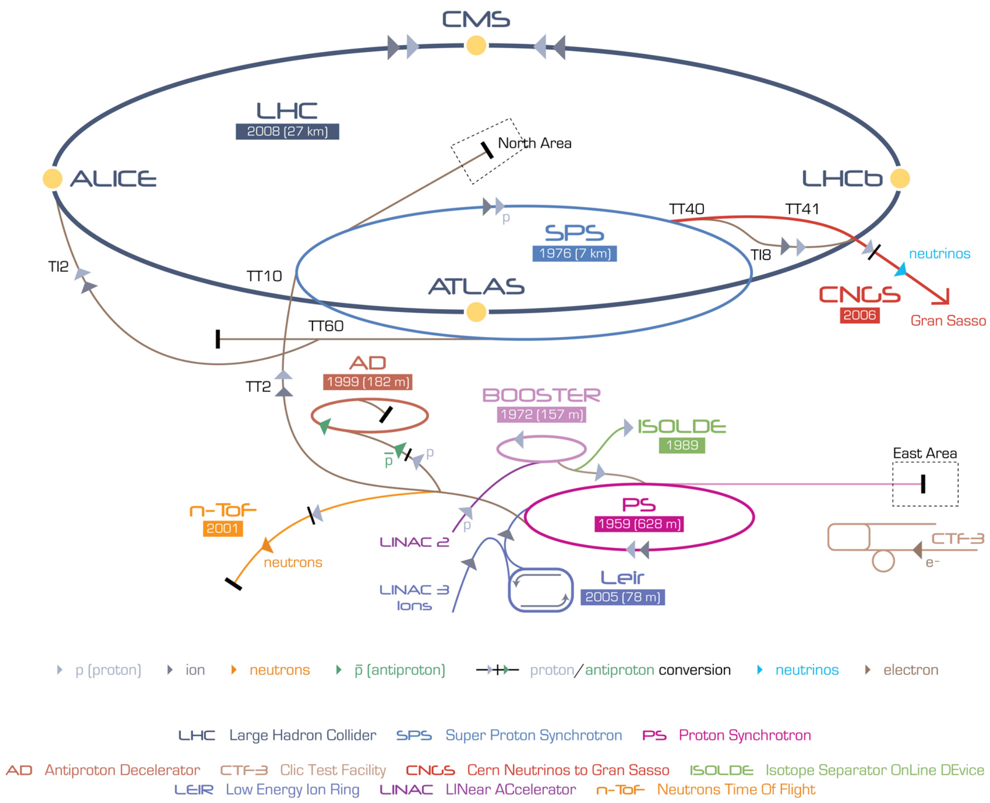

Figure 3.1: Illustration of the CERN accelerator complex [6].

beams. The exploration of rare events in the LHC collisions therefore requires both high beam energies and high beam intensities.

The LHC is supplied with protons from the injector chain Linac2 — Proton Synchrotron Booster (PSB) — Proton Synchrotron (PS) — Super Proton Synchrotron (SPS), as shown in figure 3.1. PSB, PS, and SPS also provide particle beams to smaller experiments located at CERN, such as the Isotope mass Separator On-Line facility (ISOLDE) in the case of PSB, the Antiproton Decelerator (AD) ring for PS, and several fixed-target ex-

Table 3.1: Energy of the Accelerators

Accelerator	Energy
Proton Synchrotron Booster (PSB)	1.4 GeV
Proton Synchrotron (PS)	26 GeV
Super Proton Synchrotron (SPS)	450 GeV

periments in the so-called North Area as well as the Proton Driven Plasma Wakefield Acceleration Experiment (AWAKE) for the SPS.

3.2 CMS

The central feature of the CMS apparatus is a superconducting solenoid of 6 m internal diameter, providing a magnetic field of 3.8 T. Within the solenoid volume, are the silicon pixel and strip tracker, a lead tungstate crystal electromagnetic calorimeter (ECAL), and a brass and scintillator hadron calorimeter (HCAL), each composed of a barrel and two end cap sections. Forward calorimeters extend the pseudo-rapidity (η) overage provided by the barrel and end cap detectors to the region $3.0 < |\eta| < 5.2$. Muons are measured in gas ionization detectors embedded in the steel flux return yoke outside the solenoid. In the region $|\eta| < 1.74$, the HCAL cells have widths of 0.087 in η and 0.087 radians in azimuth (ϕ). In the $\eta - \phi$ plane, and for $|\eta| < 1.48$, the HCAL cells map onto ECAL crystals arrays to form calorimeter towers projecting radially outwards from close to the nominal interaction point. At larger values of η, the size in rapidity of the towers increases and the matching ECAL arrays contain fewer crystals. Within each tower, the energy deposits in ECAL and HCAL cells are summed to define the calorimeter tower energies, subsequently used to provide the energies and directions of hadronic jets. The particle-flow (PF) event algorithm [33], reconstructs and identifies each individual particle with an optimized combination of information from the various elements of the CMS detector. The energy of the photons are directly obtained from the ECAL measurement. The energy of electrons is determined by a combination of the electron momentum at the primary interaction vertex as determined by the tracker, the energy of the corresponding ECAL cluster, and the energy sum of all bremsstrahlung photons spatially compatible with originating from the electron track. The momentum of muons is obtained from the curvature of the corresponding track. The energy of charged hadrons is determined from a combination of their momenta measured in the tracker and the matching ECAL and HCAL energy deposits, corrected for zero-suppression effects and for the response function of the calorimeters to hadronic showers. Finally, the energy of neutral hadrons is obtained from the corresponding ECAL and HCAL energy. When combining information from the entire detector, the jet energy resolution typically amounts to 8 % at 100 GeV, and 4 % at 1 TeV, to be compared to about 40 %, 12 %, and 5 % obtained when the ECAL and HCAL alone are used [34]. A more detailed description of the CMS detector, together with a definition of the coordinate system used and the relevant kinematic variables, can be found in Ref. [35].

4 Event Selection

In this chapter, the data sets, and event selection are described. Data recorded with the CMS detector have been used for the two center-of-mass energies of 8 TeV and 13 TeV. Good luminosity block record selects events from the $\sqrt{s} = 8\,\text{TeV}$ and 13 TeV data sets. The event selection considers dijet topology, and the 3rd jet is from final state radiation of the 2nd jet.

4.1 Data Samples

In this analysis, the main physics object is the jet. Jets are reconstructed by the anti-k_T jet clustering algorithm which is implemented in the fastjet package [25, 36]. The clustering radius is 0.5 (AK5) for $\sqrt{s} = 8\,\text{TeV}$ and 0.4 (AK4) for $\sqrt{s} = 13\,\text{TeV}$. The anti-$k_\text{T}$ algorithm satisfies collinear safety and infrared safety. CMS uses the particle flow (PF) reconstruction [37, 38] which can identify and reconstruct each particle individually in every event, by optimal combining information from all the sub-detectors. In high pileup environments, there are many unwanted particles from the additional interaction. The charged hadron subtraction (CHS) technique can remove unwanted particles to calorimeter and tracker with pileup vertex. The jet selection is applied loose jet ID.

- Neutral Hadron Fraction < 0.99
- Neutral EM Fraction < 0.99
- Number of Constituents > 1
- for $|\eta| < 2.4$ in addition apply
  - Charged Hadron Fraction > 0
  - Charged Multiplicity > 0
  - Charged EM Fraction < 0.99

Jets are corrected in both data and MC using the latest jet energy correction (JEC) available Winter14_V8 for $\sqrt{s} = 8\,\text{TeV}$ and Fall15_25nsV2 for $\sqrt{s} = 13\,\text{TeV}$ [39].

4.1.1 Data and MC sets for $\sqrt{s} = 8$ TeV

The data is collected at CMS at center-of-mass energy of 8 TeV during 2012 and the total integrated luminosity is 19.8 fb^{-1}. In this analysis, the bellow data sets and luminosity block are used. The good luminosity section is selected and recorded in the official JASON format file.

The CMSSW_5_3_7_patch5 reconstructs the AOD dataset with global tag FT_R_53_V18::All and the PAT objects that are used in this analysis are produced in CMSSW_5_3_30. The table 4.2 shows all $\sqrt{s} = 8\,\text{TeV}$ data sets, number of events, and integrated luminosity.

In this analysis, two different physics model Monte Carlos (MC) are used for the study of detector effects. PYTHIA 8 and MADGRAPH generate MC events with full CMS detector simulation. CMSSW_5_3_2_patch5 simulates both MC events with global tag START53_V7A::All. PYTHIA 8 is used to the tune 4C for Underlying Event (UE). The table 4.4 and the table 4.5 show p_{T} slice bins, number of events, and cross section.

The MC sample is divided into multiple samples generating different bins of p_{T}. The considered samples can be accessed through the following names:

4.1.2 Data and MC sets for $\sqrt{s} = 13$ TeV

The data is collected at CMS at center-of-mass energy of 13 TeV during 2015 with 25 ns bunch crossing and the total integrated luminosity is 2.29 fb^{-1}. In this analysis the bellow data sets and luminosity block are used.

The CMSSW_7_6_X reconstructs These AOD datasets with global tag 76X_dataRun2_v15 and the PAT objects used in this analysis were produced in CMSSW_7_6_3. The table 4.7 shows number of events and integrated luminosity.

Table 4.1: List of $\sqrt{s} = 8\,\text{TeV}$ CMS Data sets and luminosity block

/Jet/Run2012A-22Jan2013-v1/AOD
/JetHT/Run2012B-22Jan2013-v1/AOD
/JetHT/Run2012C-22Jan2013-v1/AOD
/JetHT/Run2012D-22Jan2013-v1/AOD
Cert_190456-208686_8TeV_22Jan2013ReReco_Collisions12_JSON.txt

Table 4.2: List of $\sqrt{s} = 8\,\text{TeV}$ Data sets

Data	Number of Events	Integrated luminosity (fb^{-1})
Run2012A	9400333	0.8893
Run2012B	15513284	4.429
Run2012C	25774250	7.14769
Run2012D	27572330	7.318

Table 4.3: List of $\sqrt{s} = 8\,\text{TeV}$ CMS MC sets

/QCD_Pt-XXXtoXXX_Tune4C_8TeV_pythia8/Summer12_DR53X-PU_S10_START53_V7A-v1/AODSIM
/QCD_HT-XXXToXXX_TuneZ2star_8TeV-madgraph-pythia/Summer12_DR53X-PU_S10_START53_V7A-v1/AODSIM

Table 4.4: List of PYTHIA 8 sets ($\sqrt{s} = 8\,\text{TeV}$)

p_{T} bin (GeV)	Number of Events	Cross section (pb)
170 - 300	800000	37974.99
300 - 470	500000	1938.868
470 - 600	500000	124.8942
600 - 800	500000	29.55049
800 - 1000	400000	3.871308
1000 - 1400	400000	0.8031018
1400 - 1800	200000	0.03637225
1800 - Inf.	200000	0.00197726

Table 4.5: List of MADGRAPH sets ($\sqrt{s} = 8\,\text{TeV}$)

p_{T} bin (GeV)	Number of Events	Cross section (pb)
100 - 250	52000000	1.036E7
250 - 500	28229933	276000.0
500 - 1000	32000000	8426.0
1000 0 Inf.	13960000	204.0

Table 4.6: List of $\sqrt{s} = 13\,\text{TeV}$ CMS Data sets and luminosity block

/JetHT/Run2015C_25ns-16Dec2015-v1/MINIAOD
/JetHT/Run2015D-16Dec2015-v1/MINIAOD
Cert_13TeV_16Dec2015ReReco_Collisions15_25ns_JSON.txt

In this analysis, two different physics model Monte Carlo (MC) were used for the study of detector effects. PYTHIA 8 and MADGRAPH generated MC events with full CMS detector simulation. CMSSW_7_6_3 simulated both MC events with global tag 76X_mcRun2_asymptotic_v12. PYTHIA 8 is used the tune CUETP8M1 for UE. The table 4.9 and the table 4.10 show p_{T} slice bins, number of events, and cross section.

4.2 Jet reconstruction and event selection

In this Section, the physics objects which are used and the requirements in event selection are briefly explained. The main physics objects of this study is jet which are Particle Flow (PF) reconstructed with the anti-k_{T} clustering. It tends to cluster particles starting from highest p_{T}, and to produce jets preferably with circular shape. The Particle Flow (PF) jets are reconstructed by clustering the four-momentum vectors of PF candidates. The PF jet momentum and spatial resolutions are greatly improved with respect to calorimeter jets, as the use of the tracking detector and the high granularity of ECAL allows resolution and measurement of charged hadrons and photon inside a jet, which together constitute about 85 % of the jet energy. In order to reduce pileup contribution to the reconstructed jets, the novel technique of charged hardron subtraction (CHS) is considered. The presence of pileup results in unwanted calorimetric energy depositions and extra tracks. The CHS reduces theses effects by removing tracks identified as originating from pileup vertices. The pileup from charged particles are reduced by identifying which vertex the charged PF candidates originate from and removing those unambiguously associated to pileup vertices before clustering jets and missing transverse energy. The leading primary vertex (PV) is chosen based on the largest sum of squares of the track transverse momenta associated to the vertex.

The good PV selection is required for each event.

- Require at least one PV
- Require the z component of PV to be $|z(PV)| < 24$ cm
- Require the radius in x-y plane of PV to be $\rho < 2$ cm
- Require the vertex fit NDF > 4

Reconstructed jets require small energy corrections because the detector response to particles are not linear and uniform. To obtain true particle or parton energy, there are several energy corrections that are applied for data and MC. First, jet energy correction (JEC), which are offset correction removing energy from pileup events. Zero-bias events calculate this correction, and it has the dependency of luminosity. Second, JEC in MC - truth correction which creates a uniformity response over jet p_{T} and η. This correction is derived as a function of jet p_{T} and η with dijet events. Lastly, JEC is jet energy scale correction for the remaining small energy differences between data and MC. This jet energy scale (JES) correction is calculated using dijet, photon + jet and Z + jet events.

The missing E_{T} ($E_{\mathrm{T}}^{\mathrm{miss}}$) cut is used to reject background events from high $E_{\mathrm{T}}^{\mathrm{miss}}$ like Z/W + jet. This cut value is $E_{\mathrm{T}}^{\mathrm{miss}}/\sum E_{\mathrm{T}} < 0.3$.

This analysis selects at least three jets event for measuring the correlation between the second and third jet. Jets are sorted by their transverse momentum in decreasing order ($p_{\mathrm{T}1} > p_{\mathrm{T}2} > p_{\mathrm{T}3}$). The third jet is from radiation of the second jet and the first jet and the second jet satisfies dijet event topology. For a selection of dijet events, delta ϕ between the first jet and second jet ($\Delta\phi_{12}$) cut is used for selecting dijet event. First jet and second jet rapidity maximum range is $\pm$ 2.5. The third jet is radiation from the second jet. So the ΔR of the third jet and the second jet in rapidity-phi space ($y - \phi$) is smaller than 1.5. Also, $\Delta R_{23} < R_{\text{jet}} + 0.1$ is excluded to avoid AK algorithm bias, the “cookie-cutter” effect.

This analysis uses the non-prescaled trigger [40] shown in table 4.11, and this trigger efficiency is over than 99% at 507 GeV for leading jet.

One of the observable is the p_{T} ratio of the second jet and the third jet. When the ratio is near 1, the second jet and the third jet can changed their p_{T} order because the p_{T} of the second jet and the third jet is similar and reconstruction is not perfect. The p_{T} ratio range, 0.9 to 1.0 is excluded for avoid mismatching between particle level and detector level. To avoid minimum p_{T} cut bias, $p_{\text{T3}}/p_{\text{T2}} < 0.1$ is excluded.

Finally, all event selections are summarized in table 4.12, and table 4.13 shows number of events entries.

Table 4.7: List of $\sqrt{s} = 13\,\text{TeV}$ Data sets

Data	Number of Events	Integrated luminosity (fb^{-1})
Run2015C	1856426	0.0177
Run2015D	68971060	2.277

Table 4.8: List of $\sqrt{s} = 13\,\text{TeV}$ CMS MC sets

/QCD_Pt_XXXtoXXX_TuneCUETP8M1_13TeV_pythia8/ RunIIFall15MiniAODv2-PU25nsData2015v1_76X_mcRun2_asymptotic_ v12-v1/MINIAODSIM
/QCD_HTXXXtoXXX_TuneCUETP8M1_13TeV-madgraphMLM-pythia8/ RunIIFall15MiniAODv2-PU25nsData2015v1_76X_mcRun2_asymptotic_ v12-v1/MINIAODSIM

Table 4.9: List of PYTHIA 8 sets ($\sqrt{s} = 13\,\text{TeV}$)

p_T bin (GeV)	Number of Events	Cross section (pb)
170 - 300	6918748	117276
300 - 470	5968960	7823
470 - 600	3977770	648.2
600 - 800	3979884	186.9
800 - 1000	3973224	32.293
1000 - 1400	2953982	9.4183
1400 - 1800	395725	0.84265
1800 - 2400	393760	0.114943
2400 - 3200	398452	0.00682981
3200 - Inf.	391108	0.000165445

Table 4.10: List of MADGRAPH sets ($\sqrt{s} = 13\,\text{TeV}$)

p_{T} bin (GeV)	Number of Events	Cross section (pb)
200 - 300	18822308	1717000
300 - 500	17040053	351300
500 - 700	19701790	31630
700 - 1000	15575940	6802
1000 - 1500	5085104	1206
1500 - 2000	3952170	120.4
2000 - Inf.	1981228	25.25

Table 4.11: Trigger

8 TeV	HTL_PFJet320
13 TeV	HLT_PFJet450

Table 4.12: Selection criteria

$p_{\mathrm{T}1} > 510\,\mathrm{GeV} > p_{\mathrm{T}2} > p_{\mathrm{T}3} > 30\,\mathrm{GeV}$
$0.1 < p_{\mathrm{T}3}/p_{\mathrm{T}2} < 0.9$
$R_{\mathrm{jet}} + 0.1 < \Delta R_{23} < 1.5$
$\lvert\Delta\phi_{12} - \pi\rvert < 1$
$\lvert y_1\rvert, \lvert y_2\rvert < 2.5$
$E_{\mathrm{T}}^{\mathrm{miss}}/\sum E_{\mathrm{T}} < 0.3$

Table 4.13: Number of selected events

Observables	Criteria	Number of selected data	
		$\sqrt{s} = 8\,\mathrm{TeV}$	$\sqrt{s} = 13\,\mathrm{TeV}$
$p_{\mathrm{T}3}/p_{\mathrm{T}2}$	$R_{jet} + 0.1 < \Delta R_{23} < 1.0$	475,399	302,219
	$1.0 < \Delta R_{23} < 1.5$	407,457	205,797
ΔR_{23}	$0.1 < p_{\mathrm{T}3}/p_{\mathrm{T}2} < 0.3$	426,537	226,524
	$0.6 < p_{\mathrm{T}3}/p_{\mathrm{T}2} < 0.9$	167,736	107,042

5 Detector effects: Data Unfolding

The data unfolding is required to remove migration effects for the measurement of distributions in high energy physics (HEP). The migration effects and limited acceptance leads to indirect measurement. Recently, a data unfolding process is necessary for measurements in HEP. The unfolded data can be compared directly with other experiment results and theoretical predictions.

5.1 Detector level comparison

This section shows the detector level comparisons. All distribution are normalized by the number of the entries and the bin width. The detector level systematic uncertainties are calculated with jet energy scale (JES), jet energy resolution (JER), and pileup (PU). The data is compared with two MC prediction using the PS and the ME method. The $\sqrt{s} = 8\,\text{TeV}$ data jets are reconstructed with the AK5 jet, and the $\sqrt{s} = 13\,\text{TeV}$ data jets use the AK4 jet. The detector level distributions include several detector effects which are the jet position and the jet energy smearing. The precise detector level comparisons are needed to understand the unfolding.

5.1.1 $\sqrt{s} = 8$ TeV

The $\sqrt{s} = 8$ TeV data is compared with MadGraph + pythia 6 and pythia 8. pythia 6 uses tune z2 for MadGraph parton shower, but pythia 8 uses tune 4C. In the p_T distributions, the second jet p_T distribution shows the discrepancy between MadGraph and pythia 8. Also, in the rapidity distributions, the leading jet rapidity distribution of pythia 8 (Figure 5.4 (d)) shows dump at the 0 regions.

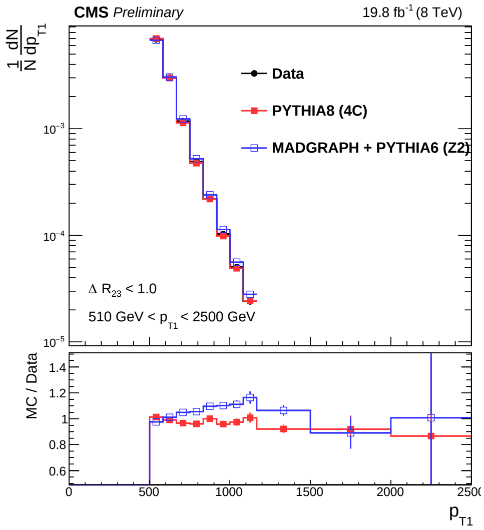

(a)

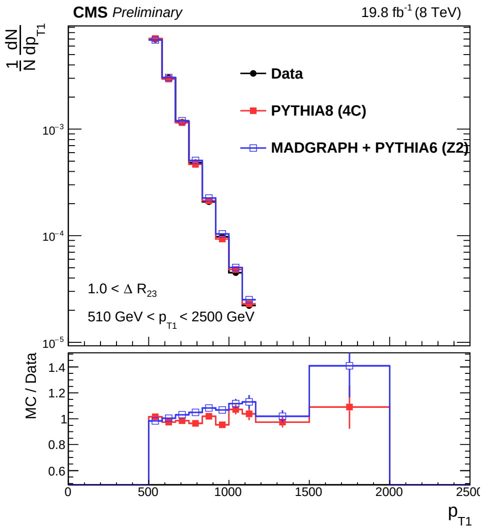

(b)

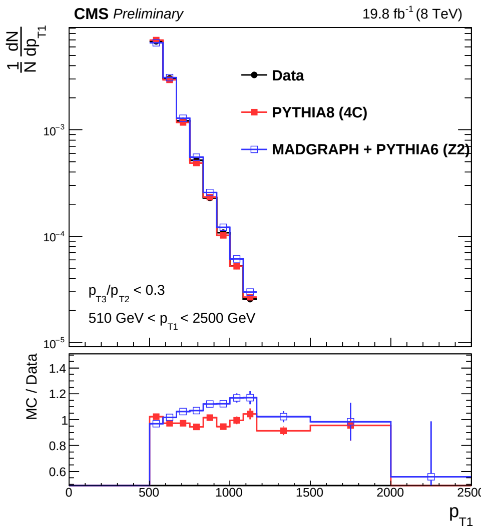

(c)

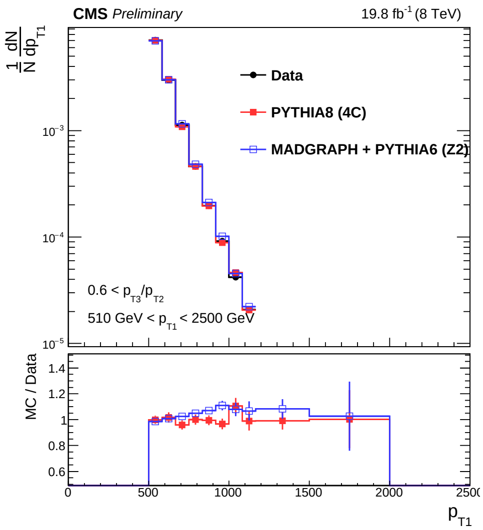

(d)

Figure 5.1: $\sqrt{s} = 8$ TeV data and theoretical predictions comparisons. (a) p_{T1} distribution for the events with a small angle radiation ($\Delta R_{23} < 1.0$), (b) p_{T1} distribution for the events with a large angle radiation ($\Delta R_{23} > 1.0$), (c) p_{T1} distribution for soft p_{T} radiation case ($p_{\mathrm{T3}}/p_{\mathrm{T2}} < 0.3$), (d) p_{T1} distribution for hard p_{T} radiation case ($p_{\mathrm{T3}}/p_{\mathrm{T2}} > 0.6$).

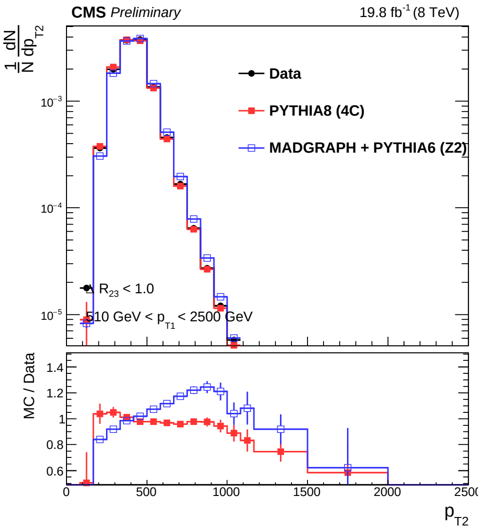

(a)

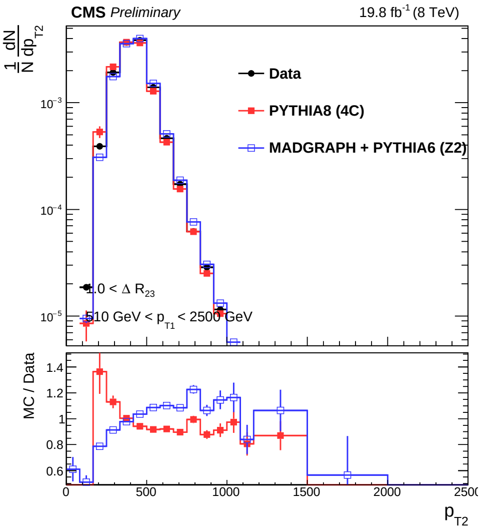

(b)

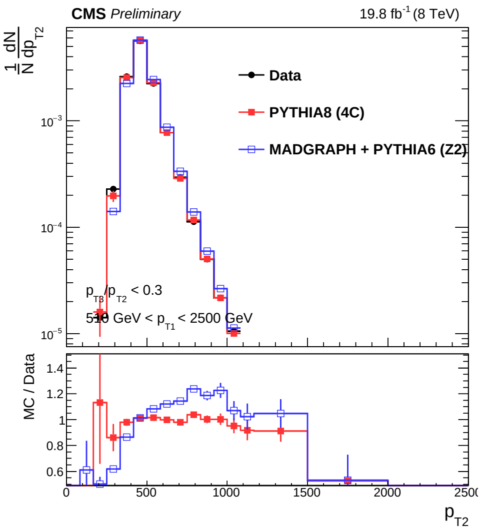

(c)

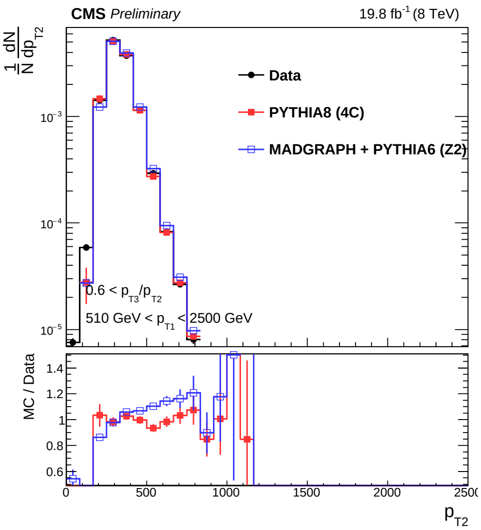

(d)

Figure 5.2: $\sqrt{s} = 8$ TeV data and theoretical predictions comparisons. (a) p_{T2} distribution for the events with a small angle radiation ($\Delta R_{23} < 1.0$), (b) p_{T2} distribution for the events with a large angle radiation ($\Delta R_{23} > 1.0$), (c) p_{T2} distribution for soft p_{T} radiation case ($p_{\mathrm{T3}}/p_{\mathrm{T2}} < 0.3$), (d) p_{T2} distribution for hard p_{T} radiation case ($p_{\mathrm{T3}}/p_{\mathrm{T2}} > 0.6$).

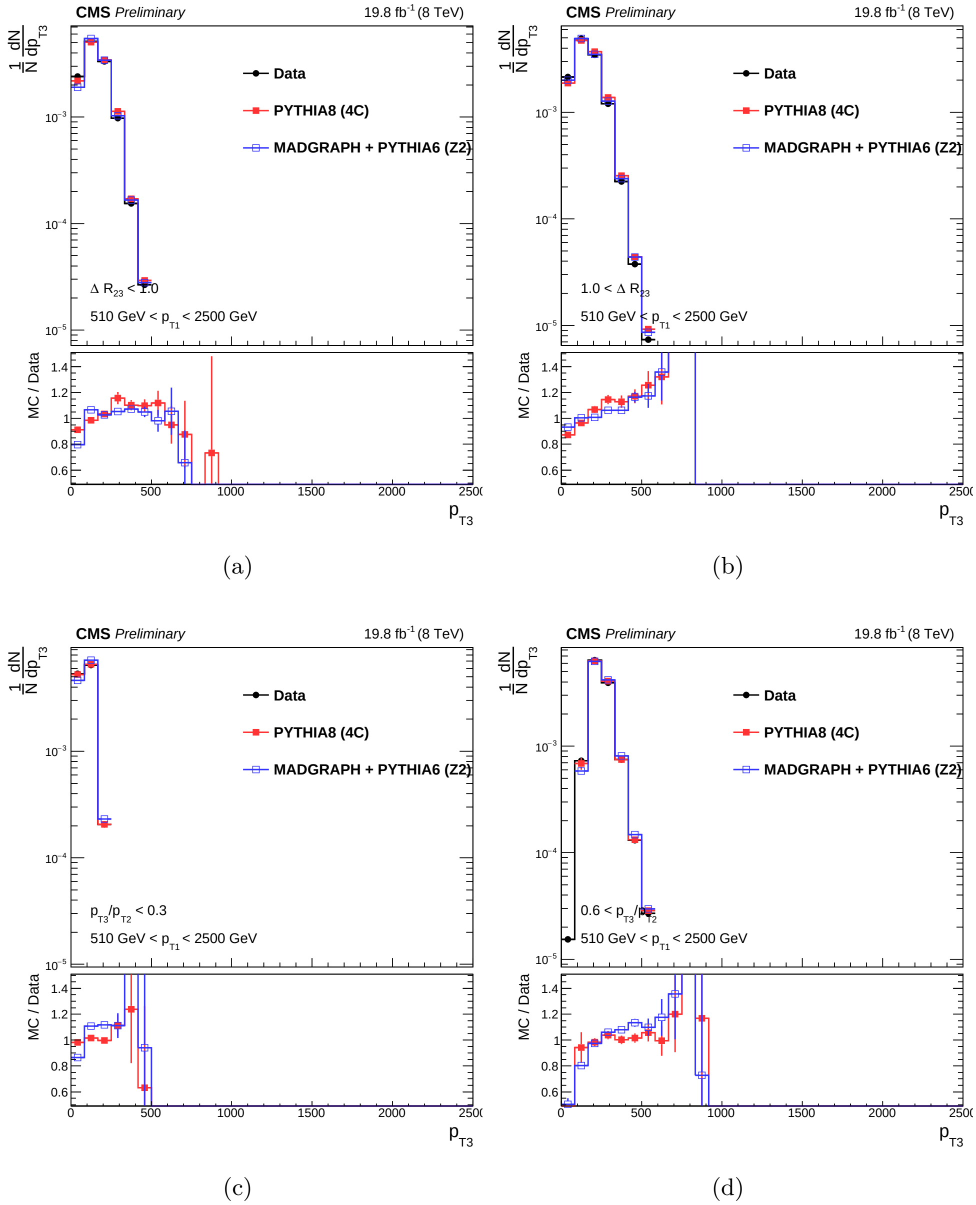

Figure 5.3: $\sqrt{s} = 8$ TeV data and theoretical predictions comparisons. (a) p_{T3} distribution for the events with a small angle radiation ($\Delta R_{23} < 1.0$), (b) p_{T3} distribution for the events with a large angle radiation ($\Delta R_{23} > 1.0$), (c) p_{T3} distribution for soft p_{T} radiation case ($p_{\mathrm{T3}}/p_{\mathrm{T2}} < 0.3$), (d) p_{T3} distribution for hard p_{T} radiation case ($p_{\mathrm{T3}}/p_{\mathrm{T2}} > 0.6$).

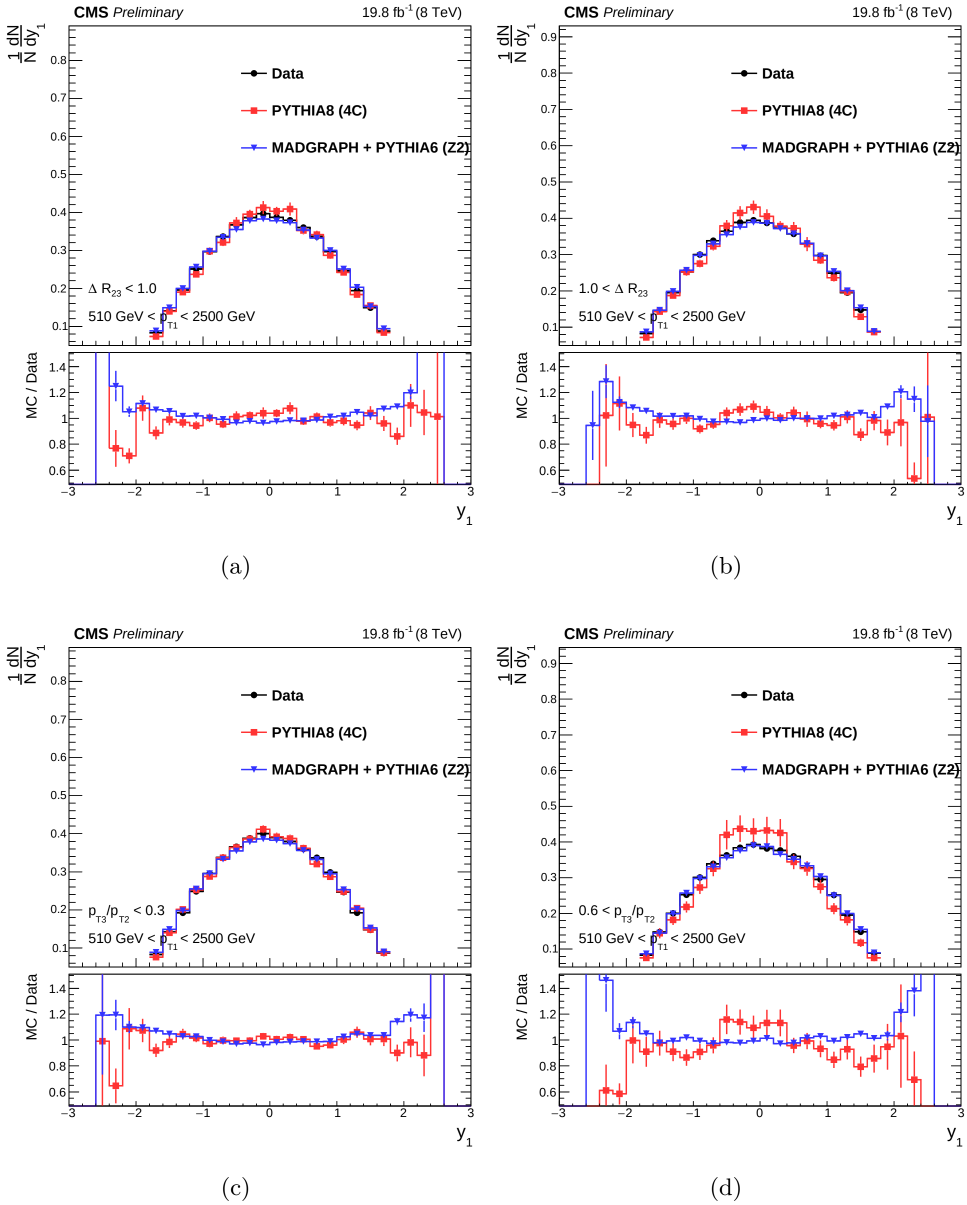

Figure 5.4: $\sqrt{s} = 8$ TeV data and theoretical predictions comparisons. (a) y_1 distribution for the events with a small angle radiation ($\Delta R_{23} < 1.0$), (b) y_1 distribution for the events with a large angle radiation ($\Delta R_{23} > 1.0$), (c) y_1 distribution for soft p_{T} radiation case ($p_{\mathrm{T3}}/p_{\mathrm{T2}} < 0.3$), (d) y_1 distribution for hard p_{T} radiation case ($p_{\mathrm{T3}}/p_{\mathrm{T2}} > 0.6$).

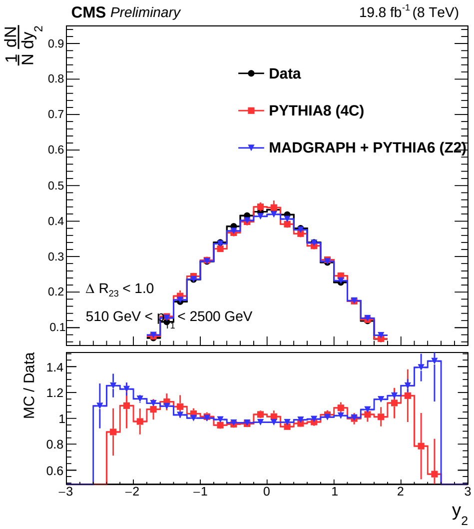

(a)

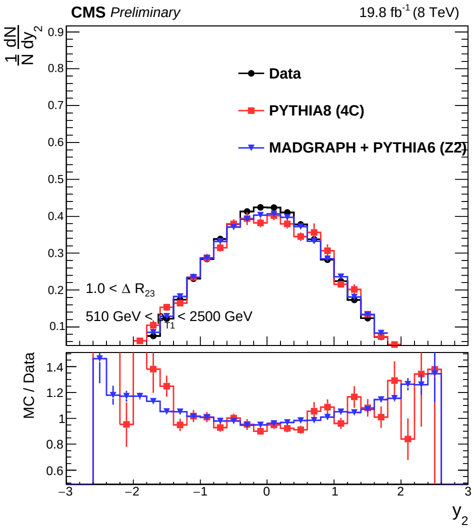

(b)

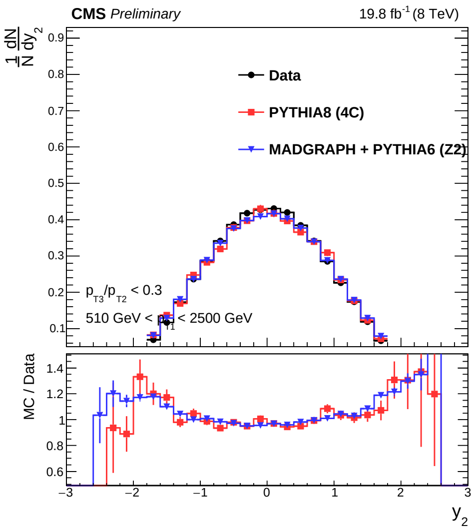

(c)

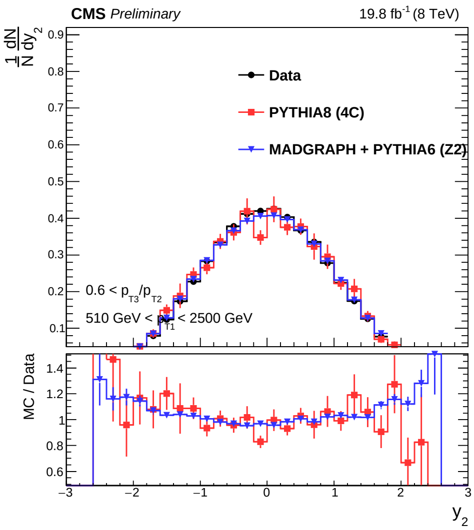

(d)

Figure 5.5: $\sqrt{s} = 8$ TeV data and theoretical predictions comparisons. (a) y_2 distribution for the events with a small angle radiation ($\Delta R_{23} < 1.0$), (b) y_2 distribution for the events with a large angle radiation ($\Delta R_{23} > 1.0$), (c) y_2 distribution for soft p_T radiation case ($p_{T3}/p_{T2} < 0.3$), (d) y_2 distribution for hard p_T radiation case ($p_{T3}/p_{T2} > 0.6$).

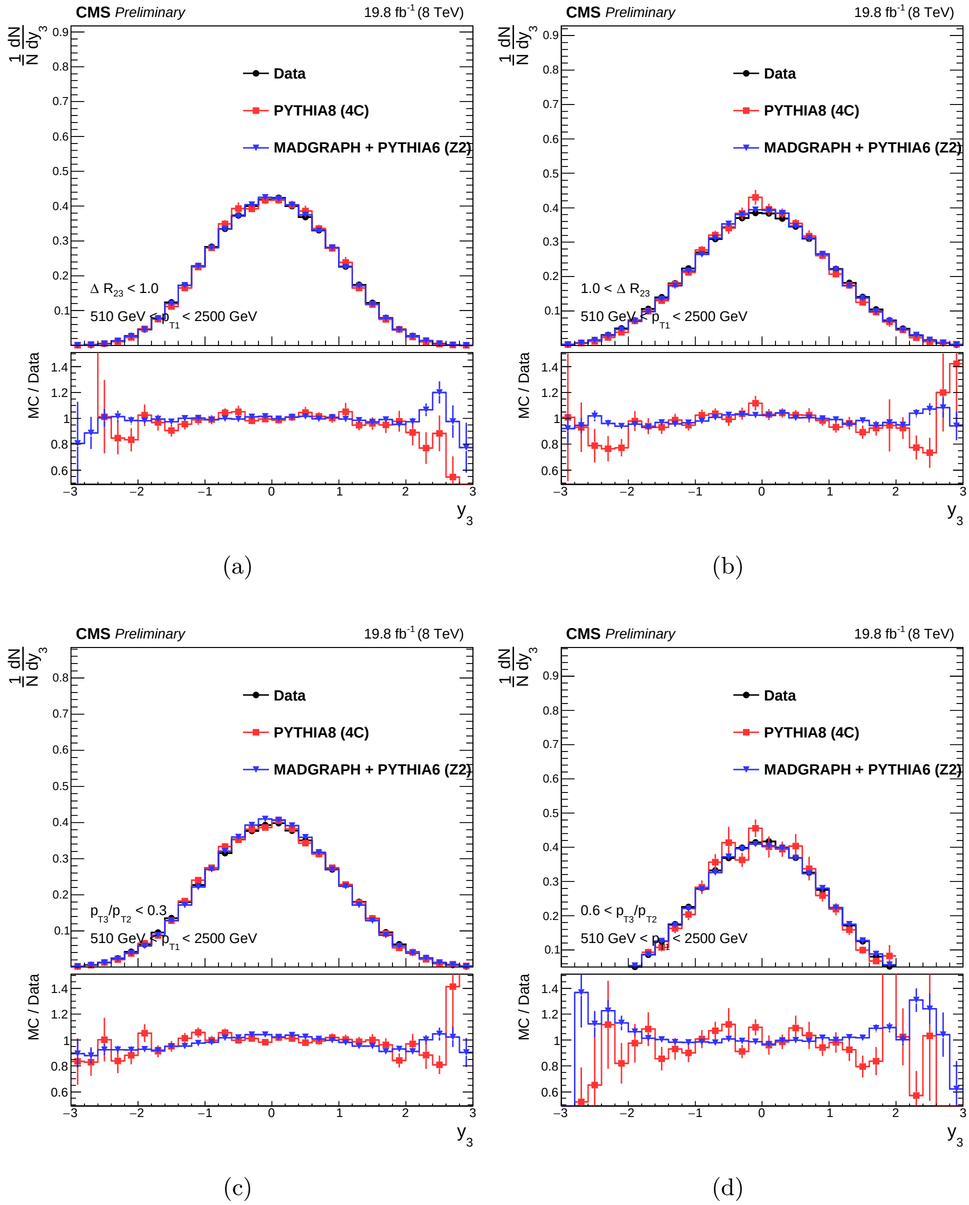

Figure 5.6: $\sqrt{s} = 8$ TeV data and theoretical predictions comparisons. (a) y_3 distribution for the events with a small angle radiation ($\Delta R_{23} < 1.0$), (b) y_3 distribution for the events with a large angle radiation ($\Delta R_{23} > 1.0$), (c) y_3 distribution for soft p_{T} radiation case ($p_{\mathrm{T}3}/p_{\mathrm{T}2} < 0.3$), (d) y_3 distribution for hard p_{T} radiation case ($p_{\mathrm{T}3}/p_{\mathrm{T}2} > 0.6$).

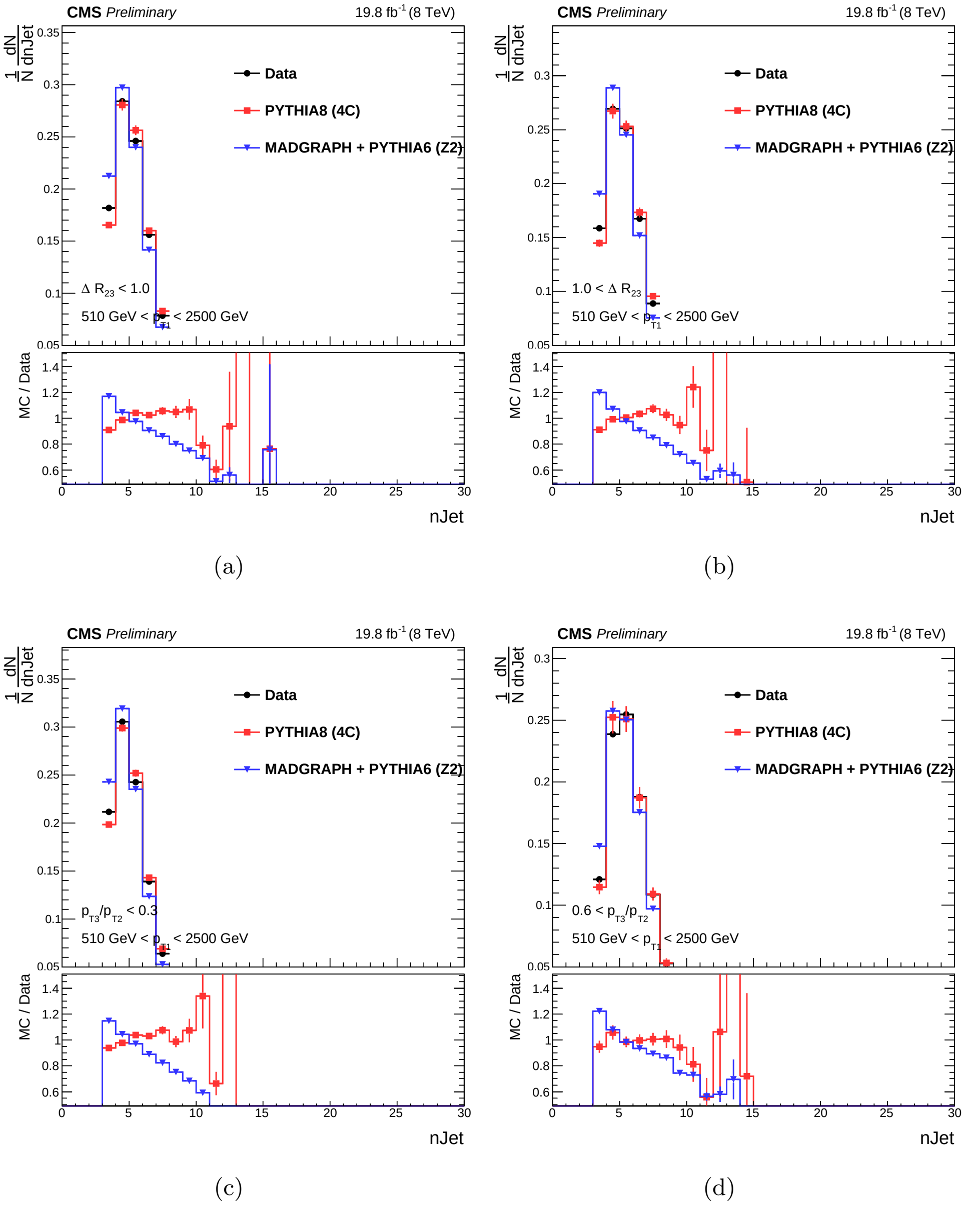

Figure 5.7: $\sqrt{s} = 8$ TeV data and theoretical predictions comparisons. (a) Number of jet distribution for the events with a small angle radiation ($\Delta R_{23} < 1.0$), (b) Number of jet distribution for the events with a large angle radiation ($\Delta R_{23} > 1.0$), (c) Number of jet distribution for soft p_{T} radiation case ($p_{\mathrm{T3}}/p_{\mathrm{T2}} < 0.3$), (d) Number of jet distribution for hard p_{T} radiation case ($p_{\mathrm{T3}}/p_{\mathrm{T2}} > 0.6$).

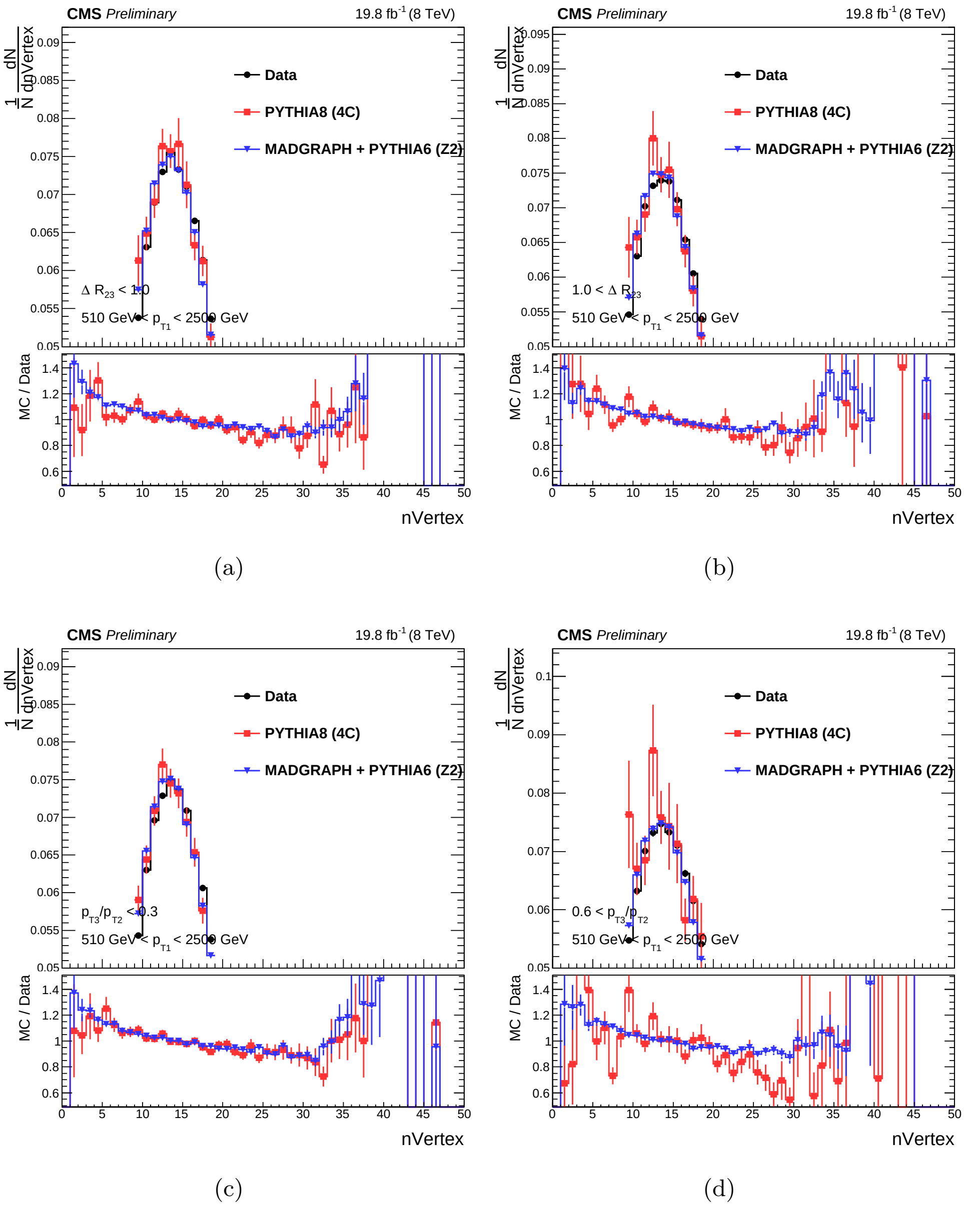

Figure 5.8: $\sqrt{s} = 8$ TeV data and theoretical predictions comparisons. (a) Number of vertex distribution for the events with a small angle radiation ($\Delta R_{23} < 1.0$), (b) Number of vertex distribution for the events with a large angle radiation ($\Delta R_{23} > 1.0$), (c) Number of vertex distribution for soft p_{T} radiation case ($p_{\mathrm{T3}}/p_{\mathrm{T2}} < 0.3$), (d) Number of vertex distribution for hard p_{T} radiation case ($p_{\mathrm{T3}}/p_{\mathrm{T2}} > 0.6$).

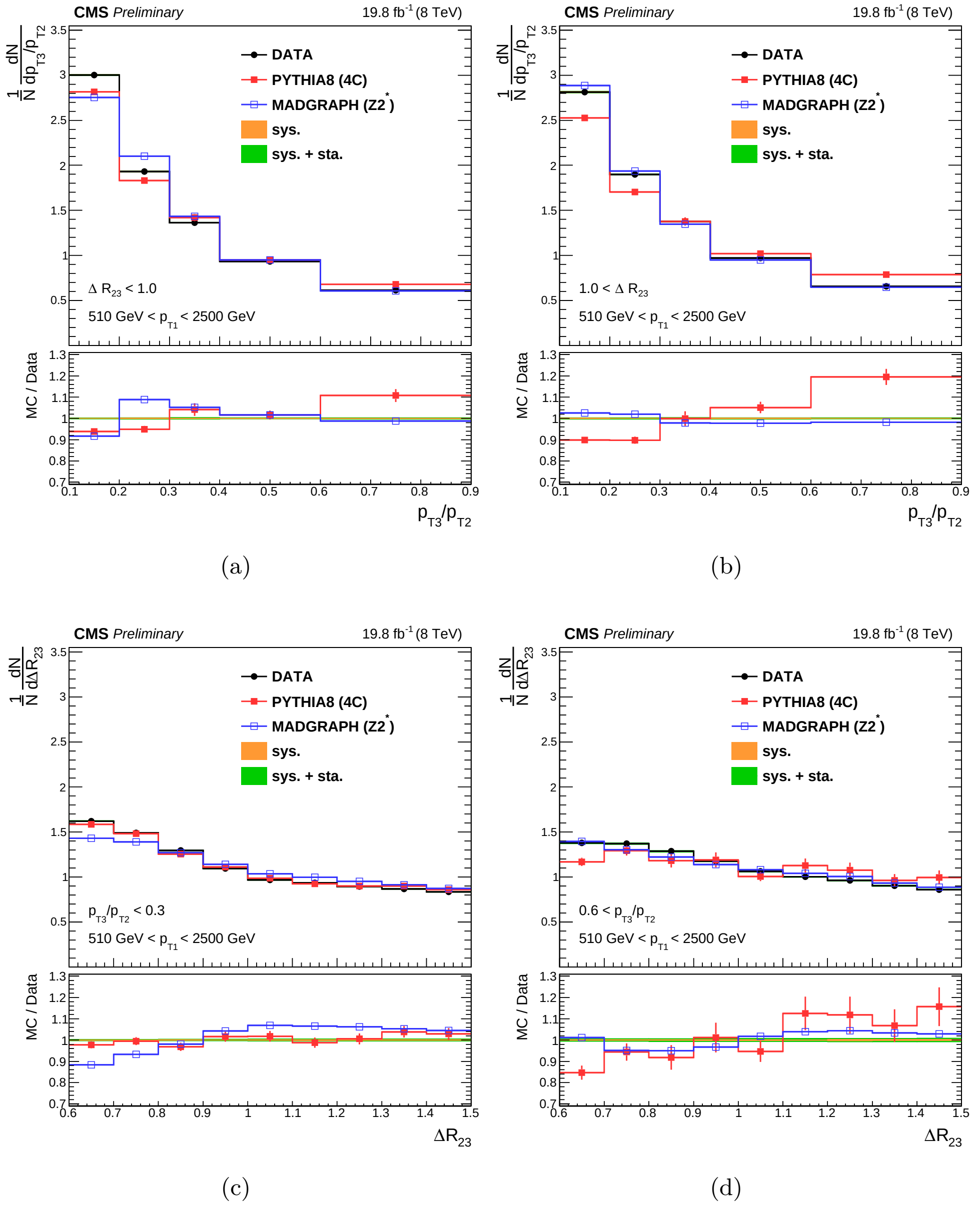

Figure 5.9: $\sqrt{s} = 8$ TeV data and theoretical predictions comparisons. (a) p_{T3}/p_{T2} distribution for the events with a small angle radiation ($\Delta R_{23} < 1.0$), (b) p_{T3}/p_{T2} distribution for the events with a large angle radiation ($\Delta R_{23} > 1.0$), (c) ΔR_{23} distribution for soft p_T radiation case ($p_{T3}/p_{T2} < 0.3$), (d) ΔR_{23} distribution for hard p_T radiation case ($p_{T3}/p_{T2} > 0.6$).

Table 5.1: $\sqrt{s} = 8$ TeV detector level systematic uncertainties

	p_{T3}/p_{T2} distribution				ΔR_{23} distribution			
	$\Delta R_{23} < 1.0$		$1.0 < \Delta R_{23}$		$p_{T3}/p_{T2} < 0.3$		$0.6 < p_{T3}/p_{T2}$	
Uncertainty	range	average	range	average	range	average	range	average
JES	0.04 - 0.09 %	0.06 %	0.03 - 0.13 %	0.08 %	0.02 - 0.20 %	0.10 %	0.09 - 0.27 %	0.19 %
JER	0.10 - 0.23 %	0.16 %	0.04 - 0.22 %	0.15 %	0.04 - 0.21 %	0.11 %	0.01 - 0.33 %	0.13 %
PU	0.01 - 0.11 %	0.04 %	0.00 - 0.07 %	0.03 %	0.01 - 0.19 %	0.10 %	0.04 - 0.23 %	0.12 %
SYS	0.14 - 0.24 %	0.18 %	0.12 - 0.26 %	0.18 %	0.09 - 0.30 %	0.20 %	0.20 - 0.38 %	0.28 %
STA	0.27 - 0.39 %	0.33 %	0.29 - 0.42 %	0.36 %	0.38 - 0.53 %	0.47 %	0.66 - 0.83 %	0.74 %
Sys. + Sta.	0.30 - 0.44 %	0.38 %	0.37 - 0.47 %	0.40 %	0.41 - 0.58 %	0.51 %	0.69 - 0.89 %	0.79 %

The PS method to calculate MC uses PYTHIA 8 with tune 4C and the ME method to calculate MC uses MadGraph with PYTHIA 6 tune Z2star. Figures 5.9 show the detector level comparison. In the PS dominant regions, the PYTHIA 8 PS method calculation describes better the data when compared to the MadGraph ME method calculation. In the ME dominant regions, MadGraph performance became better than PYTHIA 8.

5.1.2 $\sqrt{s} = 13$ TeV

This section shows the $\sqrt{s} = 13\,\text{TeV}$ data detector level comparison. The detector level systematic uncertainties are calculated with JES, JER, and PU. The data is compared with two MC predictions using the PS and the ME method. The PS method calculation MC is PYTHIA 8 with tune CUETP8M1 and the ME method calculation MC is MadGraph with PYTHIA 8 tune CUETP8M1.

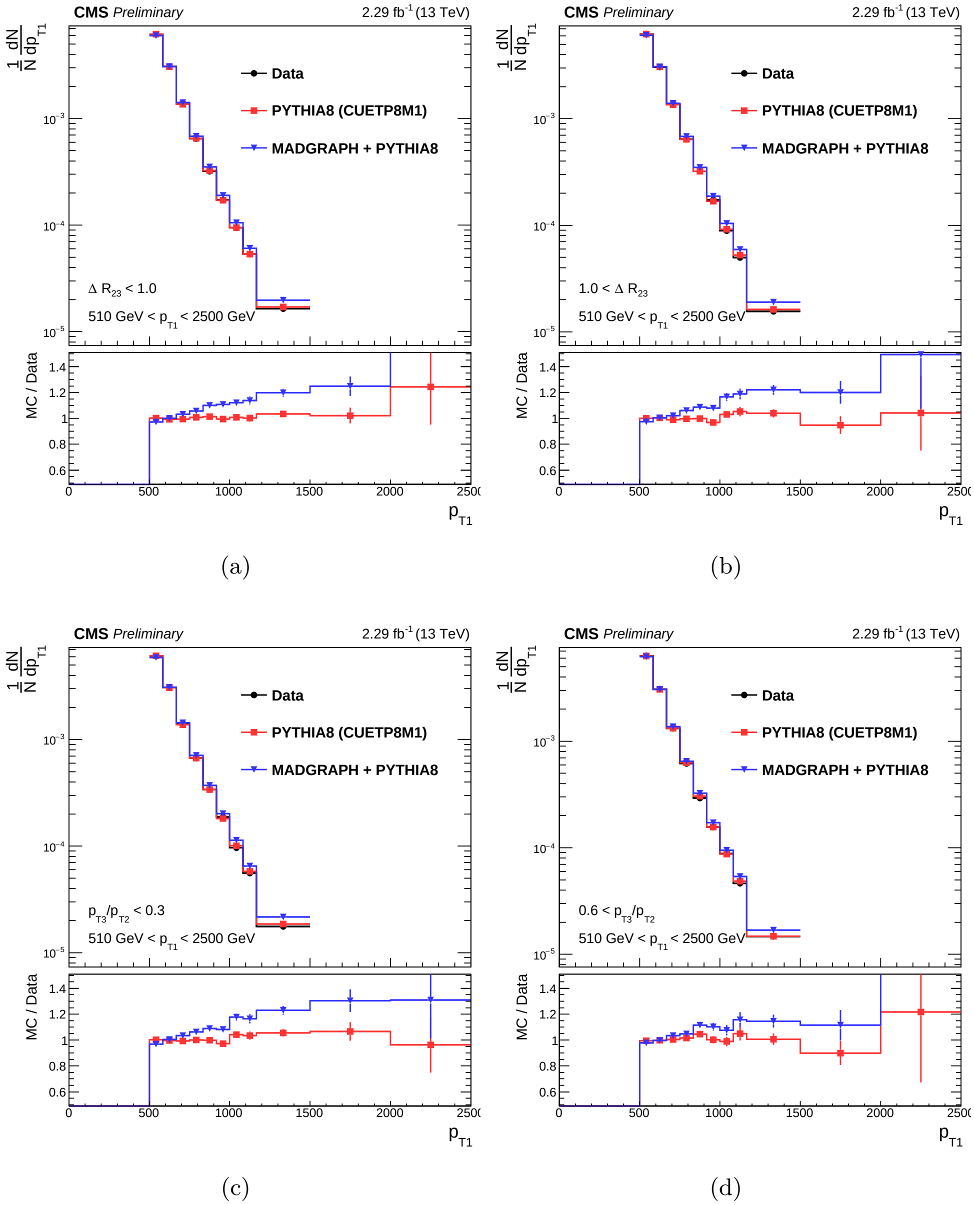

Figure 5.10: $\sqrt{s} = 13$ TeV data and theoretical predictions comparisons. (a) $p_{\mathrm{T}1}$ distribution for the events with a small angle radiation ($\Delta R_{23} < 1.0$), (b) $p_{\mathrm{T}1}$ distribution for the events with a large angle radiation ($\Delta R_{23} > 1.0$), (c) $p_{\mathrm{T}1}$ distribution for soft p_{T} radiation case ($p_{\mathrm{T}3}/p_{\mathrm{T}2} < 0.3$), (d) $p_{\mathrm{T}1}$ distribution for hard p_{T} radiation case ($p_{\mathrm{T}3}/p_{\mathrm{T}2} > 0.6$).

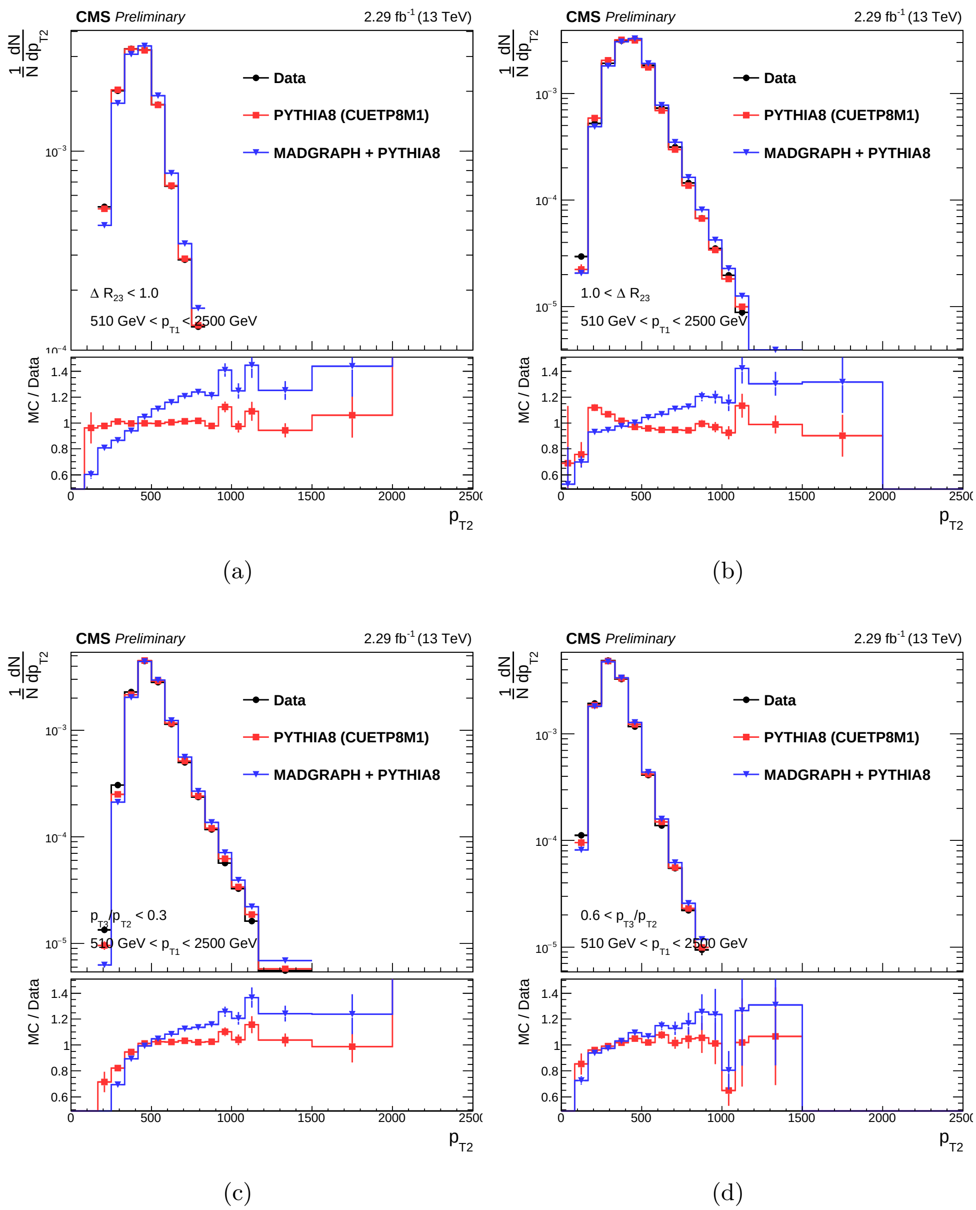

(a) (b) (c) (d)

Figure 5.11: $\sqrt{s} = 13$ TeV data and theoretical predictions comparisons. (a) p_{T2} distribution for the events with a small angle radiation ($\Delta R_{23} < 1.0$), (b) p_{T2} distribution for the events with a large angle radiation ($\Delta R_{23} > 1.0$), (c) p_{T2} distribution for soft p_{T} radiation case ($p_{\mathrm{T3}}/p_{\mathrm{T2}} < 0.3$), (d) p_{T2} distribution for hard p_{T} radiation case ($p_{\mathrm{T3}}/p_{\mathrm{T2}} > 0.6$).

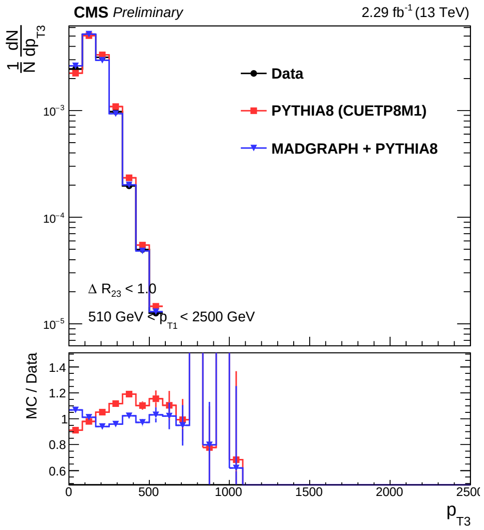

(a)

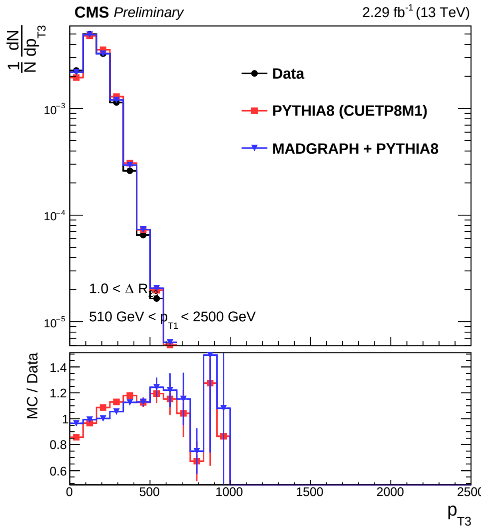

(b)

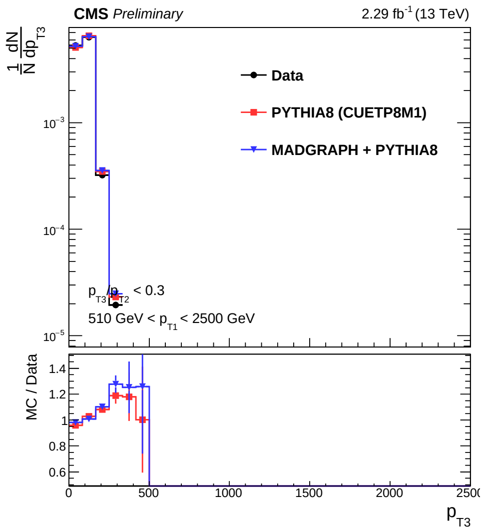

(c)

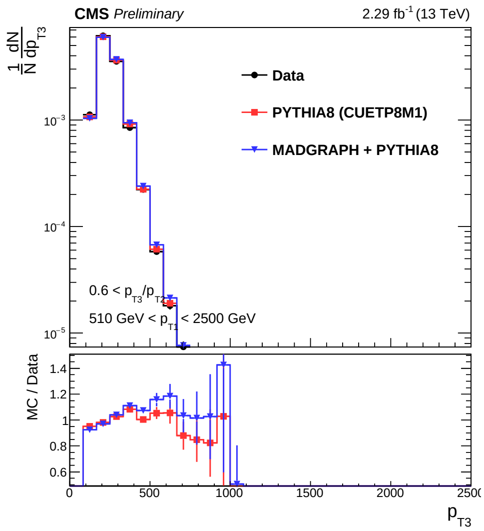

(d)

Figure 5.12: $\sqrt{s} = 13$ TeV data and theoretical predictions comparisons. (a) p_{T3} distribution for the events with a small angle radiation ($\Delta R_{23} < 1.0$), (b) p_{T3} distribution for the events with a large angle radiation ($\Delta R_{23} > 1.0$), (c) p_{T3} distribution for soft p_{T} radiation case ($p_{\mathrm{T3}}/p_{\mathrm{T2}} < 0.3$), (d) p_{T3} distribution for hard p_{T} radiation case ($p_{\mathrm{T3}}/p_{\mathrm{T2}} > 0.6$).

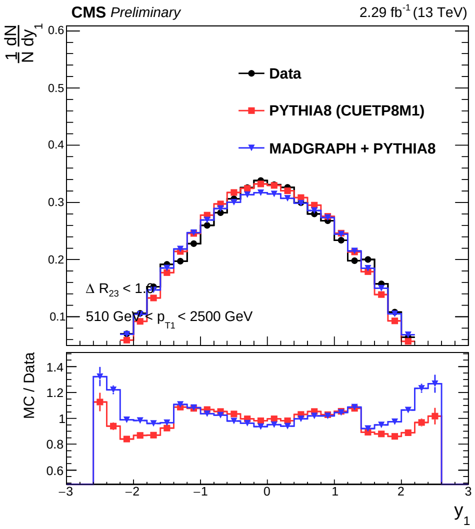

(a)

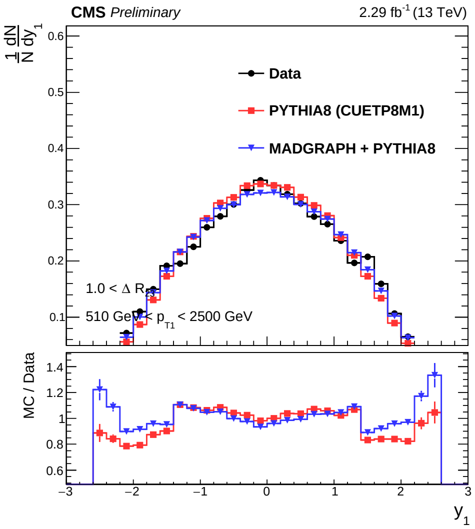

(b)

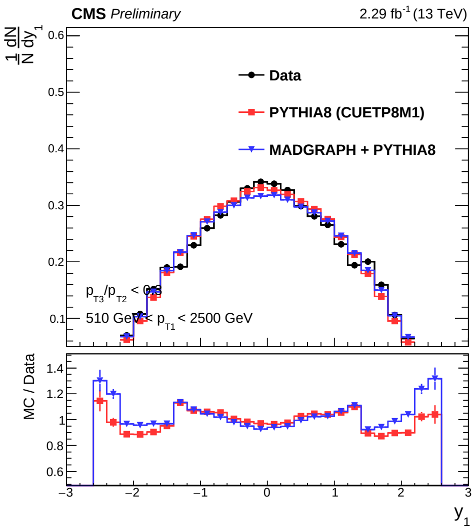

(c)

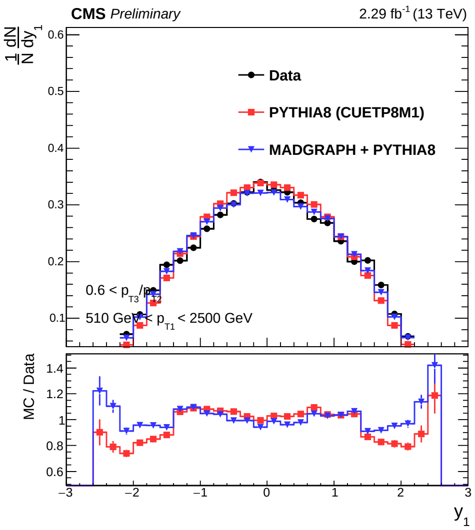

(d)

Figure 5.13: $\sqrt{s} = 13$ TeV data and theoretical predictions comparisons. (a) y_1 distribution for the events with a small angle radiation ($\Delta R_{23} < 1.0$), (b) y_1 distribution for the events with a large angle radiation ($\Delta R_{23} > 1.0$), (c) y_1 distribution for soft p_{T} radiation case ($p_{\mathrm{T3}}/p_{\mathrm{T2}} < 0.3$), (d) y_1 distribution for hard p_{T} radiation case ($p_{\mathrm{T3}}/p_{\mathrm{T2}} > 0.6$).

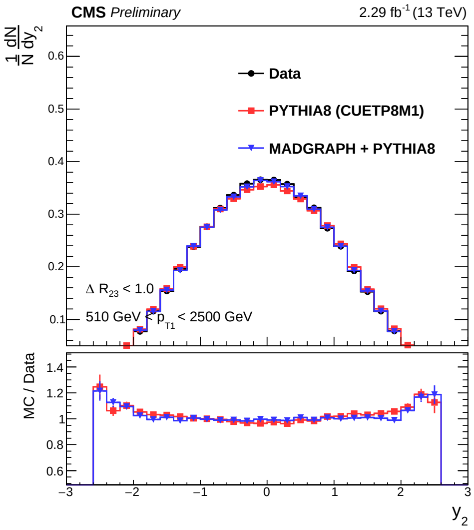

(a)

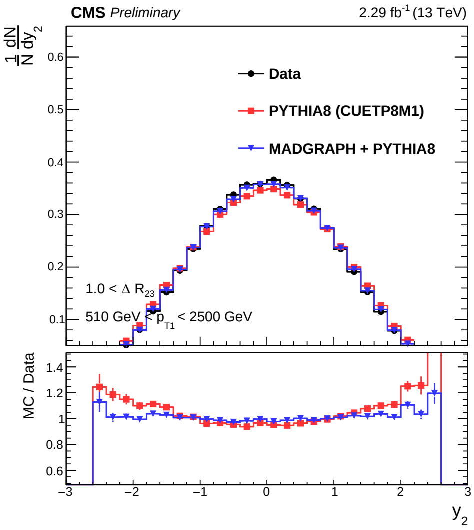

(b)

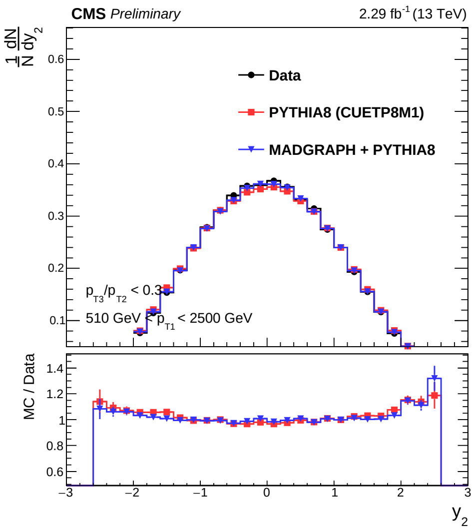

(c)

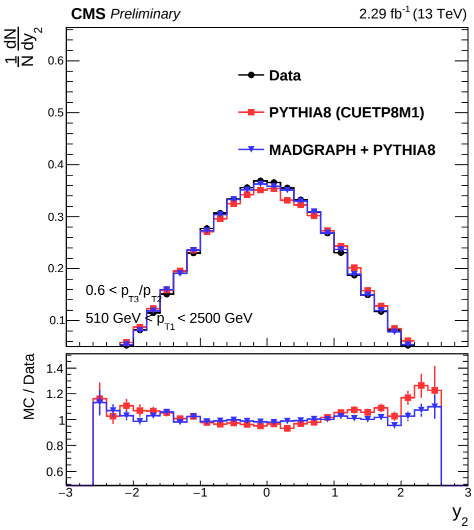

(d)

Figure 5.14: $\sqrt{s} = 13$ TeV data and theoretical predictions comparisons. (a) y_2 distribution for the events with a small angle radiation ($\Delta R_{23} < 1.0$), (b) y_2 distribution for the events with a large angle radiation ($\Delta R_{23} > 1.0$), (c) y_2 distribution for soft p_{T} radiation case ($p_{\mathrm{T3}}/p_{\mathrm{T2}} < 0.3$), (d) y_2 distribution for hard p_{T} radiation case ($p_{\mathrm{T3}}/p_{\mathrm{T2}} > 0.6$).

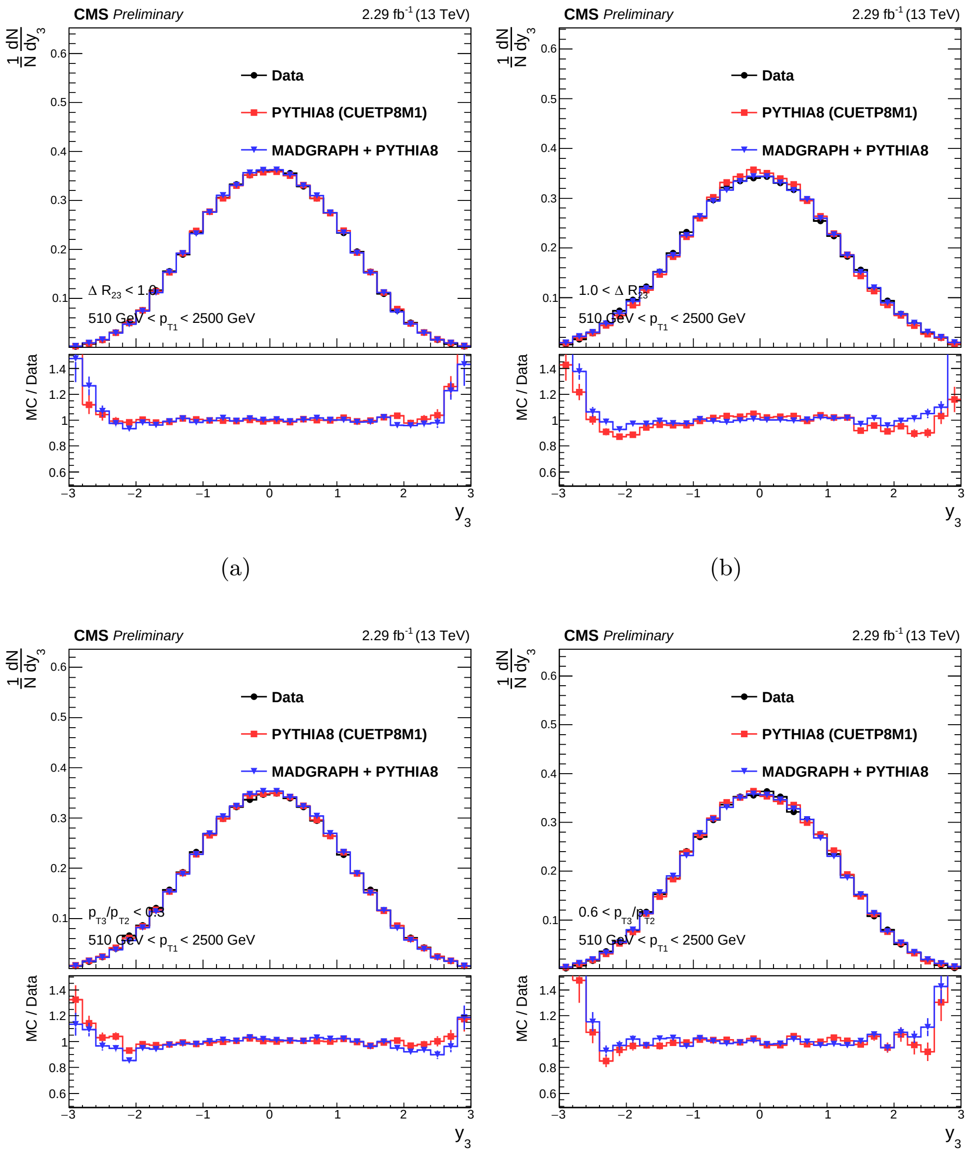

(c) (d)

Figure 5.15: $\sqrt{s} = 13$ TeV data and theoretical predictions comparisons. (a) y_3 distribution for the events with a small angle radiation ($\Delta R_{23} < 1.0$), (b) y_3 distribution for the events with a large angle radiation ($\Delta R_{23} > 1.0$), (c) y_3 distribution for soft p_{T} radiation case ($p_{\mathrm{T3}}/p_{\mathrm{T2}} < 0.3$), (d) y_3 distribution for hard p_{T} radiation case ($p_{\mathrm{T3}}/p_{\mathrm{T2}} > 0.6$).

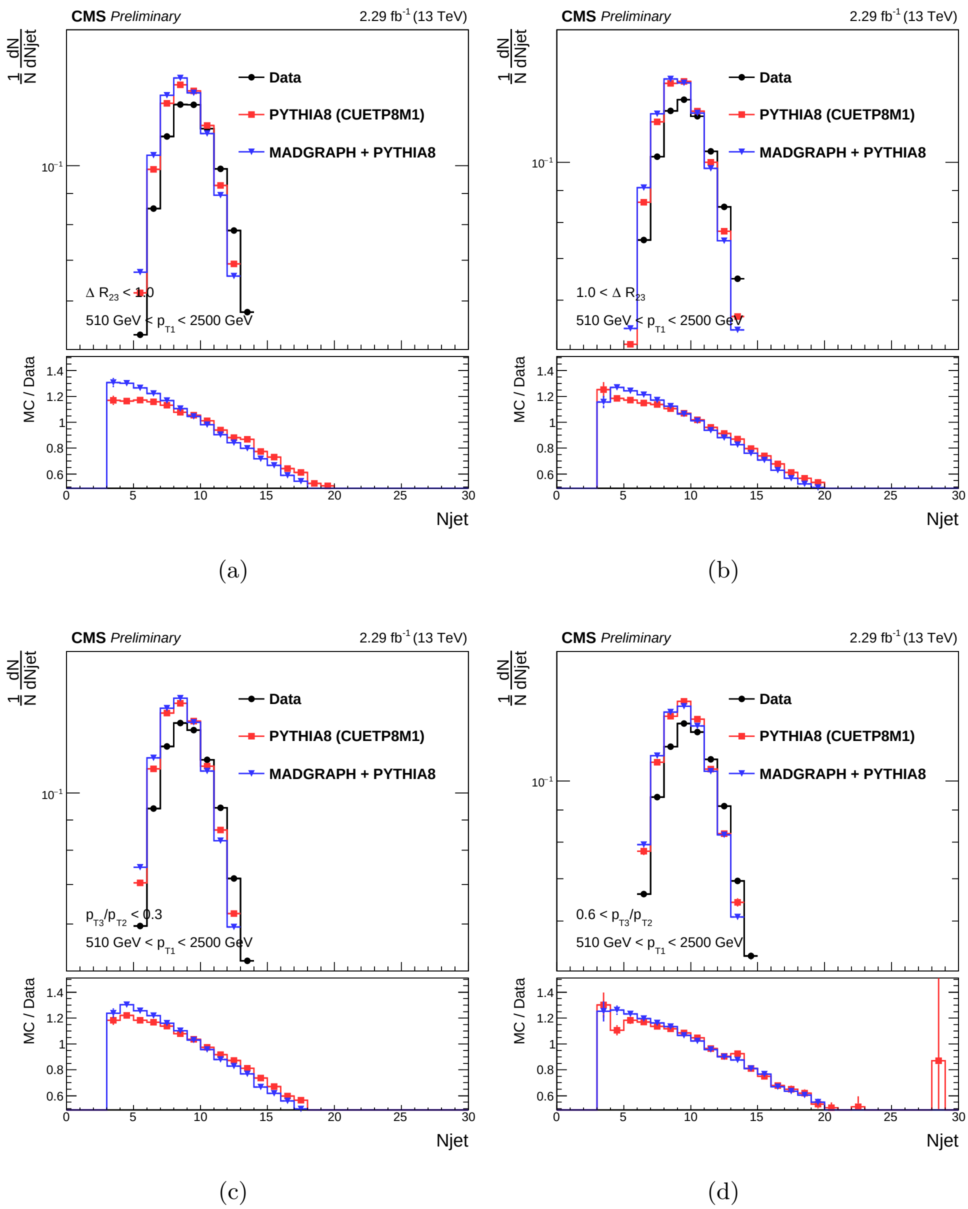

Figure 5.16: $\sqrt{s}$ = 13 TeV data and theoretical predictions comparisons. (a) Number of jet distribution for the events with a small angle radiation ($\Delta R_{23} < 1.0$), (b) Number of jet distribution for the events with a large angle radiation ($\Delta R_{23} > 1.0$), (c) Number of jet distribution for soft p_{T} radiation case ($p_{\mathrm{T3}}/p_{\mathrm{T2}} < 0.3$), (d) Number of jet distribution for hard p_{T} radiation case ($p_{\mathrm{T3}}/p_{\mathrm{T2}} > 0.6$).

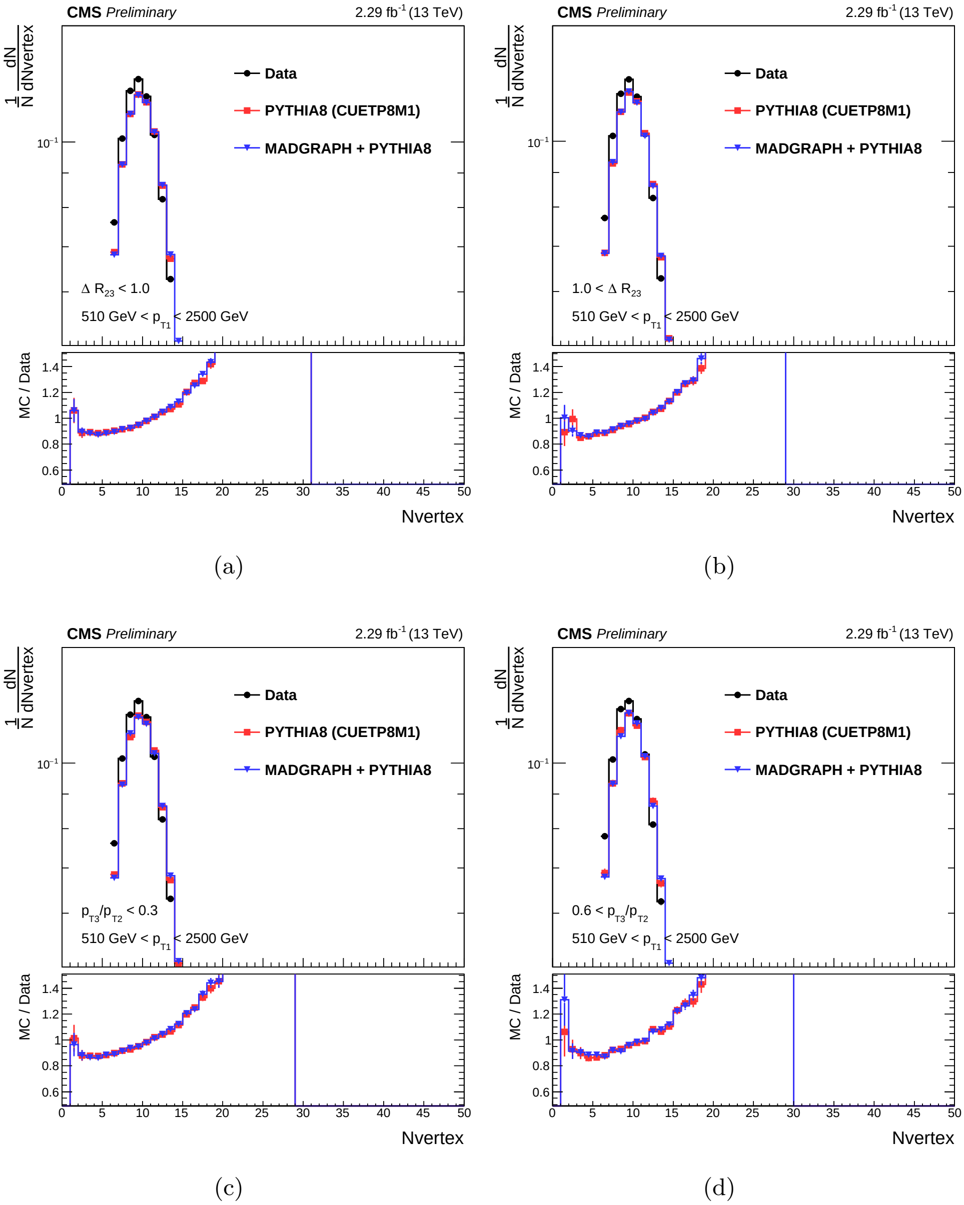

(a) (b) (c) (d)

Figure 5.17: $\sqrt{s} = 13$ TeV data and theoretical predictions comparisons. (a) Number of vertex distribution for the events with a small angle radiation ($\Delta R_{23} < 1.0$), (b) Number of vertex distribution for the events with a large angle radiation ($\Delta R_{23} > 1.0$), (c) Number of vertex distribution for soft p_{T} radiation case ($p_{\mathrm{T3}}/p_{\mathrm{T2}} < 0.3$), (d) Number of vertex distribution for hard p_{T} radiation case ($p_{\mathrm{T3}}/p_{\mathrm{T2}} > 0.6$).

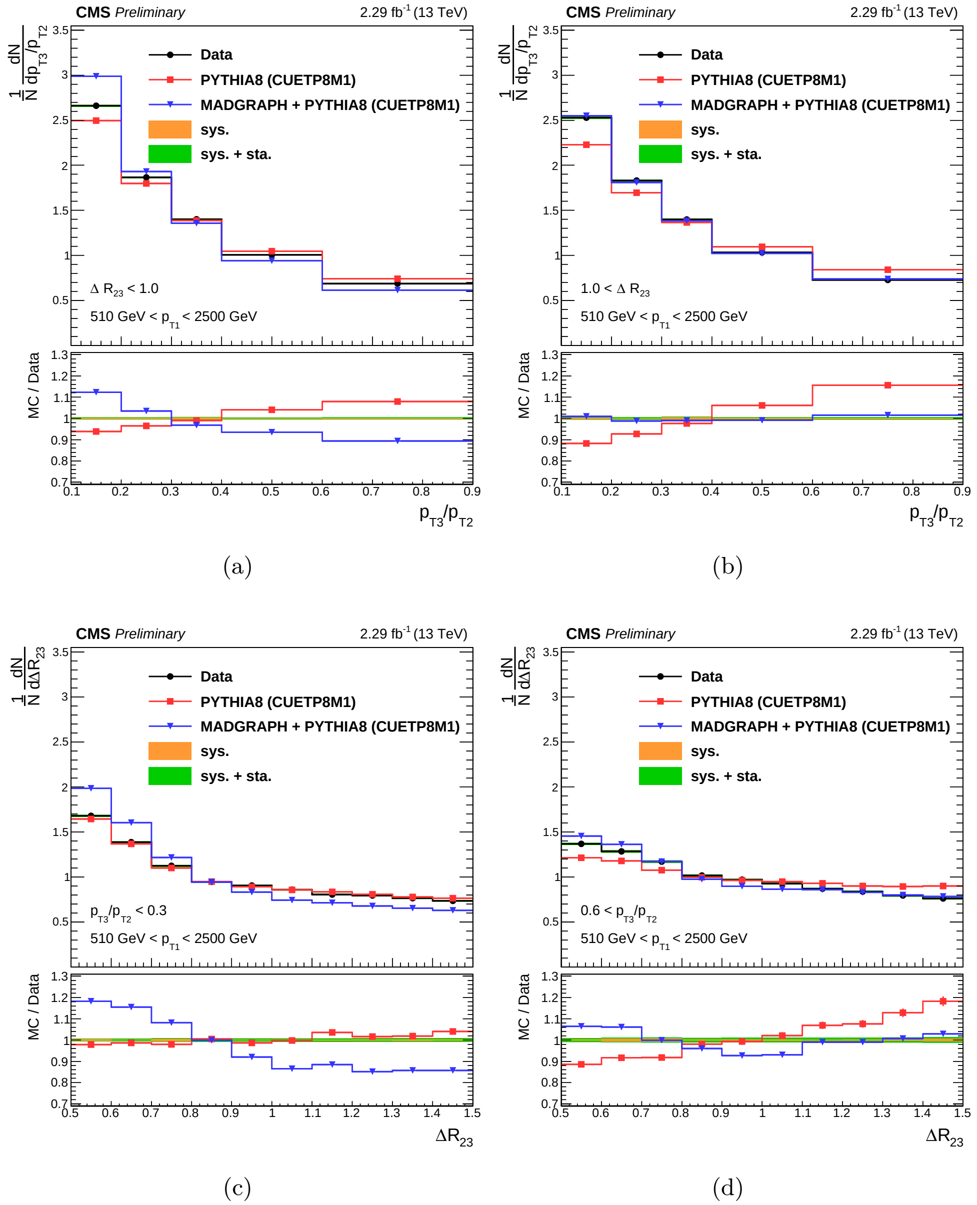

Figure 5.18: $\sqrt{s} = 13$ TeV data and theoretical predictions comparisons. (a) $p_{\mathrm{T3}}/p_{\mathrm{T2}}$ distribution for the events with a small angle radiation ($\Delta R_{23} < 1.0$), (b) $p_{\mathrm{T3}}/p_{\mathrm{T2}}$ distribution for the events with a large angle radiation ($\Delta R_{23} > 1.0$), (c) ΔR_{23} distribution for soft p_{T} radiation case ($p_{\mathrm{T3}}/p_{\mathrm{T2}} < 0.3$), (d) ΔR_{23} distribution for hard p_{T} radiation case ($p_{\mathrm{T3}}/p_{\mathrm{T2}} > 0.6$).

Table 5.2: $\sqrt{s} = 13\,\text{TeV}$ detector level systematic uncertainties

	p_{T3}/p_{T2} distribution				ΔR_{23} distribution			
	$\Delta R_{23} < 1.0$		$1.0 < \Delta R_{23}$		$p_{T3}/p_{T2} < 0.3$		$0.6 < p_{T3}/p_{T2}$	
Uncertainty	range	average	range	average	range	average	range	average
JES	0.08 - 0.28 %	0.18 %	0.11 - 0.36 %	0.17 %	0.02 - 0.34 %	0.16 %	0.13 - 0.42 %	0.24 %
JER	0.04 - 0.15 %	0.11 %	0.04 - 0.25 %	0.14 %	0.01 - 0.16 %	0.08 %	0.06 - 0.17 %	0.11 %
PU	0.00 - 0.10 %	0.04 %	0.01 - 0.24 %	0.08 %	0.03 - 0.51 %	0.14 %	0.06 - 0.56 %	0.22 %
SYS	0.13 - 0.32 %	0.22 %	0.14 - 0.45 %	0.25 %	0.13 - 0.51 %	0.27 %	0.16 - 0.70 %	0.36 %
STA	0.35 - 0.49 %	0.41 %	0.44 - 0.59 %	0.50 %	0.51 - 0.78 %	0.68 %	0.83 - 1.11 %	0.98 %
Sys. + Sta.	0.43 - 0.58 %	0.47 %	0.50 - 0.74 %	0.57 %	0.58 - 0.81 %	0.74 %	0.86 - 1.24 %	1.06 %

5.2 Unfolding

To compare the results with the theory and the corresponding results from other experiments the unfolding process of the data for the detector effects needs to be employed. Since the physics models implemented in the event generators and the detector simulations never work perfectly, the remaining effects should be considered as systematic uncertainties. In this analysis, the MadGraph full CMS detector simulation was used for the unfolding. The D'Agostini Bayesian methods in the Roounfold software package was used for the unfolding [41].

5.2.1 Response matrix

The CMS full detector simulation MC builds the response matrix. This response matrix shows detector migration effects between the generator (gen) jet and the JER reconstruction (reco) jet. For describing the jet energy resolution of data, the JER correction adds p_{T} correction to reco jet. The gen jets are matched to reco jet with diameter R which is 0.1 smaller than the clustering diameter. The AK4 jet using the matching R = 0.3 and the AK5 jet using the matching R = 0.4. The response matrix is drawn (Figure 5.19-5.20) normalized by the total entities of the gen bins. It makes the clear understanding of how the gen distribution migrates to the reco distribution. The response matrices are built with MADGRAPH MC set.

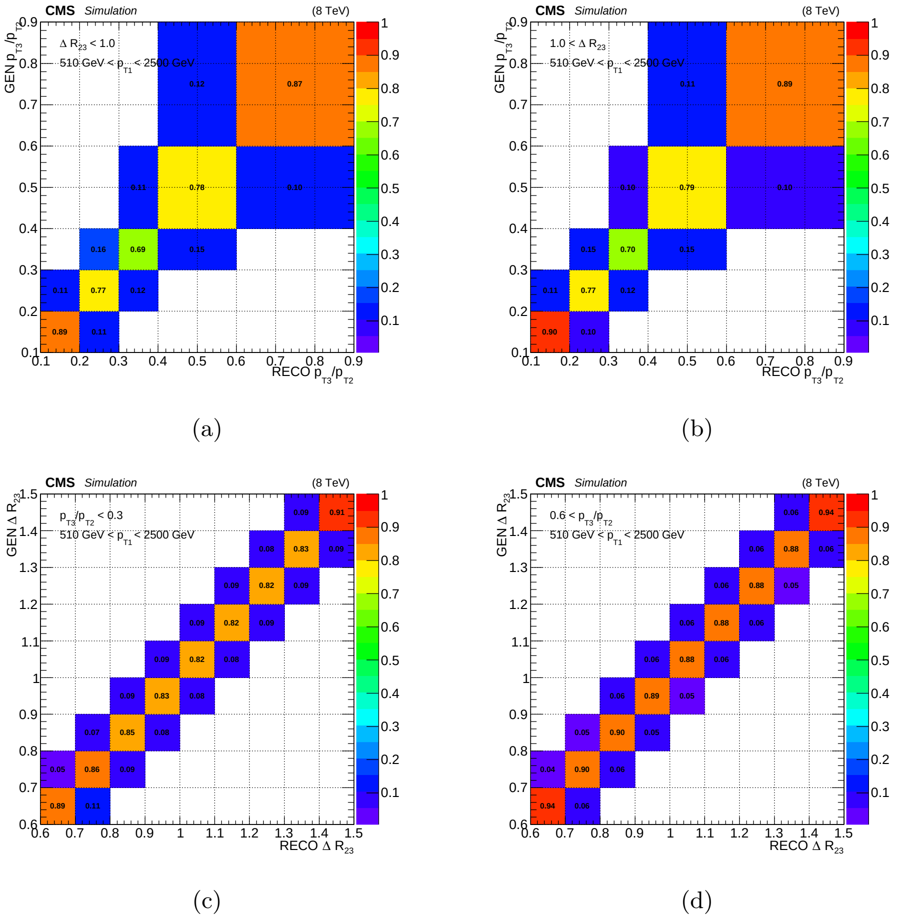

Figure 5.19: $\sqrt{s}$ = 8 TeV response matrices. (a) $p_{\mathrm{T3}}/p_{\mathrm{T2}}$ distribution response matrix for the events with a small angle radiation ($\Delta R_{23} < 1.0$), (b) $p_{\mathrm{T3}}/p_{\mathrm{T2}}$ distribution response matrix for the events with a large angle radiation ($\Delta R_{23} > 1.0$), (c) ΔR_{23} distribution response matrix for soft p_{T} radiation case ($p_{\mathrm{T3}}/p_{\mathrm{T2}} < 0.3$), (d) ΔR_{23} distribution response matrix for hard p_{T} radiation case ($p_{\mathrm{T3}}/p_{\mathrm{T2}} > 0.6$).

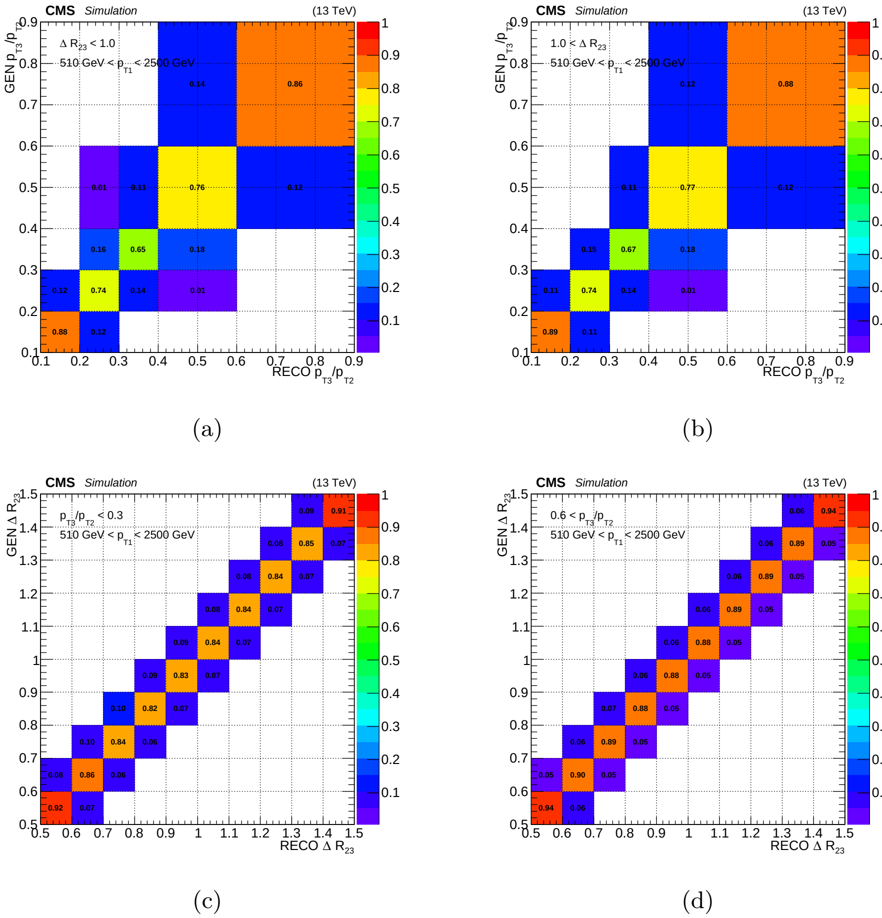

Figure 5.20: $\sqrt{s} = 13$ TeV response matrices. (a) p_{T3}/p_{T2} distribution response matrix for the events with a small angle radiation ($\Delta R_{23} < 1.0$), (b) p_{T3}/p_{T2} distribution response matrix for the events with a large angle radiation ($\Delta R_{23} > 1.0$), (c) ΔR_{23} distribution response matrix for soft p_T radiation case ($p_{T3}/p_{T2} < 0.3$), (d) ΔR_{23} distribution response matrix for hard p_T radiation case ($p_{T3}/p_{T2} > 0.6$).

5.2.2 Purity, stability, acceptance, and background

The measurement at detector (reco) and generator (gen) level stays in the same bin or different bins at the two levels. The migration effects, the measurement at detector and generator levels does not stay in the same bin. There are two types of migration effects. The first case is both level events were selected, but they are not in the same bin. The second case is only one level event was selected. The consideration of the first case, purity, and stability are studied. For the second case, acceptance and background are considered.

- The purity represents the percentage of events in a certain bin i at the detector level *det*, which are also selected at the generator level *gen* and belong to the same bin (equation 5.1). Figures 5.21-5.22 show the purity distribution.

$$P_i^{MC} = \frac{N^{MC}_{both\,select}(E^{MC}_{det} \in bin\; i \wedge E^{MC}_{gen} \in bin\; i)}{N^{MC}_{both\,select}(E^{MC}_{det} \in bin\; i)} \tag{5.1}$$

- The stability quantifies the percentage of events in a certain bin i at the generator level *gen*, which are also selected at the detector level *det* and belong to the same bin (equation 5.2). The figures 5.23-5.24 show the stability distribution.

$$S_i^{MC} = \frac{N^{MC}_{both\,select}(E^{MC}_{det} \in bin\; i \wedge E^{MC}_{gen} \in bin\; i)}{N^{MC}_{both\,select}(E^{MC}_{gen} \in bin\; i)} \tag{5.2}$$

- The acceptance measures the percentage of events in a certain bin i at the generator level *gen*, which are also selected at the detector level *det* and belong to the same bin (equation 5.3). The figures 5.25-5.26 show the acceptance distribution.

$$A_i^{MC} = \frac{N_{both\,select}^{MC}(E_{gen}^{MC} \in bin\ i)}{N_{select}^{MC}(E_{gen}^{MC} \in bin\ i)} \tag{5.3}$$

- The background measures the percentage of events in a certain bin i at the detector level *det*, which are also selected at the generator level *gen* and belong to the same bin (equation 5.4). The figures 5.27-5.28 show the background distribution.

$$B_i^{MC} = 1 - \frac{N_{both\,select}^{MC}(E_{det}^{MC} \in bin\ i)}{N_{select}^{MC}(E_{det}^{MC} \in bin\ i)} \tag{5.4}$$

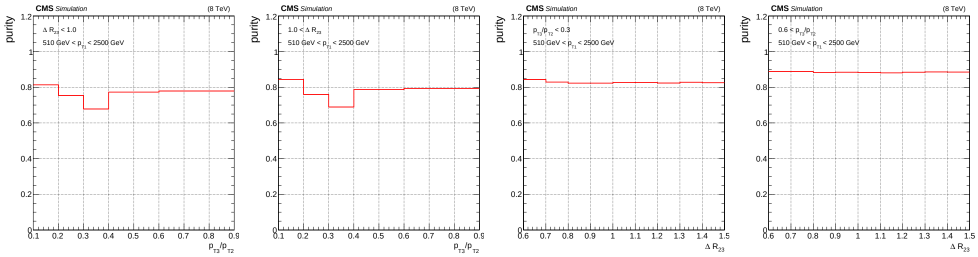

(a) (b) (c) (d)

Figure 5.21: $\sqrt{s} = 8$ TeV the purity. (a) $p_{\mathrm{T}3}/p_{\mathrm{T}2}$ distribution purity for the events with a small angle radiation ($\Delta R_{23} < 1.0$), (b) $p_{\mathrm{T}3}/p_{\mathrm{T}2}$ distribution purity for the events with a large angle radiation ($\Delta R_{23} > 1.0$), (c) ΔR_{23} distribution purity for soft p_{T} radiation case ($p_{\mathrm{T}3}/p_{\mathrm{T}2} < 0.3$), (d) ΔR_{23} distribution purity for hard p_{T} radiation case ($p_{\mathrm{T}3}/p_{\mathrm{T}2} > 0.6$).

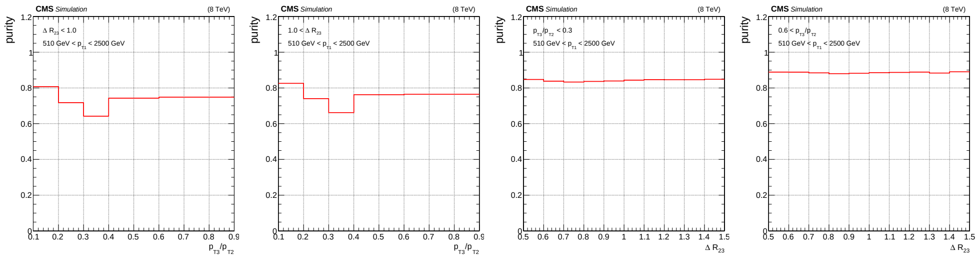

(a) (b) (c) (d)

Figure 5.22: $\sqrt{s} = 13$ TeV the purity. (a) $p_{\mathrm{T}3}/p_{\mathrm{T}2}$ distribution purity for the events with a small angle radiation ($\Delta R_{23} < 1.0$), (b) $p_{\mathrm{T}3}/p_{\mathrm{T}2}$ distribution purity for the events with a large angle radiation ($\Delta R_{23} > 1.0$), (c) ΔR_{23} distribution purity for soft p_{T} radiation case ($p_{\mathrm{T}3}/p_{\mathrm{T}2} < 0.3$), (d) ΔR_{23} distribution purity for hard p_{T} radiation case ($p_{\mathrm{T}3}/p_{\mathrm{T}2} > 0.6$).

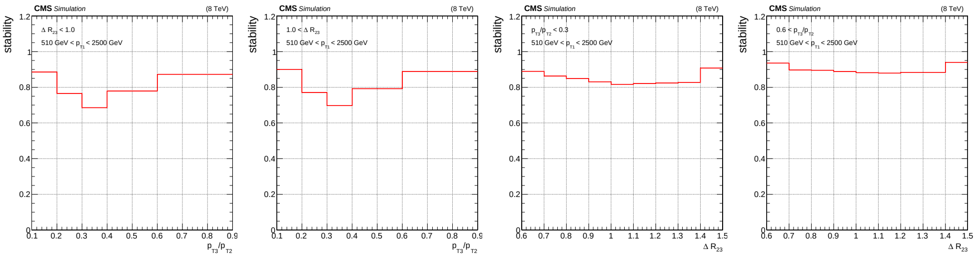

(a) (b) (c) (d)

Figure 5.23: $\sqrt{s}$ = 8 TeV the stability. (a) p_{T3}/p_{T2} distribution stability for the events with a small angle radiation ($\Delta R_{23} < 1.0$), (b) p_{T3}/p_{T2} distribution stability for the events with a large angle radiation ($\Delta R_{23} > 1.0$), (c) ΔR_{23} distribution stability for soft p_T radiation case ($p_{T3}/p_{T2} < 0.3$), (d) ΔR_{23} distribution stability for hard p_T radiation case ($p_{T3}/p_{T2} > 0.6$).

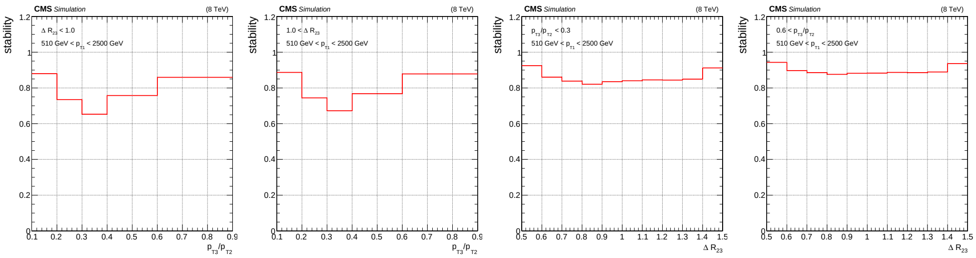

(a) (b) (c) (d)

Figure 5.24: $\sqrt{s}$ = 13 TeV the stability. (a) p_{T3}/p_{T2} distribution stability for the events with a small angle radiation ($\Delta R_{23} < 1.0$), (b) p_{T3}/p_{T2} distribution stability for the events with a large angle radiation ($\Delta R_{23} > 1.0$), (c) ΔR_{23} distribution stability for soft p_T radiation case ($p_{T3}/p_{T2} < 0.3$), (d) ΔR_{23} distribution stability for hard p_T radiation case ($p_{T3}/p_{T2} > 0.6$).

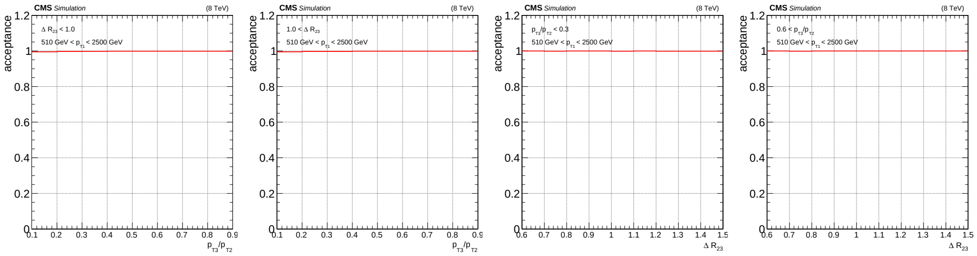

(a) (b) (c) (d)

Figure 5.25: $\sqrt{s} = 8$ TeV the acceptance. (a) p_{T3}/p_{T2} distribution acceptance for the events with a small angle radiation ($\Delta R_{23} < 1.0$), (b) p_{T3}/p_{T2} distribution acceptance for the events with a large angle radiation ($\Delta R_{23} > 1.0$), (c) ΔR_{23} distribution acceptance for soft p_T radiation case ($p_{T3}/p_{T2} < 0.3$), (d) ΔR_{23} distribution acceptance for hard p_T radiation case ($p_{T3}/p_{T2} > 0.6$).

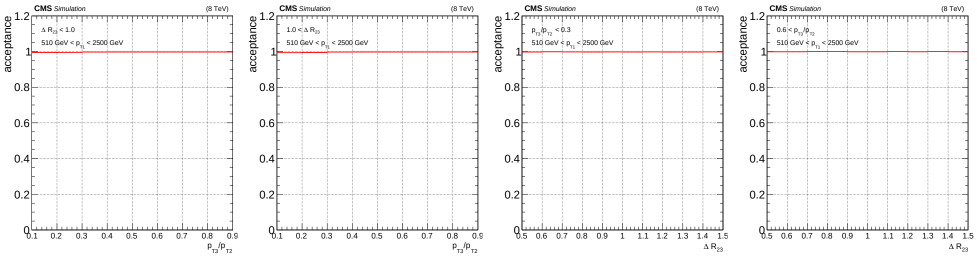

(a) (b) (c) (d)

Figure 5.26: $\sqrt{s} = 13$ TeV the acceptance. (a) p_{T3}/p_{T2} distribution acceptance for the events with a small angle radiation ($\Delta R_{23} < 1.0$), (b) p_{T3}/p_{T2} distribution acceptance for the events with a large angle radiation ($\Delta R_{23} > 1.0$), (c) ΔR_{23} distribution acceptance for soft p_T radiation case ($p_{T3}/p_{T2} < 0.3$), (d) ΔR_{23} distribution acceptance for hard p_T radiation case ($p_{T3}/p_{T2} > 0.6$).

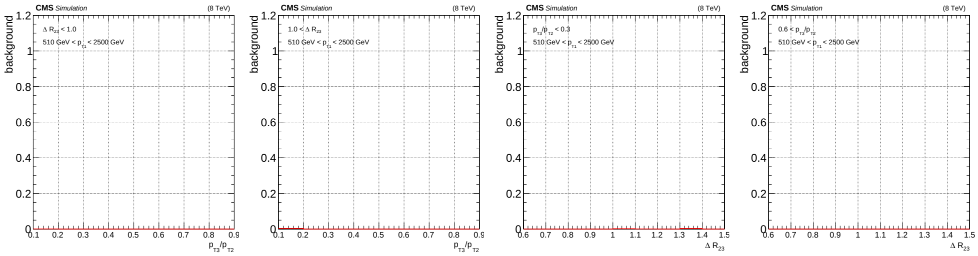

(a) (b) (c) (d)

Figure 5.27: $\sqrt{s} = 8$ TeV the background. (a) $p_{\mathrm{T3}}/p_{\mathrm{T2}}$ distribution background for the events with a small angle radiation ($\Delta R_{23} < 1.0$), (b) $p_{\mathrm{T3}}/p_{\mathrm{T2}}$ distribution background for the events with a large angle radiation ($\Delta R_{23} > 1.0$), (c) ΔR_{23} distribution background for soft p_{T} radiation case ($p_{\mathrm{T3}}/p_{\mathrm{T2}} < 0.3$), (d) ΔR_{23} distribution background for hard p_{T} radiation case ($p_{\mathrm{T3}}/p_{\mathrm{T2}} > 0.6$).

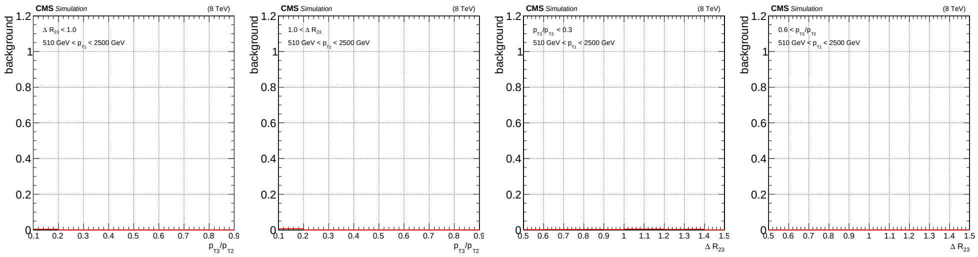

(a) (b) (c) (d)

Figure 5.28: $\sqrt{s} = 13$ TeV the background. (a) $p_{\mathrm{T3}}/p_{\mathrm{T2}}$ distribution background for the events with a small angle radiation ($\Delta R_{23} < 1.0$), (b) $p_{\mathrm{T3}}/p_{\mathrm{T2}}$ distribution background for the events with a large angle radiation ($\Delta R_{23} > 1.0$), (c) ΔR_{23} distribution background for soft p_{T} radiation case ($p_{\mathrm{T3}}/p_{\mathrm{T2}} < 0.3$), (d) ΔR_{23} distribution background for hard p_{T} radiation case ($p_{\mathrm{T3}}/p_{\mathrm{T2}} > 0.6$).

5.2.3 Iteration test

The D'Agostini Bayesian method is required for the iteration study. The iteration study is considered to show the stability of the unfolding results. After 7 iterations, the unfolding results became stable. The figures 5.29-5.30 shows χ^2 test results of iteration on the data.

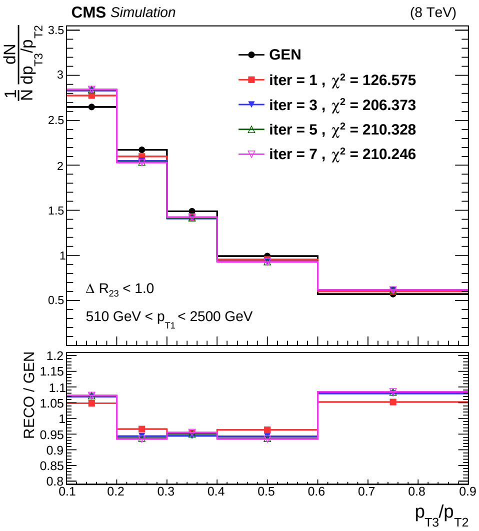

(a)

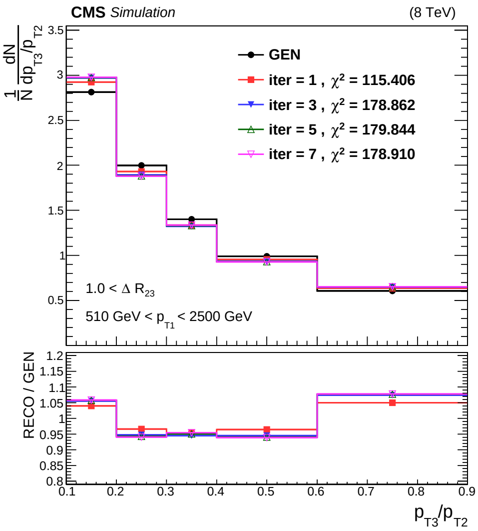

(b)

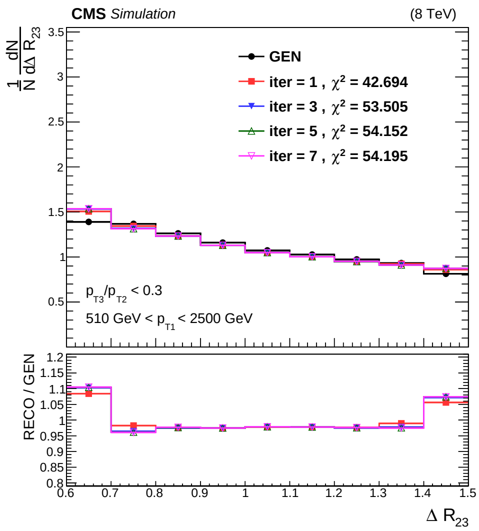

(c)

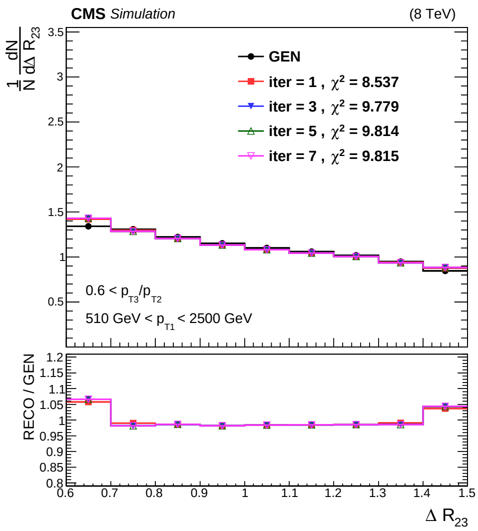

(d)

Figure 5.29: $\sqrt{s} = 8$ TeV the iteration test results. (a) p_{T3}/p_{T2} distribution for the events with a small angle radiation ($\Delta R_{23} < 1.0$), (b) p_{T3}/p_{T2} distribution for the events with a large angle radiation ($\Delta R_{23} > 1.0$), (c) ΔR_{23} distribution for soft p_T radiation case ($p_{T3}/p_{T2} < 0.3$), (d) ΔR_{23} distribution for hard p_T radiation case ($p_{T3}/p_{T2} > 0.6$).

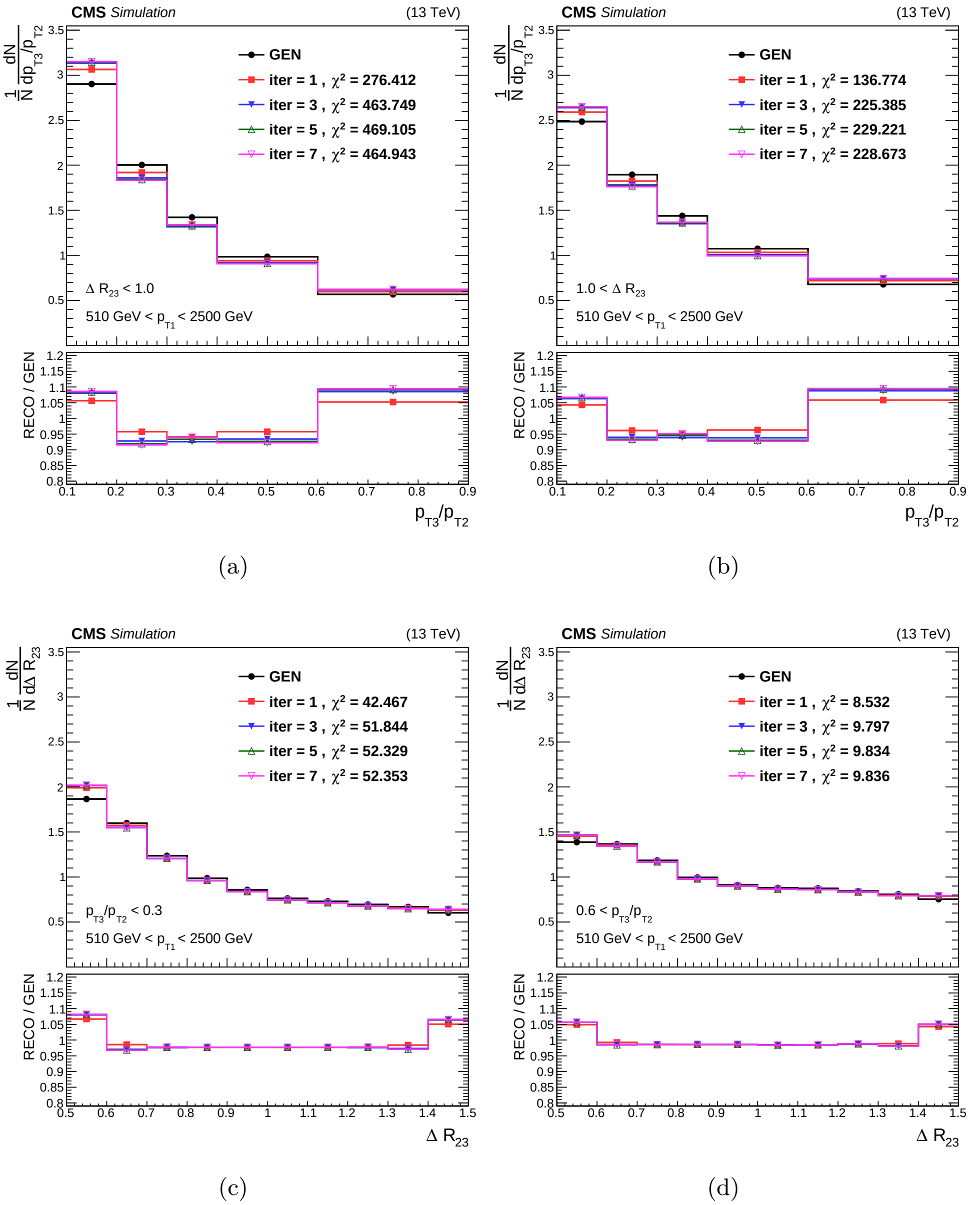

Figure 5.30: $\sqrt{s} = 13$ TeV the iteration test results. (a) p_{T3}/p_{T2} distribution for the events with a small angle radiation ($\Delta R_{23} < 1.0$), (b) p_{T3}/p_{T2} distribution for the events with a large angle radiation ($\Delta R_{23} > 1.0$), (c) ΔR_{23} distribution for soft p_T radiation case ($p_{T3}/p_{T2} < 0.3$), (d) ΔR_{23} distribution for hard p_T radiation case ($p_{T3}/p_{T2} > 0.6$).

5.2.4 Unfolding MC

In this subsection, the detector level distributions are unfolded by tree different unfolding method bin by bin, SVD, and D'Agostini Bayesian. The bin by bin method is based on simple correction factor which is divided the gen distribution by the reco distribution and used to compare with the full unfolding. The D'Agostini Bayesian method is an iterative method and requires the regularization. The comparison of two method shows the different correction at the last bin. The figures 5.31-5.32 are shown the unfolding MC results.

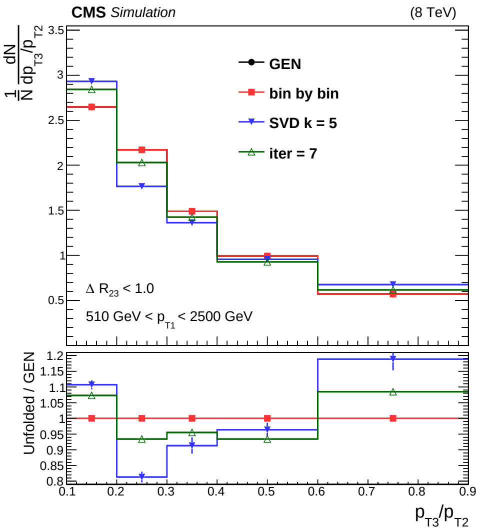

(a)

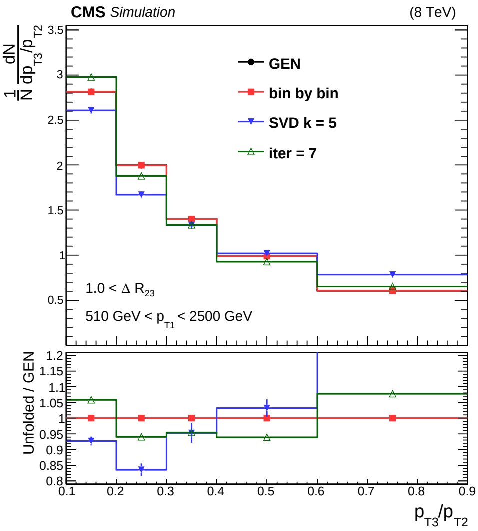

(b)

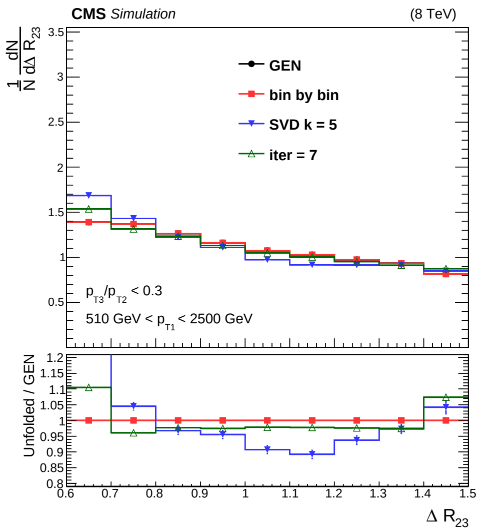

(c)

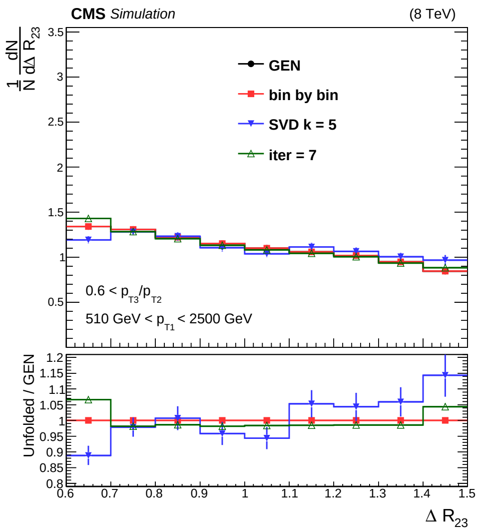

(d)

Figure 5.31: $\sqrt{s} = 8$ TeV the unfolded MC results. (a) p_{T3}/p_{T2} distribution for the events with a small angle radiation ($\Delta R_{23} < 1.0$), (b) p_{T3}/p_{T2} distribution for the events with a large angle radiation ($\Delta R_{23} > 1.0$), (c) ΔR_{23} distribution for soft p_T radiation case ($p_{T3}/p_{T2} < 0.3$), (d) ΔR_{23} distribution for hard p_T radiation case ($p_{T3}/p_{T2} > 0.6$).

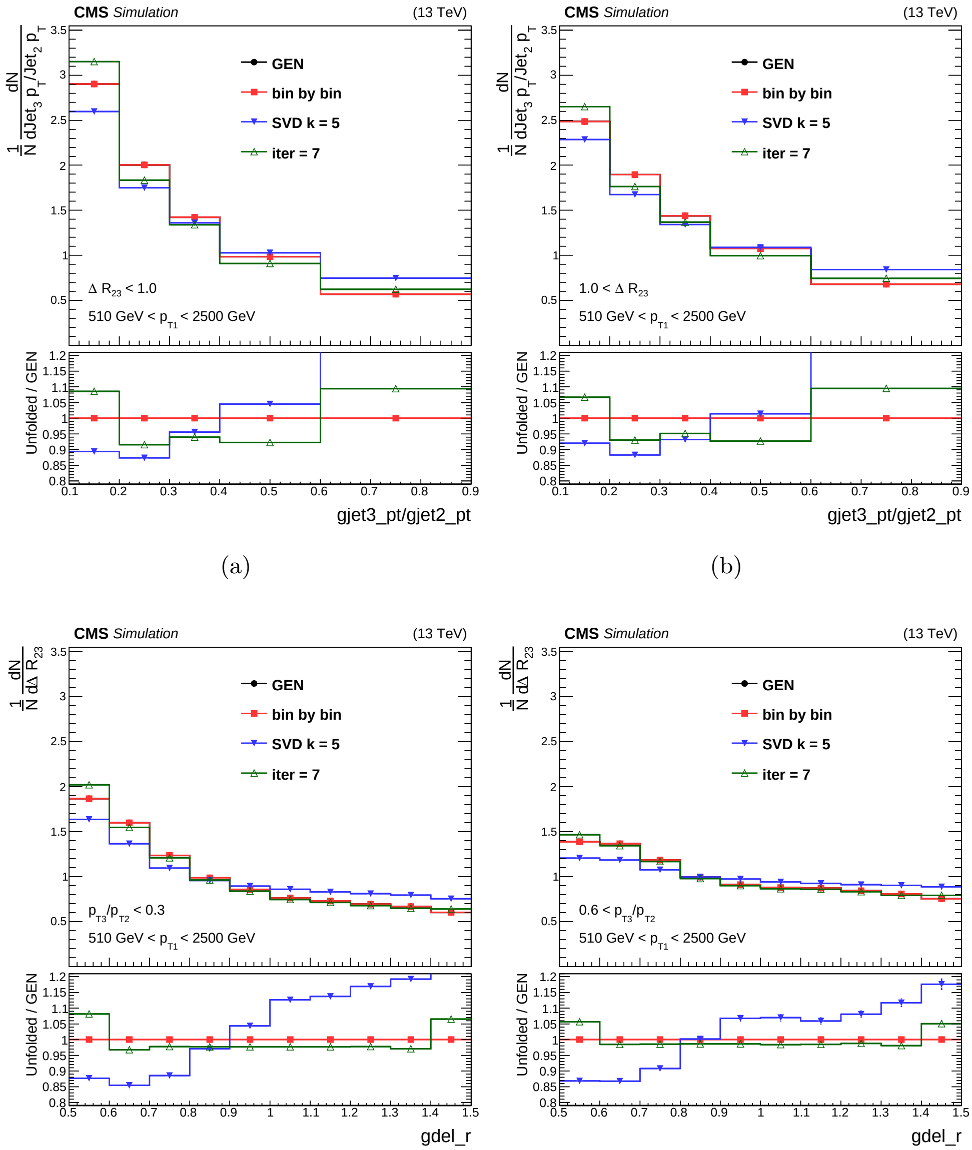

(a) (b) (c) (d)

Figure 5.32: $\sqrt{s} = 13$ TeV the unfolded MC results. (a) p_{T3}/p_{T2} distribution for the events with a small angle radiation ($\Delta R_{23} < 1.0$), (b) p_{T3}/p_{T2} distribution for the events with a large angle radiation ($\Delta R_{23} > 1.0$), (c) ΔR_{23} distribution for soft p_T radiation case ($p_{T3}/p_{T2} < 0.3$), (d) ΔR_{23} distribution for hard p_T radiation case ($p_{T3}/p_{T2} > 0.6$).

5.2.5 Closure test

The closure test is required to validate the software. For this test, half of the statistics are used for building the response matrix, and the other half of the statistics are unfolded. The result is compared to the full statistic unfolding result. The comparison result shows some fluctuation of statistical difference, but the closure test is satisfied. The figures 5.33-5.34 show the closure test results.

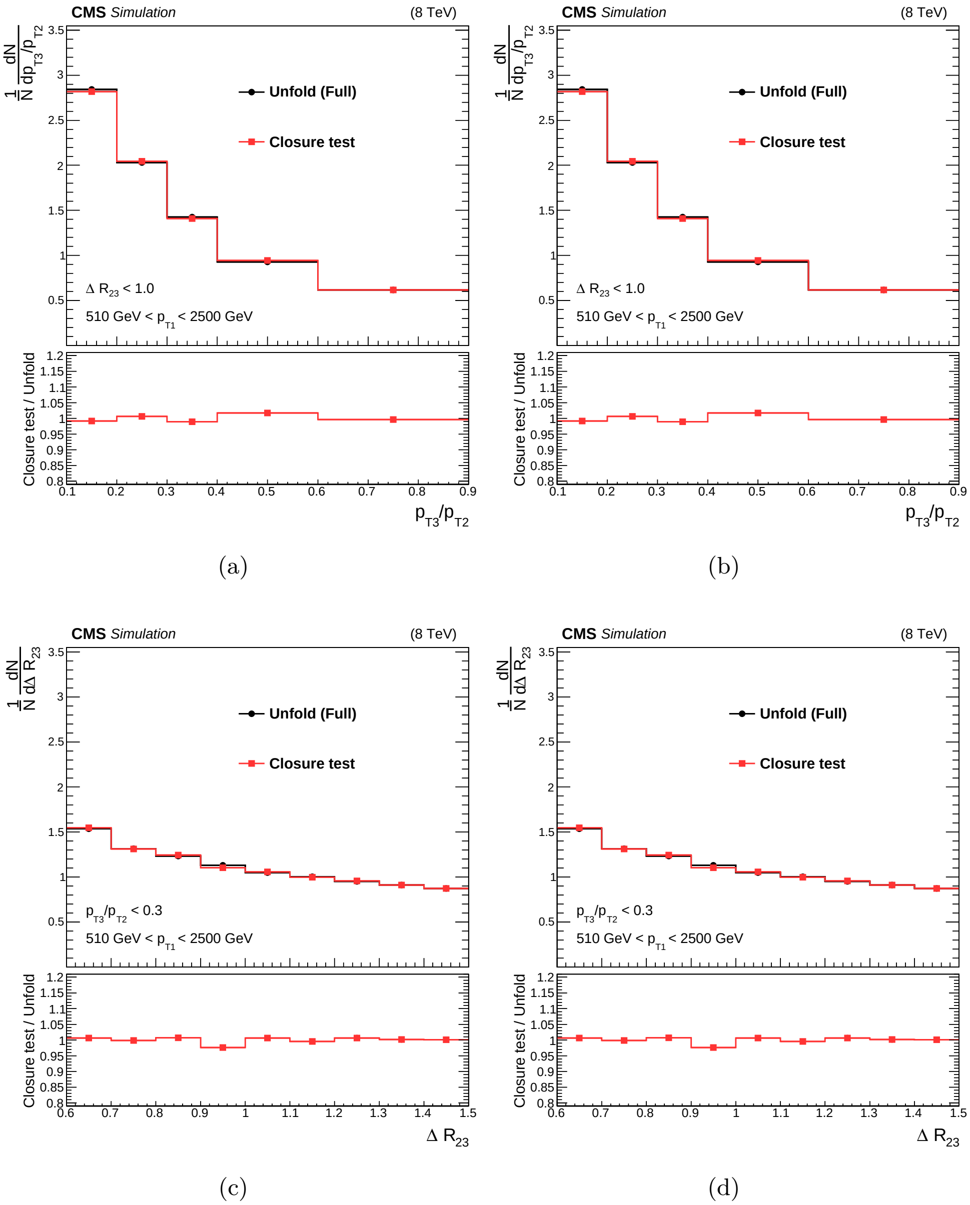

Figure 5.33: $\sqrt{s} = 8$ TeV the closure test results. (a) p_{T3}/p_{T2} distribution for the events with a small angle radiation ($\Delta R_{23} < 1.0$), (b) p_{T3}/p_{T2} distribution for the events with a large angle radiation ($\Delta R_{23} > 1.0$), (c) ΔR_{23} distribution for soft p_T radiation case ($p_{T3}/p_{T2} < 0.3$), (d) ΔR_{23} distribution for hard p_T radiation case ($p_{T3}/p_{T2} > 0.6$).

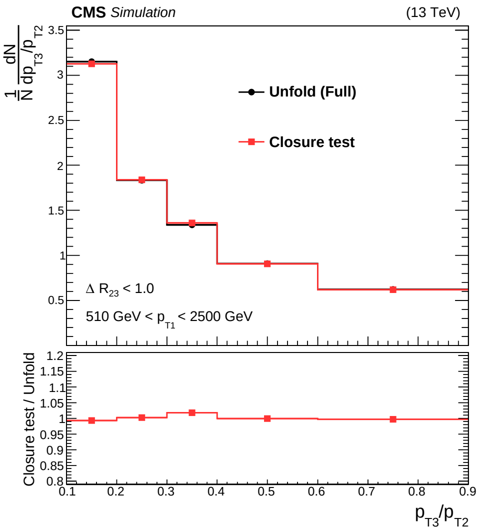

(a)

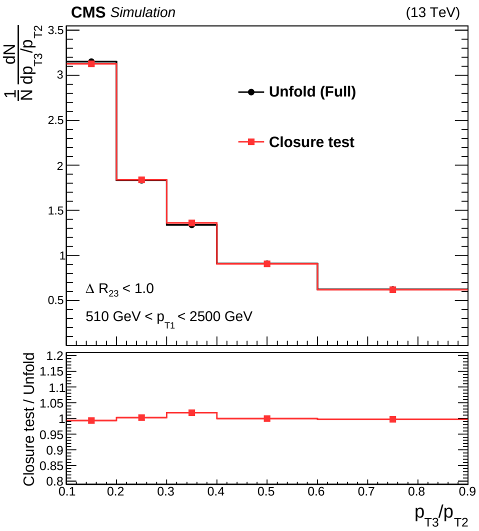

(b)

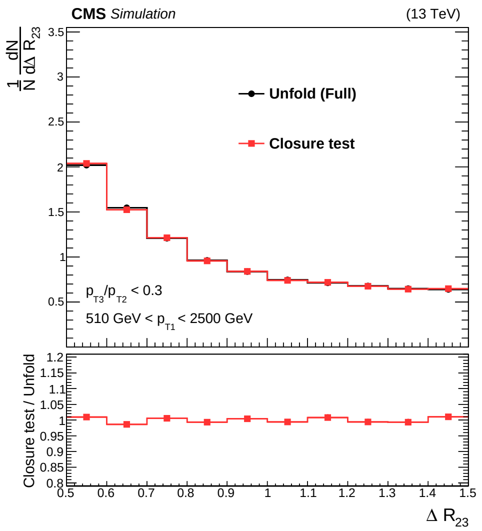

(c)

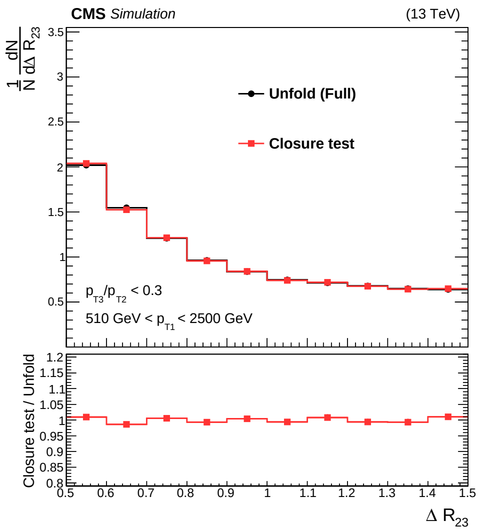

(d)

Figure 5.34: $\sqrt{s} = 13$ TeV the closure test results. (a) $p_{\mathrm{T3}}/p_{\mathrm{T2}}$ distribution for the events with a small angle radiation ($\Delta R_{23} < 1.0$), (b) $p_{\mathrm{T3}}/p_{\mathrm{T2}}$ distribution for the events with a large angle radiation ($\Delta R_{23} > 1.0$), (c) ΔR_{23} distribution for soft p_{T} radiation case ($p_{\mathrm{T3}}/p_{\mathrm{T2}} < 0.3$), (d) ΔR_{23} distribution for hard p_{T} radiation case ($p_{\mathrm{T3}}/p_{\mathrm{T2}} > 0.6$).

5.2.6 Comparison response matrix

The response matrices are built with two full detector simulations, MC PYTHIA 8 and MadGraph. The MadGraph reco distribution is unfolded with two different response matrices and compared. These comparison results show the dependency of unfolding to the physics model. The figures 5.35-5.36 show the comparison response matrix results.

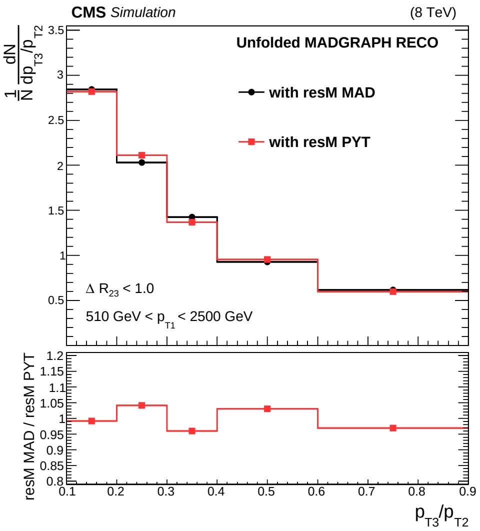

(a)

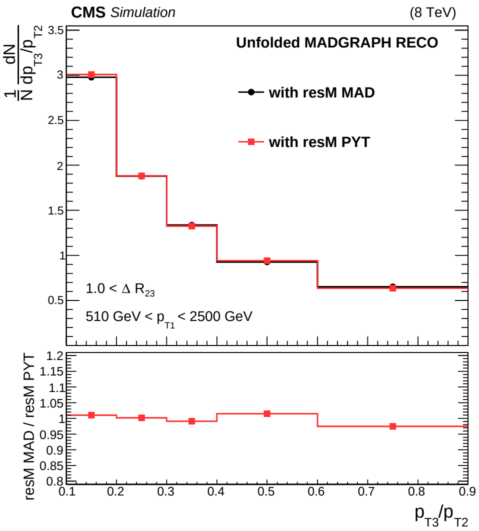

(b)

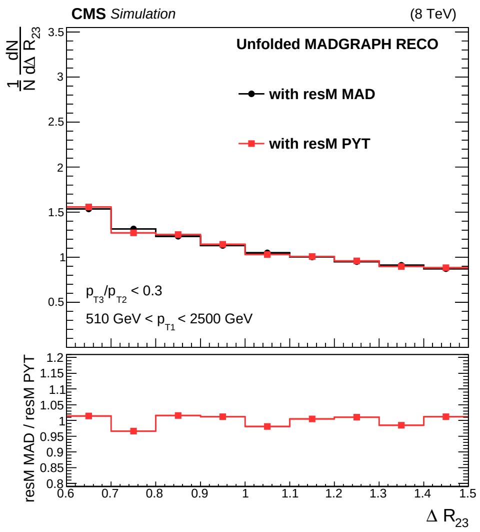

(c)

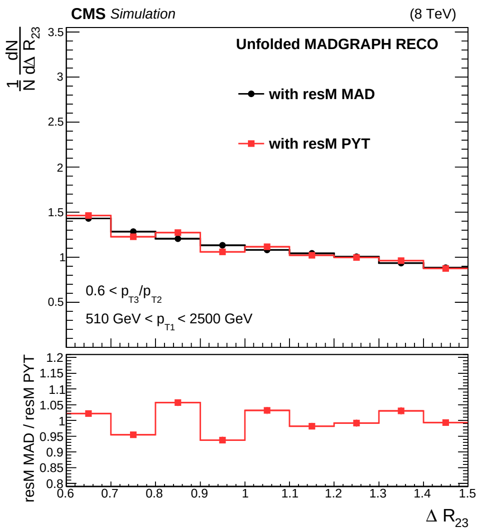

(d)

Figure 5.35: $\sqrt{s} = 8$ TeV the results of comparison response matrices. (a) p_{T3}/p_{T2} distribution for the events with a small angle radiation ($\Delta R_{23} < 1.0$), (b) p_{T3}/p_{T2} distribution for the events with a large angle radiation ($\Delta R_{23} > 1.0$), (c) ΔR_{23} distribution for soft p_T radiation case ($p_{T3}/p_{T2} < 0.3$), (d) ΔR_{23} distribution for hard p_T radiation case ($p_{T3}/p_{T2} > 0.6$).

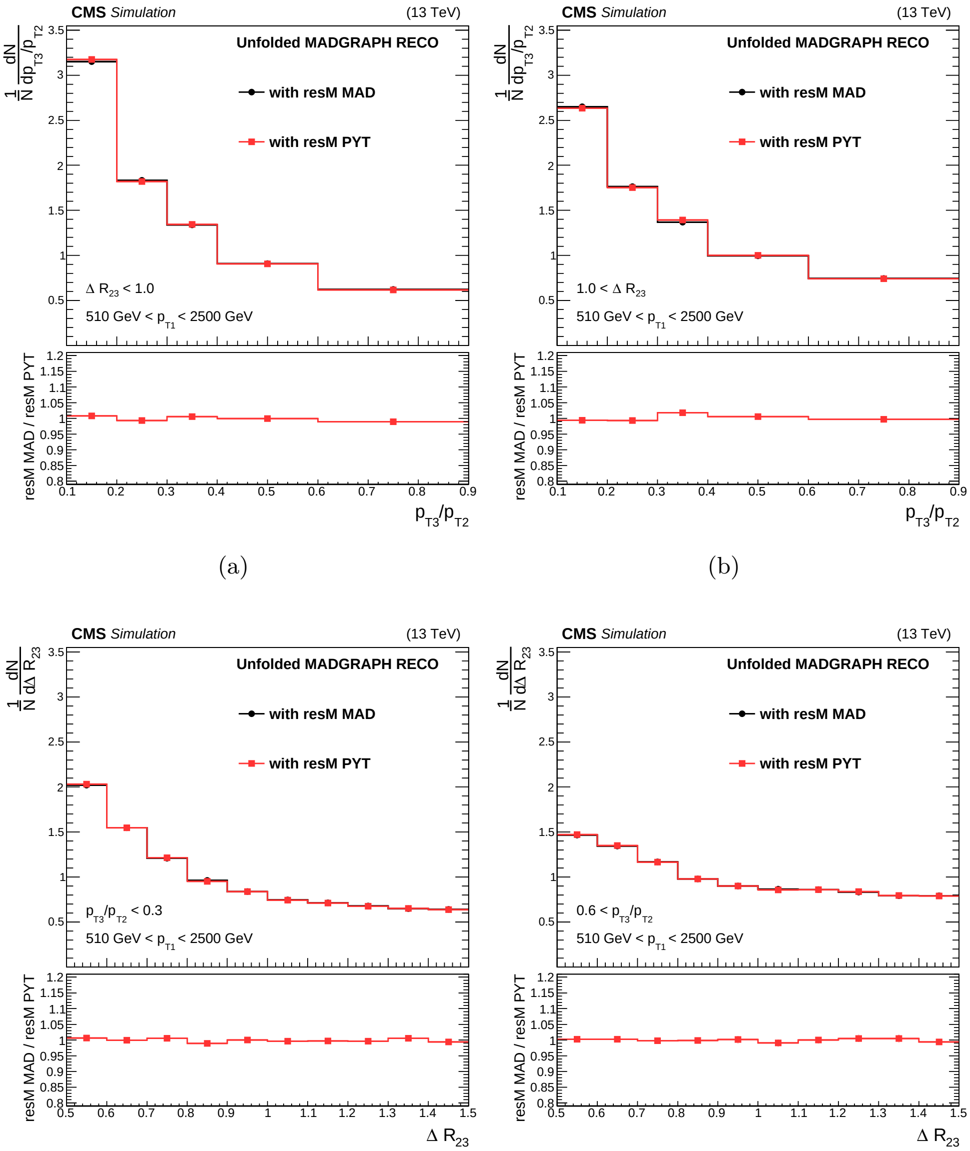

(a) (b) (c) (d)

Figure 5.36: $\sqrt{s} = 13$ TeV the results of comparison response matrices. (a) p_{T3}/p_{T2} distribution for the events with a small angle radiation ($\Delta R_{23} < 1.0$), (b) p_{T3}/p_{T2} distribution for the events with a large angle radiation ($\Delta R_{23} > 1.0$), (c) ΔR_{23} distribution for soft p_T radiation case ($p_{T3}/p_{T2} < 0.3$), (d) ΔR_{23} distribution for hard p_T radiation case ($p_{T3}/p_{T2} > 0.6$).

5.2.7 Unfolding data

The data is unfolded by the MadGraph response matrix. The figures 5.37-5.38 show the unfolded data results. The three different method show the unfolded data distribution, and it clearly shows that the bin-by-bin method calculation of the edged bin is different. Otherwise, the SVD and the D'Agostini methods show similar the results of the unfolding.

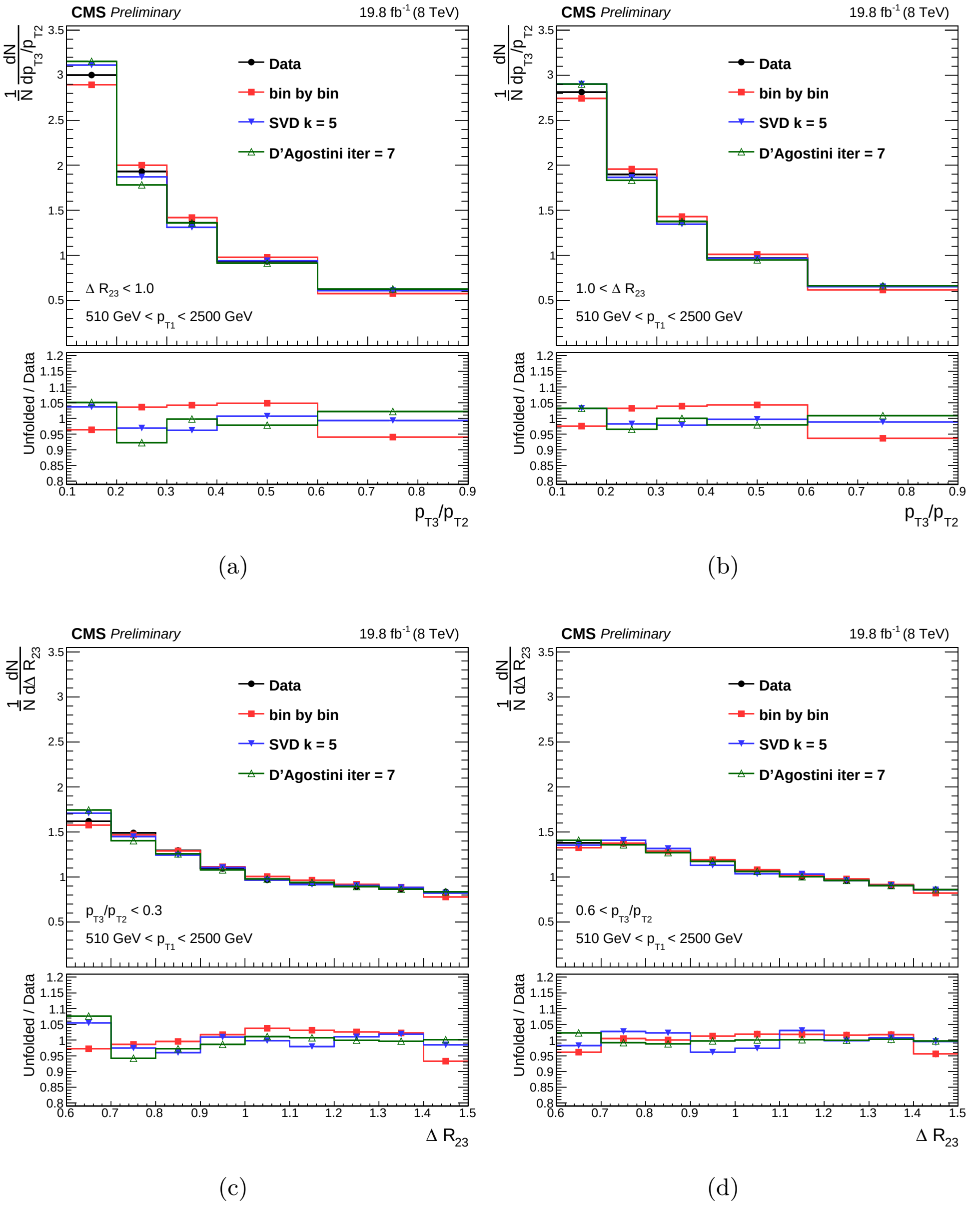

Figure 5.37: $\sqrt{s} = 8$ TeV the unfolded data. (a) $p_{\mathrm{T3}}/p_{\mathrm{T2}}$ distribution for the events with a small angle radiation ($\Delta R_{23} < 1.0$), (b) $p_{\mathrm{T3}}/p_{\mathrm{T2}}$ distribution for the events with a large angle radiation ($\Delta R_{23} > 1.0$), (c) ΔR_{23} distribution for soft p_{T} radiation case ($p_{\mathrm{T3}}/p_{\mathrm{T2}} < 0.3$), (d) ΔR_{23} distribution for hard p_{T} radiation case ($p_{\mathrm{T3}}/p_{\mathrm{T2}} > 0.6$).

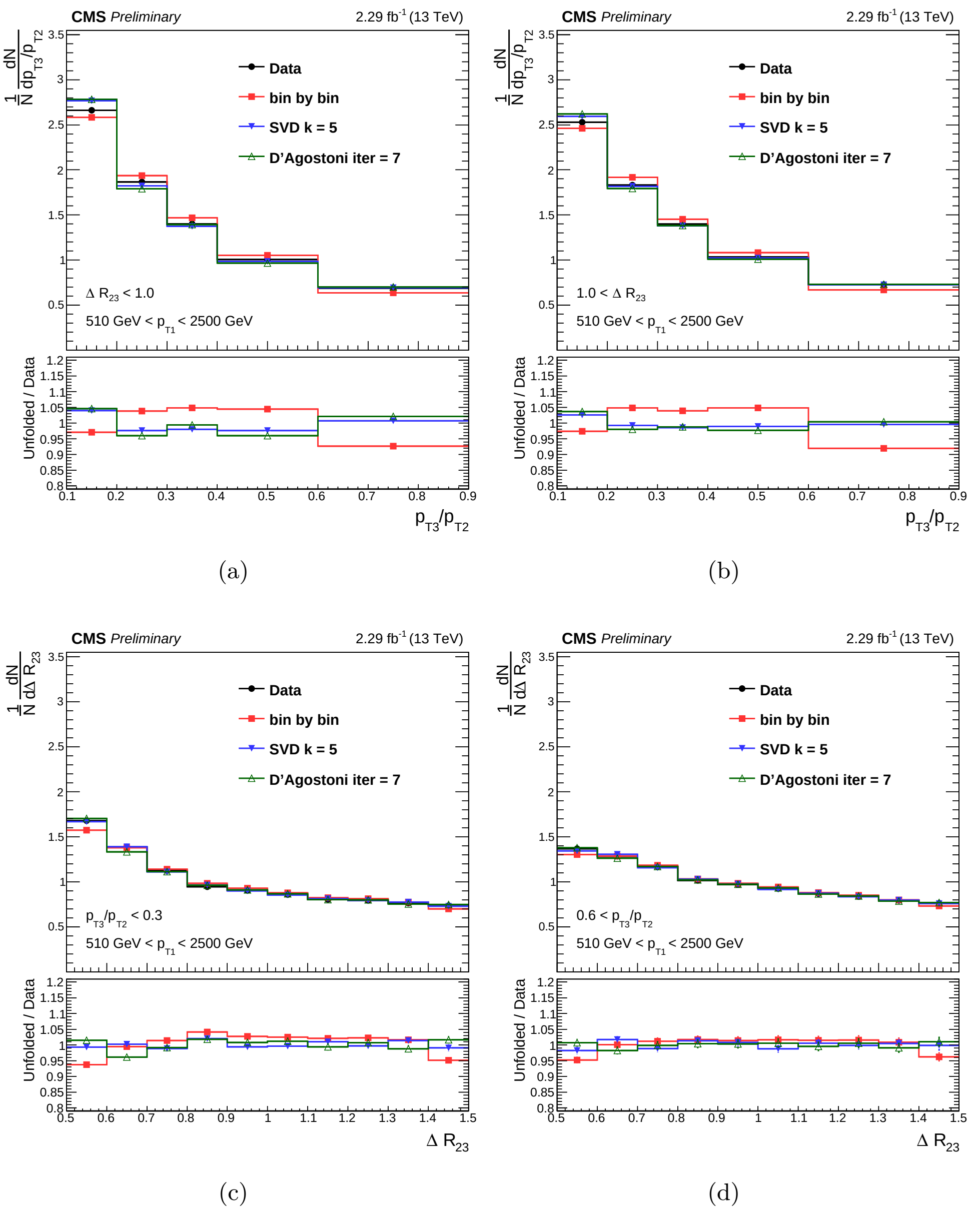

Figure 5.38: $\sqrt{s}$ = 13 TeV the unfolded data. (a) p_{T3}/p_{T2} distribution for the events with a small angle radiation ($\Delta R_{23} < 1.0$), (b) p_{T3}/p_{T2} distribution for the events with a large angle radiation ($\Delta R_{23} > 1.0$), (c) ΔR_{23} distribution for soft p_T radiation case ($p_{T3}/p_{T2} < 0.3$), (d) ΔR_{23} distribution for hard p_T radiation case ($p_{T3}/p_{T2} > 0.6$).

5.2.8 Fractional statistical error

The unfolding leads to changing the statistical error. Figures 5.39-5.40 show the fractional statistical errors for the unfolded. The errors after unfolding are slightly larger as expected.

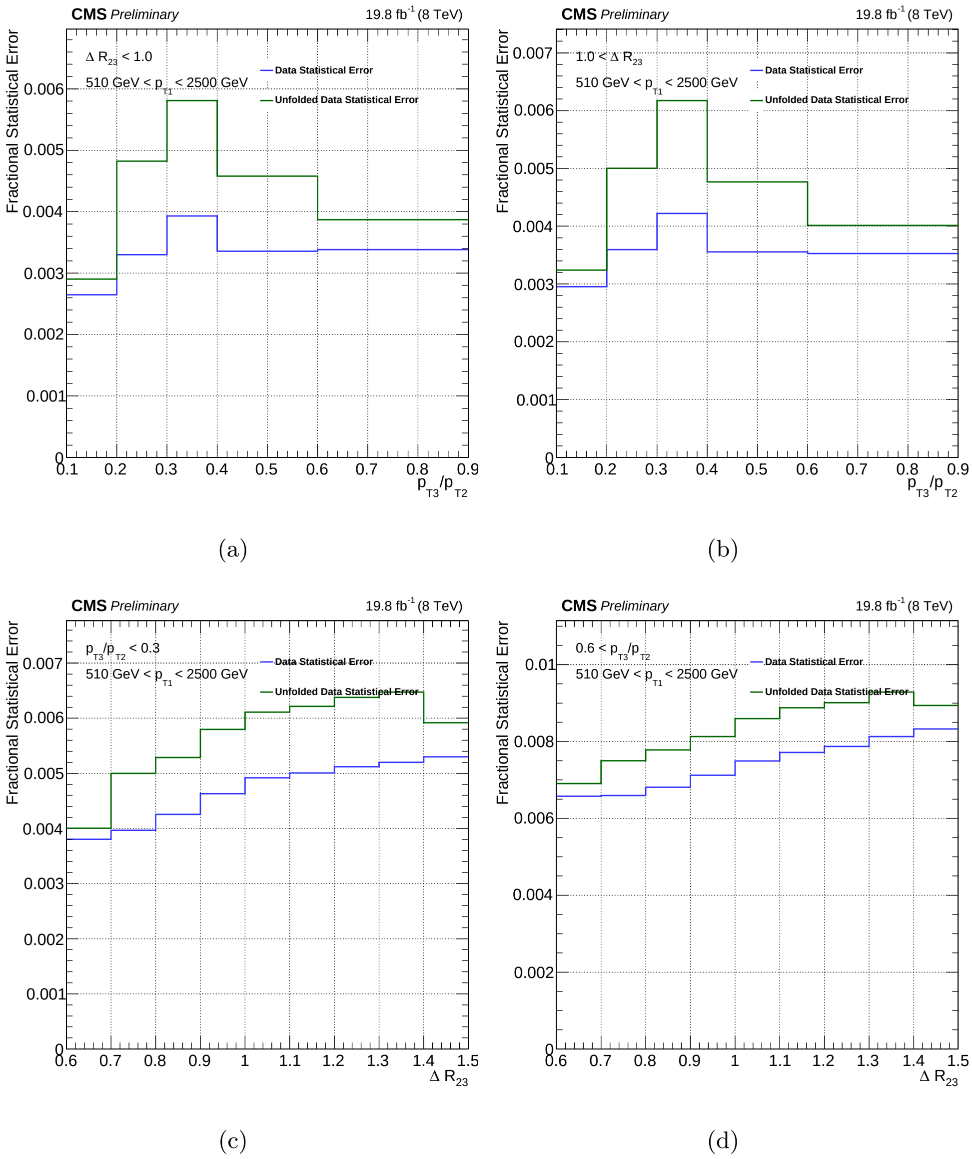

Figure 5.39: $\sqrt{s} = 8$ TeV the fractional statistical error. (a) $p_{\mathrm{T3}}/p_{\mathrm{T2}}$ distribution for the events with a small angle radiation ($\Delta R_{23} < 1.0$), (b) $p_{\mathrm{T3}}/p_{\mathrm{T2}}$ distribution for the events with a large angle radiation ($\Delta R_{23} > 1.0$), (c) ΔR_{23} distribution for soft p_{T} radiation case ($p_{\mathrm{T3}}/p_{\mathrm{T2}} < 0.3$), (d) ΔR_{23} distribution for hard p_{T} radiation case ($p_{\mathrm{T3}}/p_{\mathrm{T2}} > 0.6$).

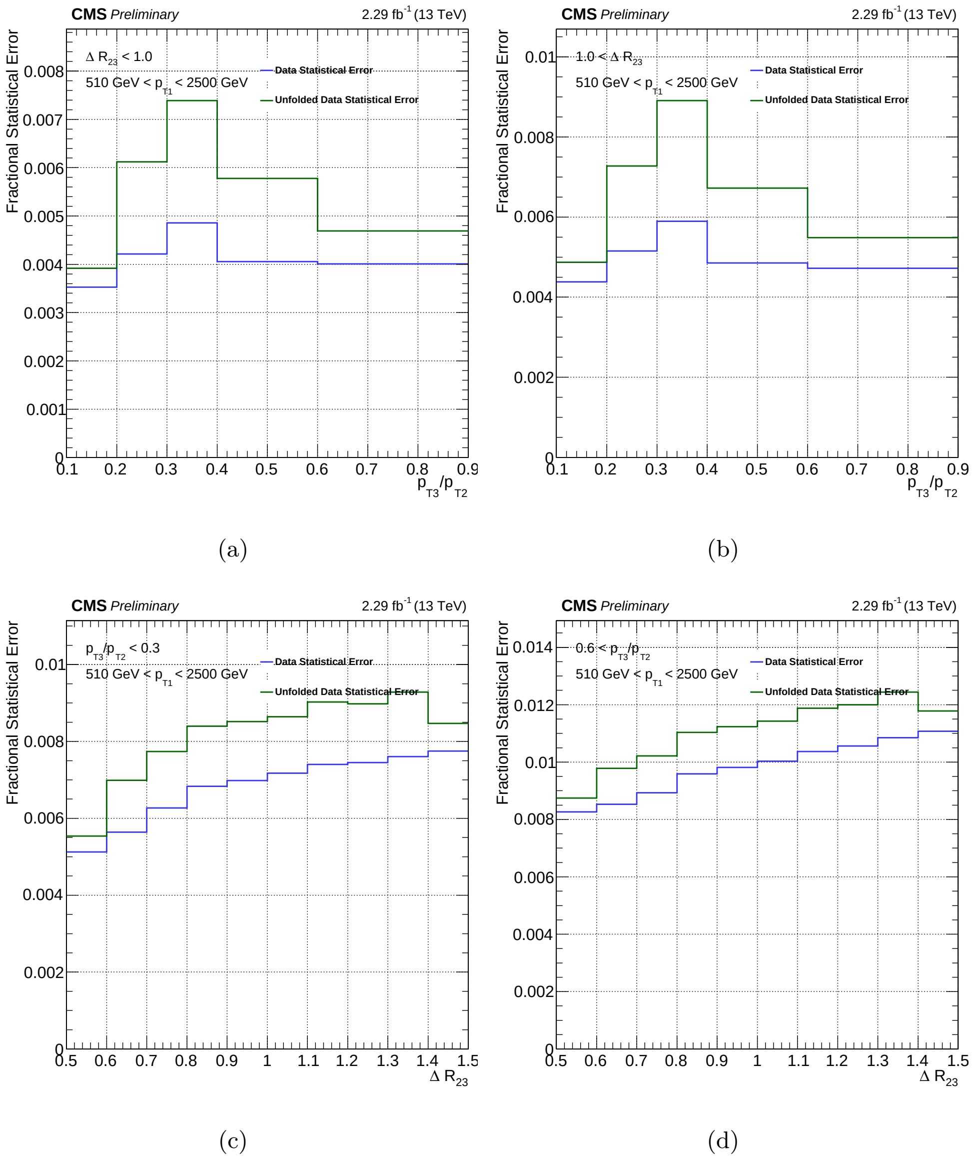

Figure 5.40: $\sqrt{s} = 13$ TeV the fractional statistical error. (a) p_{T3}/p_{T2} distribution for the events with a small angle radiation ($\Delta R_{23} < 1.0$), (b) p_{T3}/p_{T2} distribution for the events with a large angle radiation ($\Delta R_{23} > 1.0$), (c) ΔR_{23} distribution for soft p_T radiation case ($p_{T3}/p_{T2} < 0.3$), (d) ΔR_{23} distribution for hard p_T radiation case ($p_{T3}/p_{T2} > 0.6$).

5.2.9 Bottom line test

A useful sanity check of the unfolded result can be performed by the comparison of some models to the data in the "smeared" space, by smearing the models. If the result of the bottom-line test does not match the criteria just described, the result of the unfolding process should be considered wrong.

Back folding

An essential check of the unfolded results is the effort of folding the obtained distributions back to the detector level by using the MC simulation. This is possible by using the response matrix, to apply acceptance, efficiency, and migrations to the unfolded distributions and manually build the detector effects. In this way, a schematic but reliable detector simulation can be added on top of the "true" level, and the folded spectra can be compared to the measured data distributions. Since no related class is implemented in ROOUNFOLD, the folding exercise has been "manually" set; it is, in particular, performed by applying the following formula:

$$N^i_{\mathrm{fold}} = \sum_{j=1}^{N_{\mathrm{bins}}} \frac{P^{ij} \cdot N^j_{\mathrm{unfold}} \cdot (1 - P^j(\mathrm{Miss}))}{1 - P^j(\mathrm{Fake})} \tag{5.5}$$

The table 5.3 - 5.3 show the results of bottom line test. The three different theoretical predictions are compared with the folding and the unfolding χ^2 values. The results show that the unfolding is performed correctly.

Table 5.3: $\sqrt{s} = 8\,\text{TeV}$ Bottom line test

	p_{T3}/p_{T2} distribution				ΔR_{23} distribution			
	$\Delta R_{23} < 1.0$		$1.0 < \Delta R_{23}$		$p_{T3}/p_{T2} < 0.3$		$0.6 < p_{T3}/p_{T2}$	
χ^2/NDF	fold	unfold	fold	backfold	fold	backfold	fold	backfold
PYTHIA 8 (CUETP8M1)	16.97	16.47	30.98	25.88	6.33	6.38	7.44	6.44
POWHEG + PYTHIA 8	164.52	143.33	98.27	76.54	14.75	15.36	1.25	1.42
MADGRAPH + PYTHIA 8	35.84	23.52	2.55	2.64	18.20	16.19	1.81	1.67

Table 5.4: $\sqrt{s} = 13\,\text{TeV}$ Bottom line test

	p_{T3}/p_{T2} distribution				ΔR_{23} distribution			
	$\Delta R_{23} < 1.0$		$1.0 < \Delta R_{23}$		$p_{T3}/p_{T2} < 0.3$		$0.6 < p_{T3}/p_{T2}$	
χ^2/NDF	fold	unfold	fold	backfold	fold	backfold	fold	backfold
PYTHIA 8 (CUETP8M1)	183.54	147.25	271.10	207.60	30.56	29.07	45.13	42.36
POWHEG + PYTHIA 8	273.16	202.61	157.46	111.98	6.13	6.45	1.37	1.48
MADGRAPH + PYTHIA 8	371.66	179.35	6.72	1.94	236.36	222.95	19.97	18.31

Table 5.5: $\sqrt{s} = 8\,\mathrm{TeV}$ the statistical covariance matrix, $\mathrm{Cov}^{\mathrm{Stat}}$, taking into account the correlations due to unfolding in $p_{\mathrm{T3}}/p_{\mathrm{T2}}$, $\Delta R_{23} < 1.0$ (PS dominant region)

bin	1	2	3	4	5
1	186027.94	-36236.72	-1317.03	2869.99	-603.61
2	-36236.72	150613.95	-26842.42	-3893.07	2246.74
3	-1317.03	-26842.42	119953.53	-27320.94	-203.77
4	2869.99	-3893.07	-27320.94	145336.86	-29442.90
5	-603.61	2246.74	-203.77	-29442.90	117617.24

Table 5.6: $\sqrt{s} = 8\,\mathrm{TeV}$ the statistical covariance matrix, $\mathrm{Cov}^{\mathrm{Stat}}$, taking into account the correlations due to unfolding in $p_{\mathrm{T3}}/p_{\mathrm{T2}}$, $< \Delta R_{23} > 1.0$ (ME dominant region)

bin	1	2	3	4	5
1	145588.22	-28113.55	168.30	1879.99	-414.38
2	-28113.55	128165.71	-24460.38	-1910.90	1646.85
3	168.30	-24460.38	104092.47	-24029.43	344.82
4	1879.99	-1910.90	-24029.43	126753.50	-24736.57
5	-414.38	1646.85	344.82	-24736.57	104463.82

Table 5.5-5.12 show the statistical covariance matrix from the unfolding. Those tables are used for the bottom line test calculation. The covariance matrix values are not normalized.

Table 5.7: $\sqrt{s} = 8$ TeV the statistical covariance matrix, $\mathrm{Cov}^{\mathrm{Stat}}$, taking into account the correlations due to unfolding in ΔR_{23}, $p_{\mathrm{T}3}/p_{\mathrm{T}2} < 0.3$ (PS dominant region)

bin	1	2	3	4	5	6	7	8	9
1	88522.66	-14870.19	819.53	152.15	-59.77	-9.05	2.01	0.09	-0.01
2	-14870.19	87833.11	-13618.95	559.42	187.58	-62.30	0.37	0.57	0.01
3	819.53	-13618.95	78672.76	-12715.53	481.66	162.67	-48.88	1.16	-0.27
4	152.15	559.42	-12715.53	69243.63	-11680.07	437.10	189.07	-41.56	0.69
5	-59.77	187.58	481.66	-11680.07	63271.34	-10856.96	451.25	147.21	-37.77
6	-9.05	-62.30	162.67	437.10	-10856.96	60481.34	-10504.27	456.85	135.73
7	2.01	0.37	-48.88	189.07	451.25	-10504.27	57480.99	-9927.38	583.15
8	0.09	0.57	1.16	-41.56	147.21	456.85	-9927.38	55610.51	-9247.20
9	-0.01	0.01	-0.27	0.69	-37.77	135.73	583.15	-9247.20	44301.40

Table 5.8: $\sqrt{s} = 8$ TeV the statistical covariance matrix, $\mathrm{Cov}^{\mathrm{Stat}}$, taking into account the correlations due to unfolding in ΔR_{23}, $p_{\mathrm{T}3}/p_{\mathrm{T}2} > 0.6$ (ME dominant region)

bin	1	2	3	4	5	6	7	8	9
1	26705.03	-3194.31	173.65	3.22	-2.79	0.19	0.06	0.01	0.00
2	-3194.31	29129.69	-3248.30	148.25	3.47	-3.58	0.11	-0.53	0.06
3	173.65	-3248.30	27405.87	-3131.14	145.20	0.62	-10.80	1.03	-0.00
4	3.22	148.25	-3131.14	25483.62	-2933.77	133.67	1.32	-1.92	0.06
5	-2.79	3.47	145.20	-2933.77	23345.85	-2869.68	149.31	4.00	-2.29
6	0.19	-3.58	0.62	133.67	-2869.68	22159.62	-2720.61	137.61	2.43
7	0.06	0.11	-10.80	1.32	149.31	-2720.61	21086.94	-2458.47	128.29
8	0.01	-0.53	1.03	-1.92	4.00	137.61	-2458.47	19777.84	-2262.79
9	0.00	0.06	-0.00	0.06	-2.29	2.43	128.29	-2262.79	16548.96

Table 5.9: $\sqrt{s} = 13\,\text{TeV}$ the statistical covariance matrix, Cov^{Stat}, taking into account the correlations due to unfolding in $p_{\text{T}3}/p_{\text{T}2}$, $\Delta R_{23} < 1.0$ (PS dominant region)

bin	1	2	3	4	5
1	109477.69	-27968.91	2557.75	1583.91	-663.09
2	-27968.91	110598.57	-30238.39	626.00	1603.48
3	2557.75	-30238.39	97613.97	-29664.05	2130.17
4	1583.91	626.00	-29664.05	114738.54	-28475.65
5	-663.09	1603.48	2130.17	-28475.65	89346.11

Table 5.10: $\sqrt{s} = 13\,\text{TeV}$ the statistical covariance matrix, Cov^{Stat}, taking into account the correlations due to unfolding in $p_{\text{T}3}/p_{\text{T}2}$, $\Delta R_{23} > 1.0$ (ME dominant region)

bin	1	2	3	4	5
1	69691.52	-17509.54	1981.81	697.48	-316.79
2	-17509.54	72787.89	-19893.85	1213.32	712.57
3	1981.81	-19893.85	64702.92	-20015.29	1867.02
4	697.48	1213.32	-20015.29	78407.46	-18508.93
5	-316.79	712.57	1867.02	-18508.93	61607.81

Table 5.11: $\sqrt{s} = 13\,\text{TeV}$ the statistical covariance matrix, Cov^{Stat}, taking into account the correlations due to unfolding in ΔR_{23}, $p_{T3}/p_{T2} < 0.3$ (PS dominant region)

bin	1	2	3	4	5	6	7	8	9	10
1	45686.09	-7574.19	675.40	-59.89	-18.38	-21.28	-20.77	-12.64	-20.01	-0.93
2	-7574.19	44583.34	-7325.31	623.32	-30.42	-33.05	-13.99	-10.23	-16.25	-0.71
3	675.40	-7325.31	38101.11	-6747.39	605.84	-30.94	-26.68	-8.48	-16.80	-0.74
4	-59.89	623.32	-6747.39	33441.95	-5943.45	523.40	-46.78	-22.27	-21.80	-1.46
5	-18.38	-30.42	605.84	-5943.45	30916.76	-5287.17	471.06	-14.20	-12.84	1.45
6	-21.28	-33.05	-30.94	523.40	-5287.17	28859.25	-4782.73	420.64	-37.25	-6.27
7	-20.77	-13.99	-26.68	-46.78	471.06	-4782.73	26803.09	-4677.88	410.74	-21.70
8	-12.64	-10.23	-8.48	-22.27	-14.20	420.64	-4677.88	26498.95	-4438.79	400.06
9	-20.01	-16.25	-16.80	-21.80	-12.84	-37.25	410.74	-4438.79	25156.22	-3969.75
10	-0.93	-0.71	-0.74	-1.46	1.45	-6.27	-21.70	400.06	-3969.75	20564.65

Table 5.12: $\sqrt{s} = 13\,\text{TeV}$ the statistical covariance matrix, Cov^{Stat}, taking into account the correlations due to unfolding in ΔR_{23}, $p_{T3}/p_{T2} > 0.6$ (ME dominant region)

bin	1	2	3	4	5	6	7	8	9	10
1	16682.44	-2017.49	135.63	-6.85	-1.24	0.20	-0.01	-0.00	0.00	0.00
2	-2017.49	17516.54	-2072.99	131.43	-5.93	-0.96	0.21	-0.01	-0.00	-0.00
3	135.63	-2072.99	16398.79	-2031.09	126.76	-8.90	0.06	0.11	-0.01	-0.00
4	-6.85	131.43	-2031.09	14576.58	-1830.77	114.04	-4.46	-0.48	0.12	-0.01
5	-1.24	-5.93	126.76	-1830.77	13720.15	-1672.21	110.68	-3.79	-0.41	0.10
6	0.20	-0.96	-8.90	114.04	-1672.21	13078.54	-1586.47	103.54	-3.99	-0.18
7	-0.01	0.21	0.06	-4.46	110.68	-1586.47	12136.11	-1461.51	92.03	-3.68
8	-0.00	-0.01	0.11	-0.48	-3.79	103.54	-1461.51	11726.10	-1409.03	82.59
9	0.00	-0.00	-0.01	0.12	-0.41	-3.99	92.03	-1409.03	11007.88	-1248.71
10	0.00	-0.00	-0.00	-0.01	0.10	-0.18	-3.68	82.59	-1248.71	9428.18

6 Systematic Uncertainties

Besides the statistical ones, which only deal with the number of selected events, the systematic uncertainties are also significant: they have different origins, going from known detector effects to the specific choice of the models used for the correction of the data. The uncertainties have estimated with the normalized distributions: the latter results to be smaller than the former, because they include only migration effects within the phase space, while the ones into and out of the phase space are excluded.

6.1 Jet Energy Scale

One of the significant uncertainties in jet measurements is the jet energy scale (JES). The energy deposited in the detector, reconstructed as a jet, needs to be corrected to obtain a stable measurement to match as accurately as possible to the kinematical quantities of the object from which it originates. The JES is a small remaining correction of the jet energy for matching of MC to data. The JES considers the difference between the nominal distribution and scales up/down distribution. When applying the jet energy scale uncertainties, symmetric differences which consider in the up and down directions, concerning the nominal distributions. The figures 6.1-6.2 show JES for $p_{\mathrm{T3}}/p_{\mathrm{T2}}$ and ΔR_{23} in PS and ME dominant region. The black dot line represents nominal data. The JES shift up (red line) which is 1 σ up and the JES shift down (blue line) which is 1 σ down.

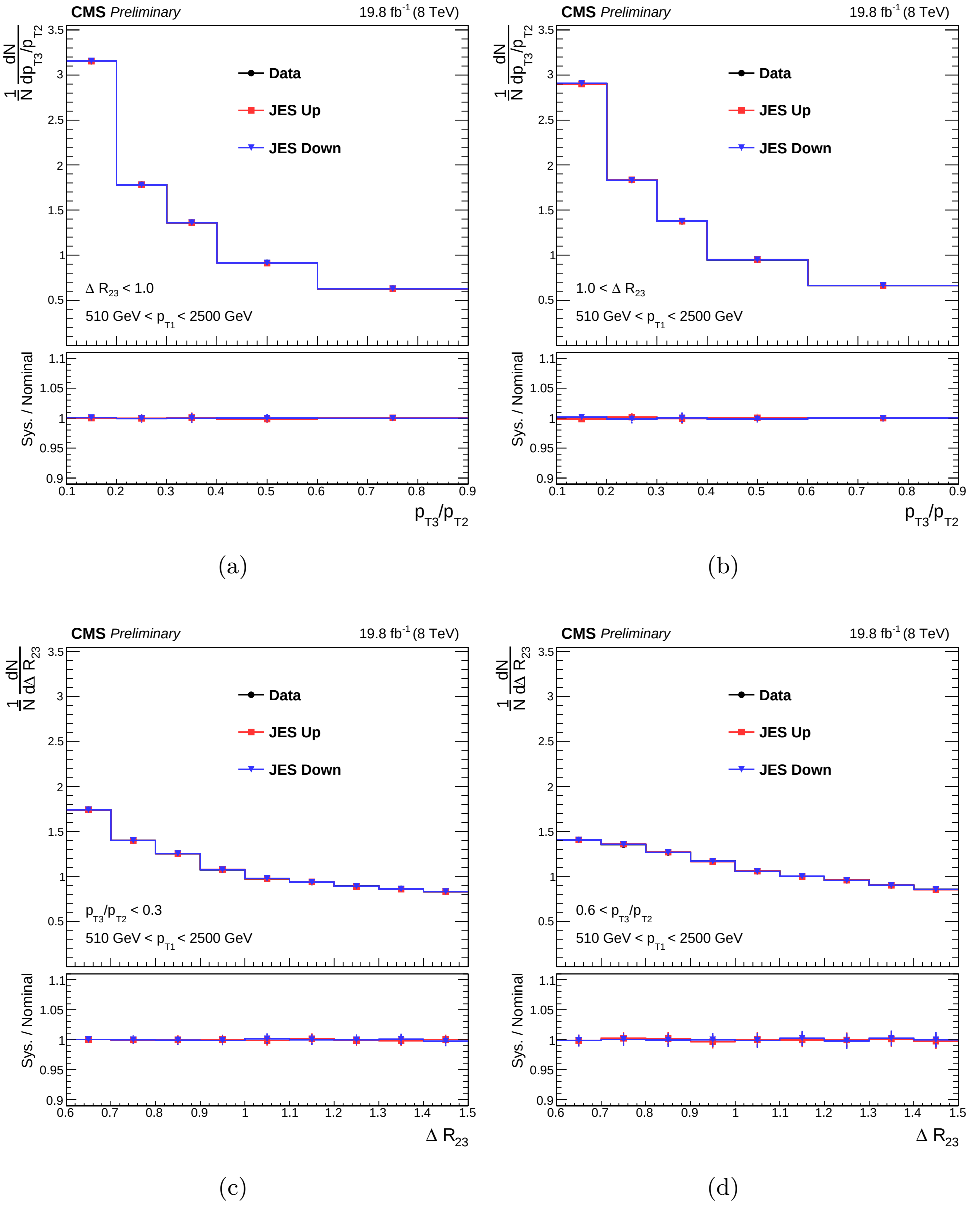

Figure 6.1: $\sqrt{s} = 8$ TeV JES systematic uncertainty. (a) p_{T3}/p_{T2} distribution for the events with a small angle radiation ($\Delta R_{23} < 1.0$), (b) p_{T3}/p_{T2} distribution for the events with a large angle radiation ($\Delta R_{23} > 1.0$), (c) ΔR_{23} distribution for soft p_T radiation case ($p_{T3}/p_{T2} < 0.3$), (d) ΔR_{23} distribution for hard p_T radiation case ($p_{T3}/p_{T2} > 0.6$).

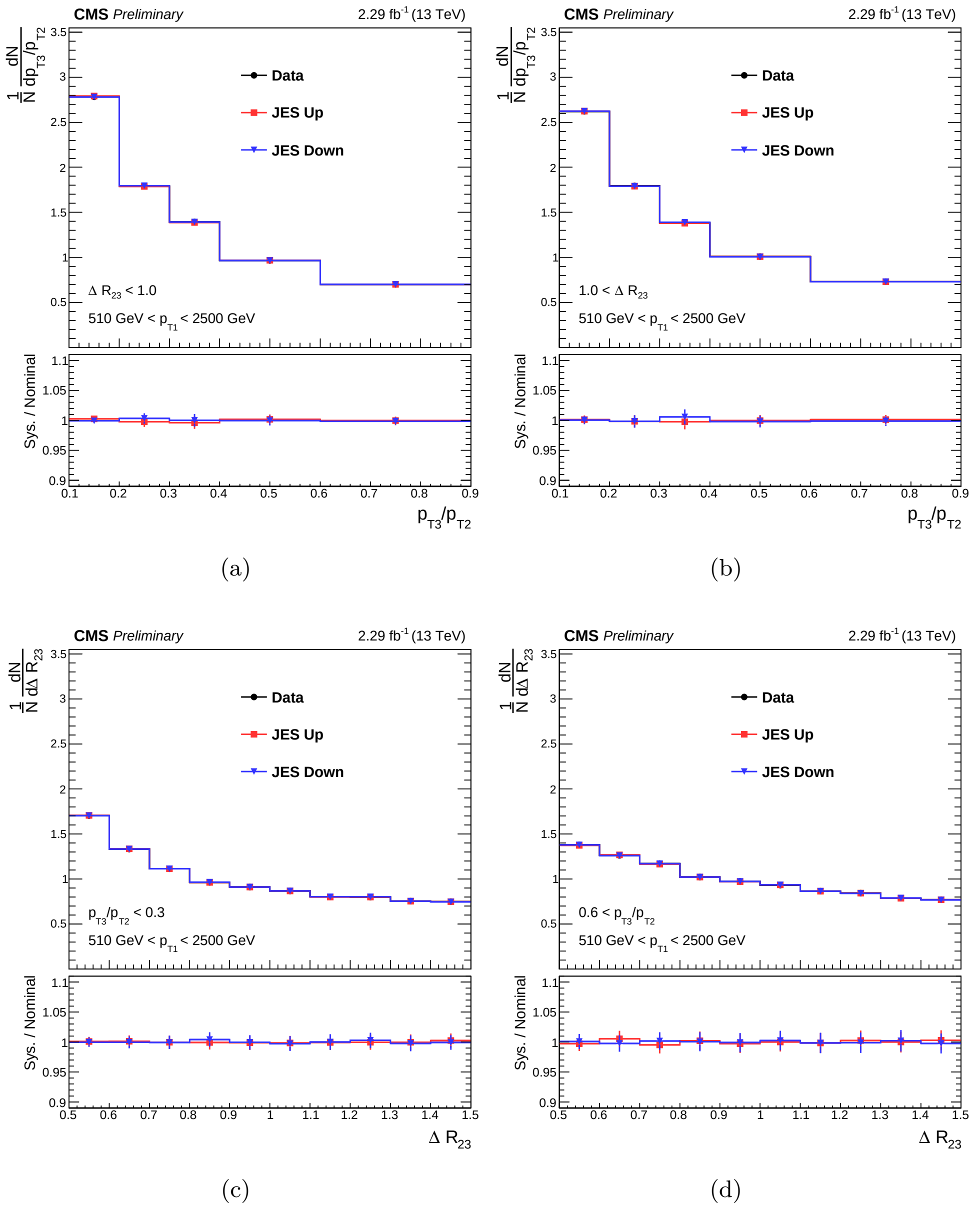

Figure 6.2: $\sqrt{s} = 13$ TeV JES systematic uncertainty. (a) p_{T3}/p_{T2} distribution for the events with a small angle radiation ($\Delta R_{23} < 1.0$), (b) p_{T3}/p_{T2} distribution for the events with a large angle radiation ($\Delta R_{23} > 1.0$), (c) ΔR_{23} distribution for soft p_T radiation case ($p_{T3}/p_{T2} < 0.3$), (d) ΔR_{23} distribution for hard p_T radiation case ($p_{T3}/p_{T2} > 0.6$).

6.2 Jet Energy Resolution

The detector response does not exactly correspond to the true value. This response follows a Gaussian distribution, and the broader the distribution is, the less accurate. The Gaussian width of this distribution is called the resolution. While the final angular resolutions in η and ϕ in CMS have a negligible effect for the described measurement, the resolution in p_{T}, which is equivalent to the one in energy, is more relevant and its impact needs to be take into account. The jet energy resolution (JER) is an important detector effect of the jet energy difference in truth jet and reco jet. The CMS Collaboration provides the correction factors which depends on jet η. The table 6.1 shows the JER scale factors. The nominal is a black dot line on MC. The JER up/down which is the red/blue line, and it is divided by nominal for getting the JER systematic. Figure 6.3-6.4 show the JER systematic.

Table 6.1: The scale factors for $\sqrt{s} = 8\,\mathrm{TeV}$ (13 TeV) JER

	JER	JER-up	JER-down
$\lvert\eta\rvert < 0.5$	1.079 (1.086)	1.105 (1.195)	1.053 (0.977)
$\lvert\eta\rvert < 1.1$	1.099 (1.128)	1.127 (1.241)	1.071 (1.015)
$\lvert\eta\rvert < 1.7$	1.121 (1.143)	1.150 (1.257)	1.092 (1.029)
$\lvert\eta\rvert < 2.3$	1.208 (1.109)	1.254 (1.220)	1.162 (0.998)
$\lvert\eta\rvert < 2.8$	1.254 (1.254)	1.316 (1.379)	1.192 (1.128)
$\lvert\eta\rvert < 3.2$	1.395 (1.395)	1.458 (1.535)	1.332 (1.256)
$\lvert\eta\rvert < 5.0$	1.056 (1.056)	1.247 (1.247)	0.865 (0.865)

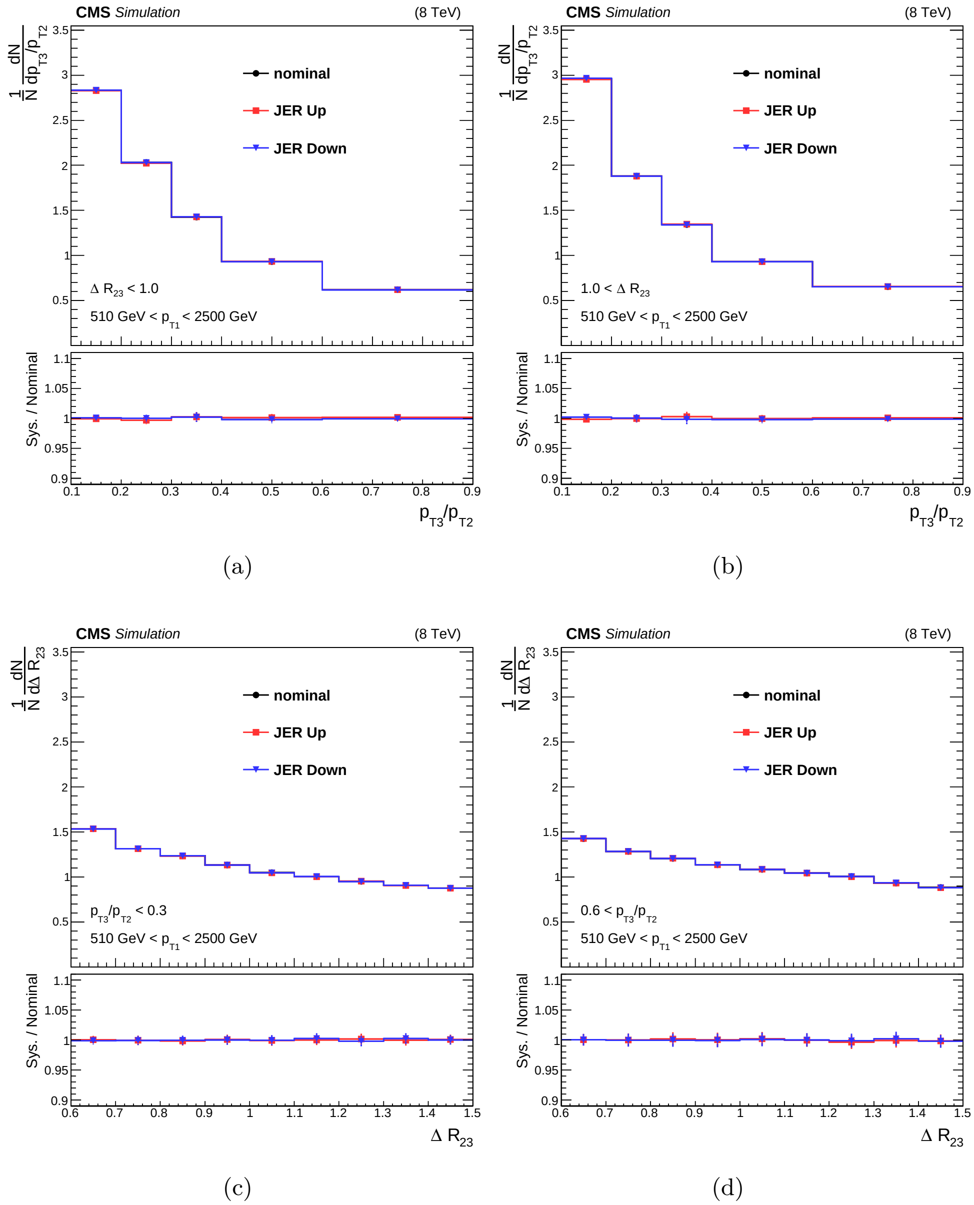

Figure 6.3: $\sqrt{s} = 8$ TeV JER systematic uncertainty. (a) p_{T3}/p_{T2} distribution for the events with a small angle radiation ($\Delta R_{23} < 1.0$), (b) p_{T3}/p_{T2} distribution for the events with a large angle radiation ($\Delta R_{23} > 1.0$), (c) ΔR_{23} distribution for soft p_T radiation case ($p_{T3}/p_{T2} < 0.3$), (d) ΔR_{23} distribution for hard p_T radiation case ($p_{T3}/p_{T2} > 0.6$).

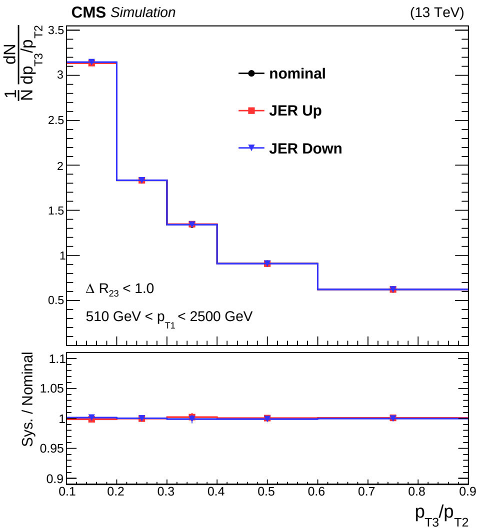

(a)

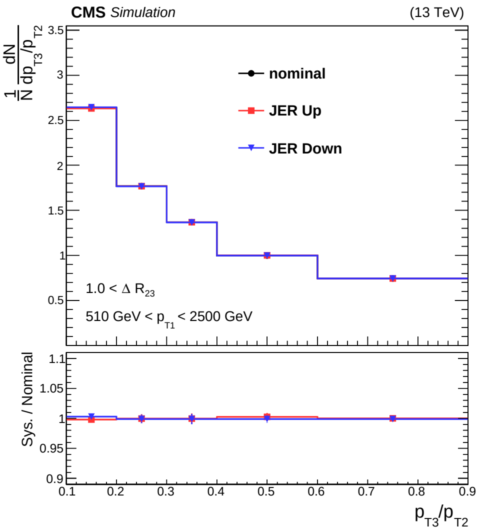

(b)

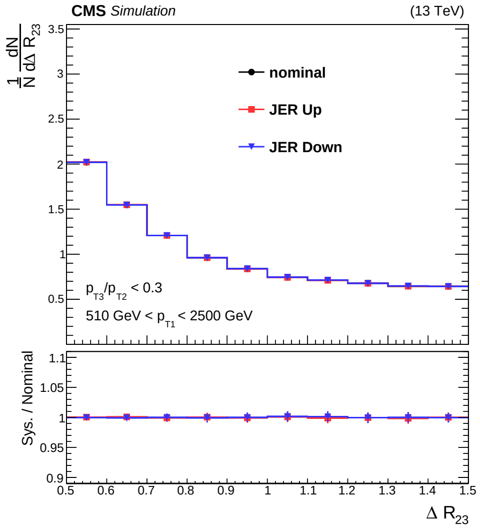

(c)

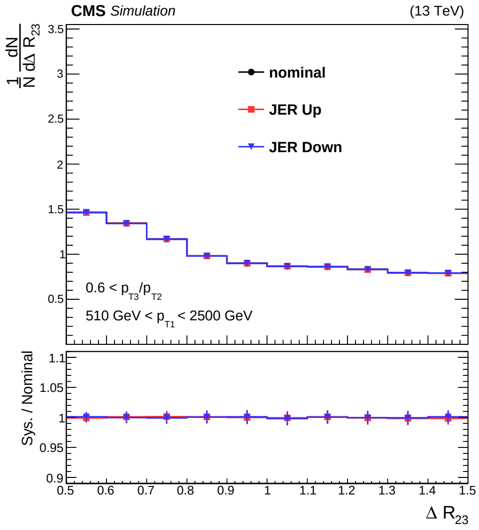

(d)

Figure 6.4: $\sqrt{s} = 13$ TeV JER systematic uncertainty. (a) p_{T3}/p_{T2} distribution for the events with a small angle radiation ($\Delta R_{23} < 1.0$), (b) p_{T3}/p_{T2} distribution for the events with a large angle radiation ($\Delta R_{23} > 1.0$), (c) ΔR_{23} distribution for soft p_T radiation case ($p_{T3}/p_{T2} < 0.3$), (d) ΔR_{23} distribution for hard p_T radiation case ($p_{T3}/p_{T2} > 0.6$).

6.3 Pileup

The pileup (PU) weighting procedure also includes a systematic effect for the measurements depending on how well the primary vertex distribution in data matches the one in the simulation. The PU weight is estimated from the measured total inelastic cross section bunch by bunch. The PU systematic uncertainty is calculated by variation of the cross-section within $\pm$ 5 %. The PU up/down which 5 % up/down is the red/blue line, and it is divided by nominal for getting PU systematic. Figure 6.5-6.6 show the PU systematic.

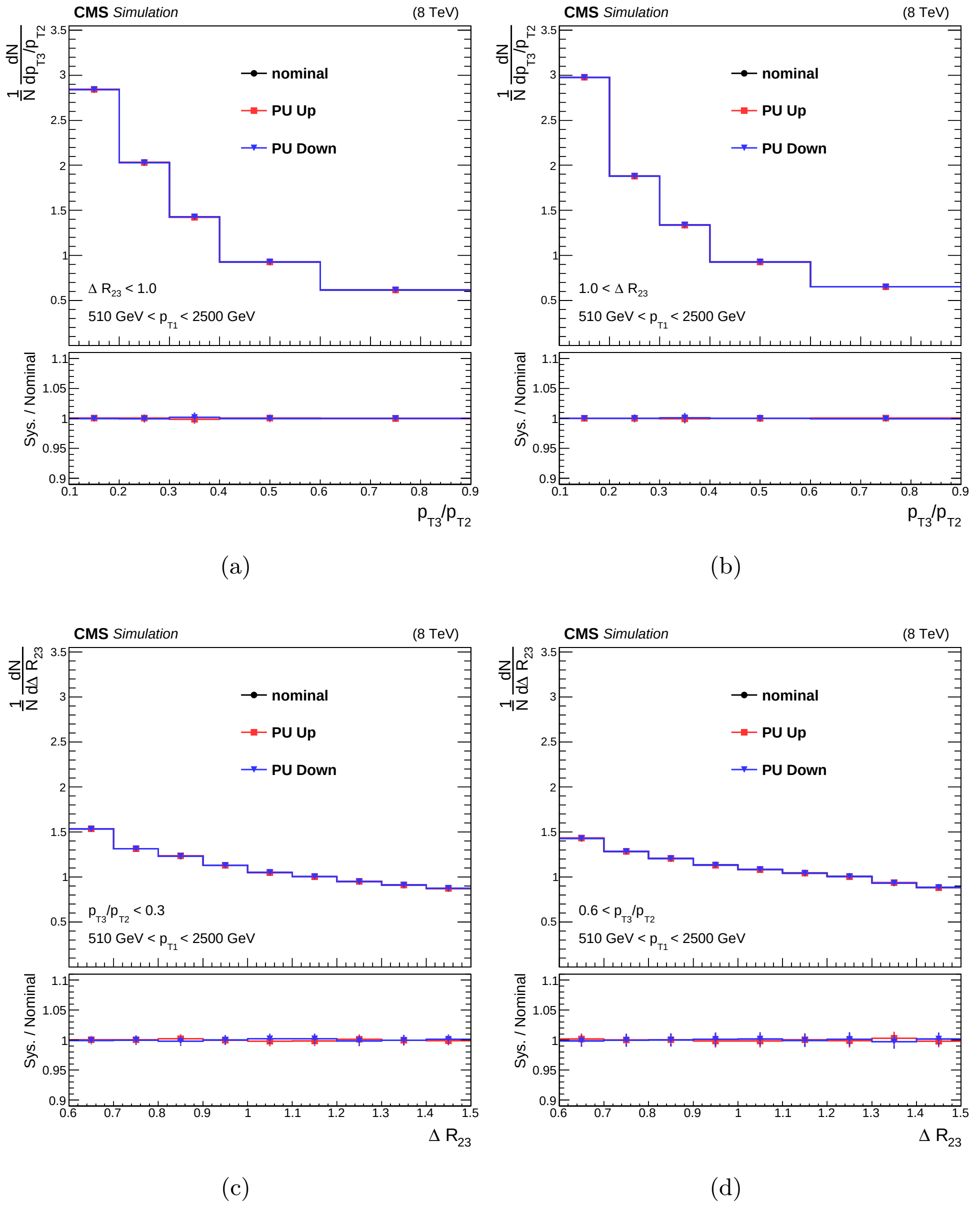

Figure 6.5: $\sqrt{s} = 8$ TeV PU systematic uncertainty. (a) p_{T3}/p_{T2} distribution for the events with a small angle radiation ($\Delta R_{23} < 1.0$), (b) p_{T3}/p_{T2} distribution for the events with a large angle radiation ($\Delta R_{23} > 1.0$), (c) ΔR_{23} distribution for soft p_T radiation case ($p_{T3}/p_{T2} < 0.3$), (d) ΔR_{23} distribution for hard p_T radiation case ($p_{T3}/p_{T2} > 0.6$).

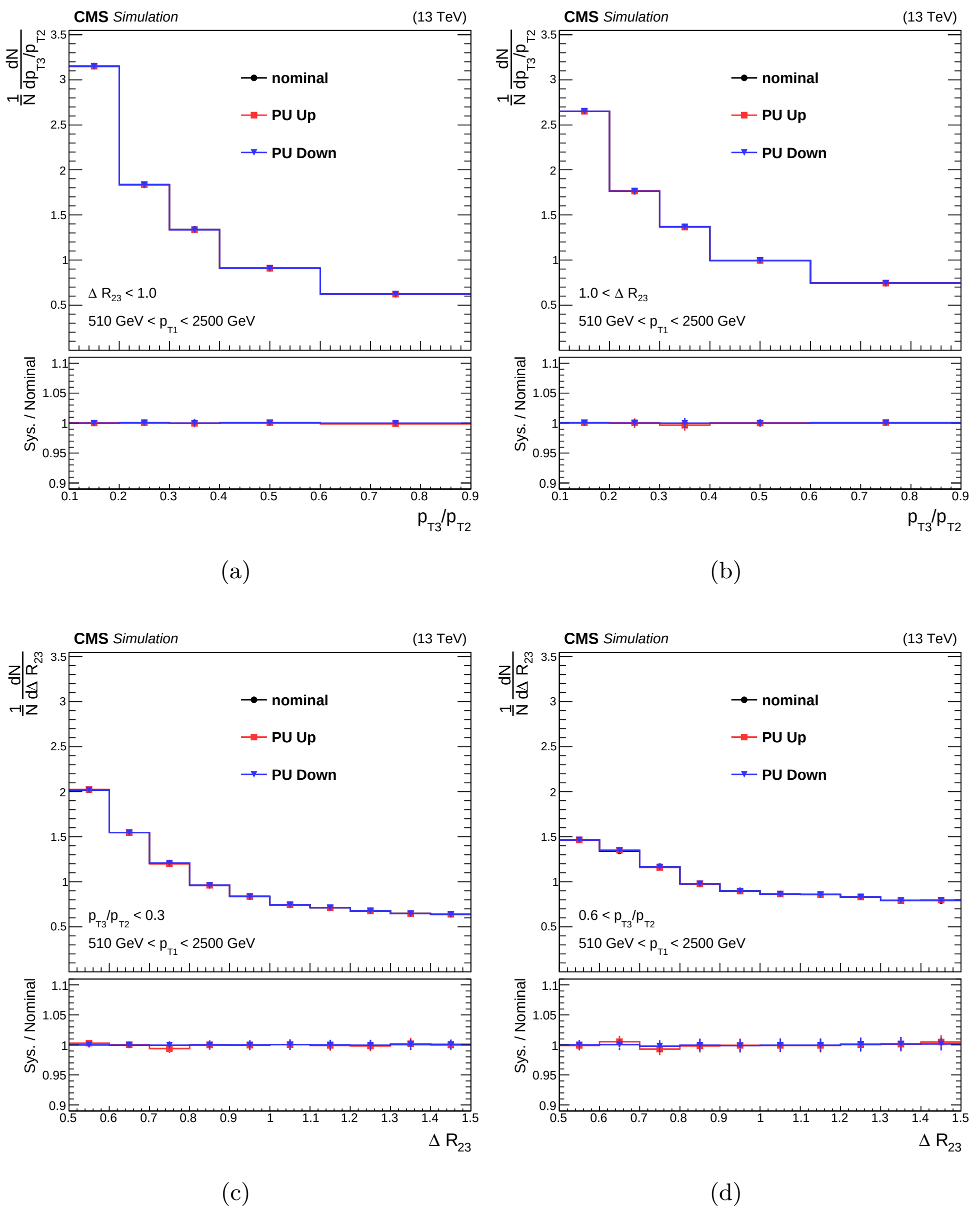

Figure 6.6: $\sqrt{s} = 13$ TeV PU systematic uncertainty. (a) p_{T3}/p_{T2} distribution for the events with a small angle radiation ($\Delta R_{23} < 1.0$), (b) p_{T3}/p_{T2} distribution for the events with a large angle radiation ($\Delta R_{23} > 1.0$), (c) ΔR_{23} distribution for soft p_T radiation case ($p_{T3}/p_{T2} < 0.3$), (d) ΔR_{23} distribution for hard p_T radiation case ($p_{T3}/p_{T2} > 0.6$).

6.4 Physics Model

The physics model (MOD) uncertainty is dependent on the unfolding response matrix. The MOD uncertainty considers two different physics model (pythia 8 and MadGraph) for building response matrix. The MOD uncertainty is estimated by the difference between the average value of two model unfolding results and maximum or minimum value. Figure 6.7-6.8 shows MOD uncertainty.

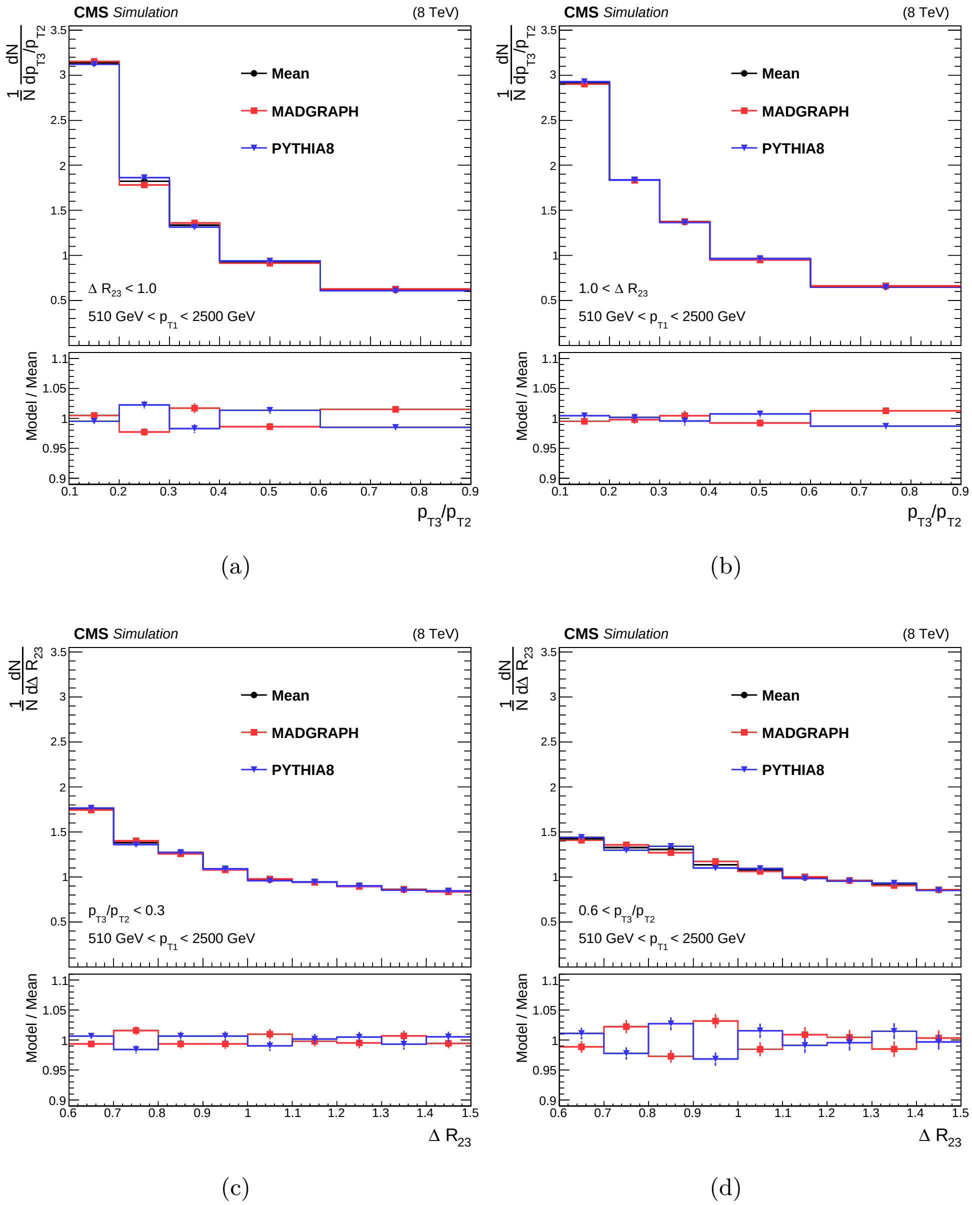

Figure 6.7: $\sqrt{s} = 8$ TeV MOD systematic uncertainty. (a) $p_{\mathrm{T}3}/p_{\mathrm{T}2}$ distribution for the events with a small angle radiation ($\Delta R_{23} < 1.0$), (b) $p_{\mathrm{T}3}/p_{\mathrm{T}2}$ distribution for the events with a large angle radiation ($\Delta R_{23} > 1.0$), (c) ΔR_{23} distribution for soft p_{T} radiation case ($p_{\mathrm{T}3}/p_{\mathrm{T}2} < 0.3$), (d) ΔR_{23} distribution for hard p_{T} radiation case ($p_{\mathrm{T}3}/p_{\mathrm{T}2} > 0.6$).

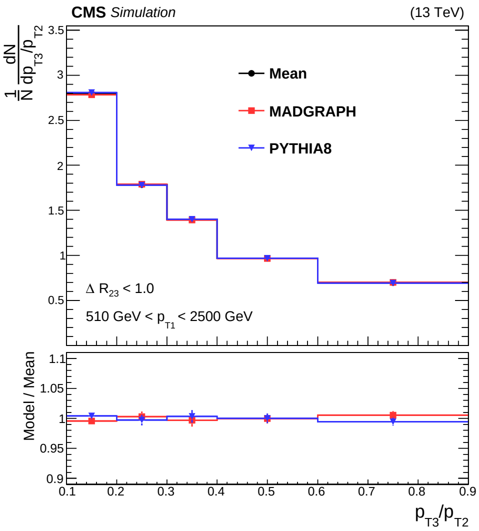

(a)

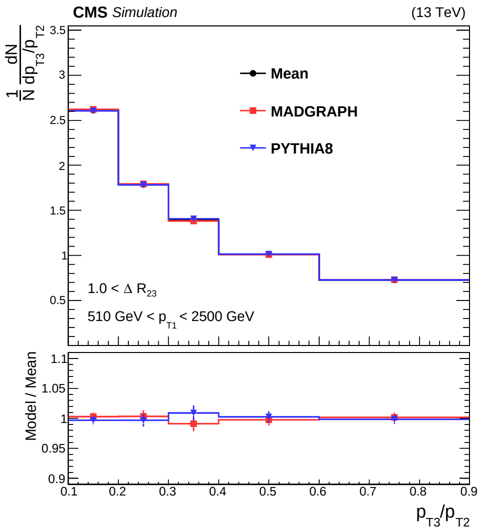

(b)

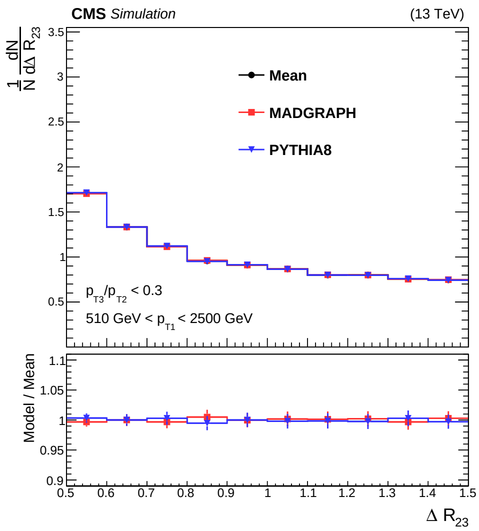

(c)

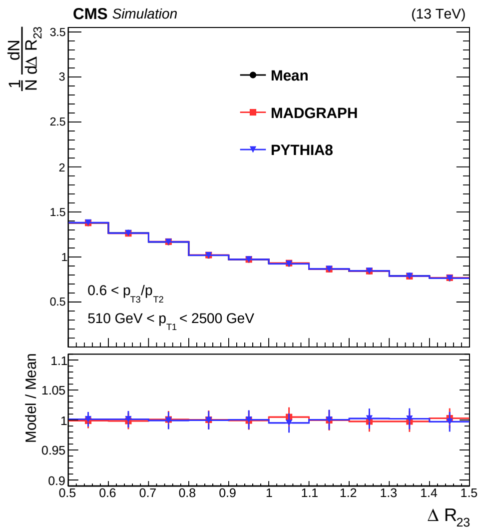

(d)

Figure 6.8: $\sqrt{s} = 13$ TeV MOD systematic uncertainty. (a) p_{T3}/p_{T2} distribution for the events with a small angle radiation ($\Delta R_{23} < 1.0$), (b) p_{T3}/p_{T2} distribution for the events with a large angle radiation ($\Delta R_{23} > 1.0$), (c) ΔR_{23} distribution for soft p_T radiation case ($p_{T3}/p_{T2} < 0.3$), (d) ΔR_{23} distribution for hard p_T radiation case ($p_{T3}/p_{T2} > 0.6$).

6.5 Unfolding Method

Since the unfolding results contain the unfolding algorithm characteristic, the systematic uncertainty should estimate the unfolding (UNFOLD) methods uncertainty. Two different unfolding methods (D'Agostini and SVD) are introduced To estimate the UNFOLD uncertainty. The difference between the average value of the two unfolding method results and maximum or minimum value shows the UNFOLD uncertainty effect. Figure 6.9-6.10 show the UNFOLD systematic.

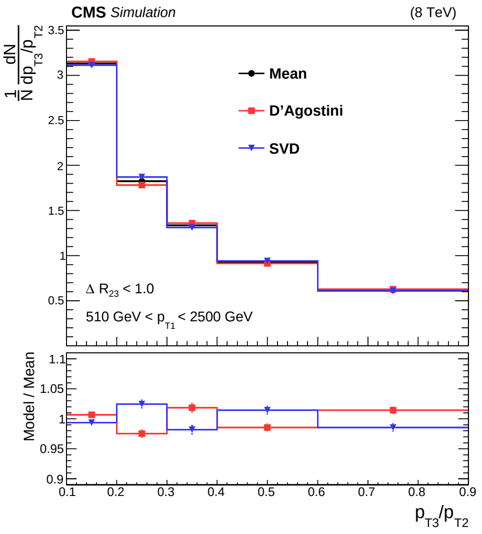

(a)

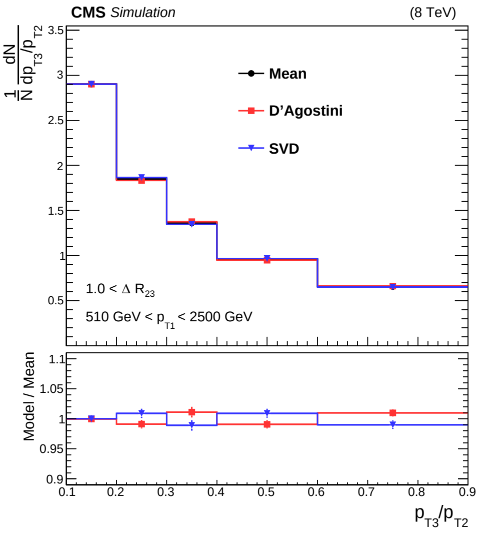

(b)

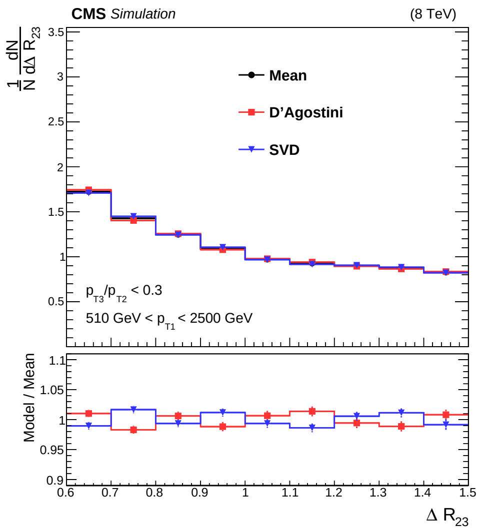

(c)

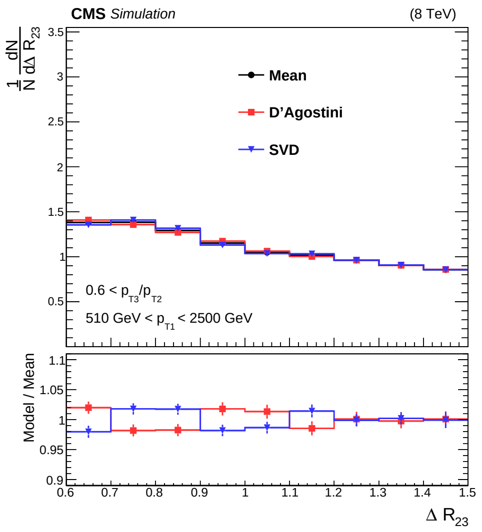

(d)

Figure 6.9: $\sqrt{s} = 8$ TeV UNFOLD systematic uncertainty. (a) p_{T3}/p_{T2} distribution for the events with a small angle radiation ($\Delta R_{23} < 1.0$), (b) p_{T3}/p_{T2} distribution for the events with a large angle radiation ($\Delta R_{23} > 1.0$), (c) ΔR_{23} distribution for soft p_T radiation case ($p_{T3}/p_{T2} < 0.3$), (d) ΔR_{23} distribution for hard p_T radiation case ($p_{T3}/p_{T2} > 0.6$).

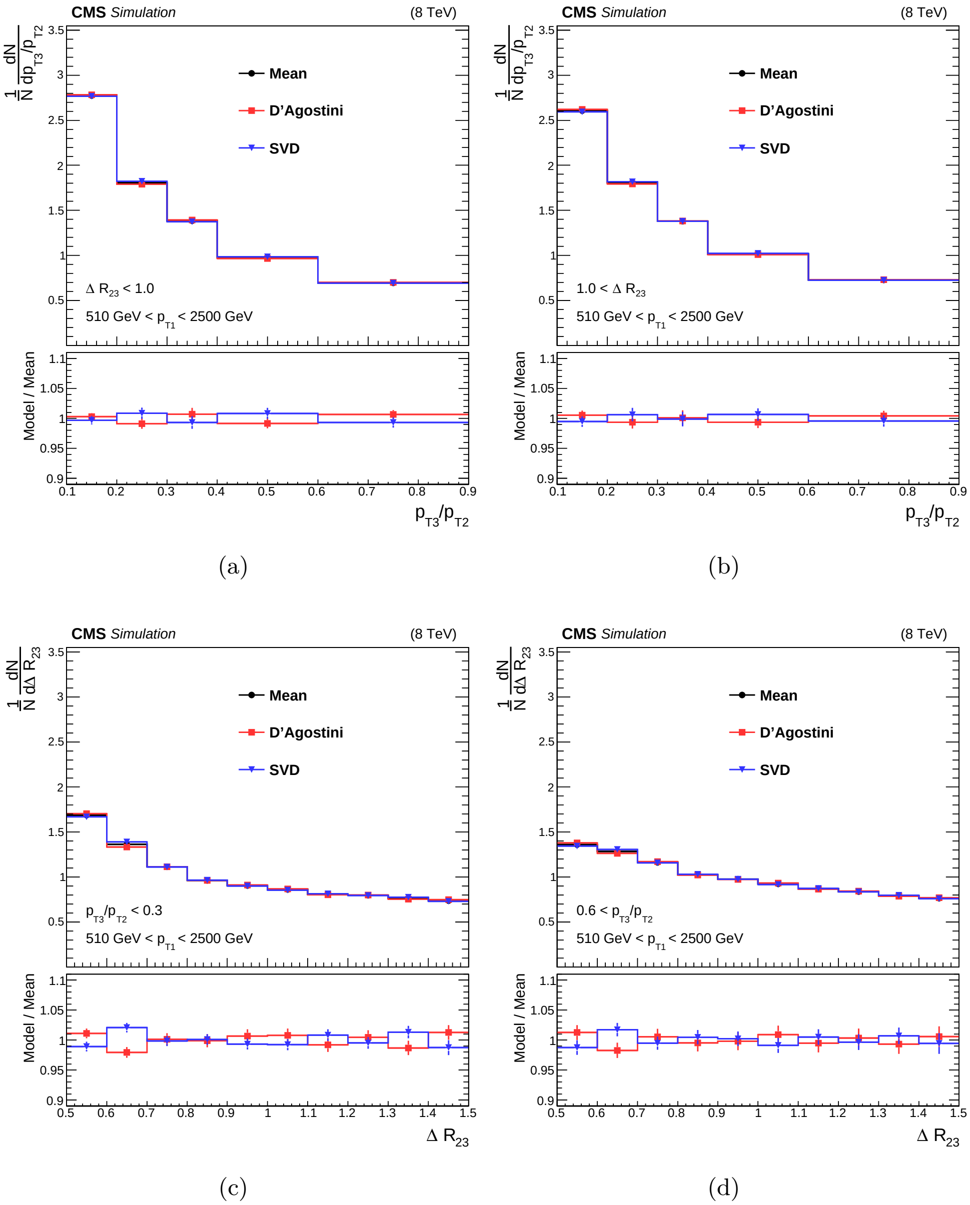

Figure 6.10: $\sqrt{s} = 13$ TeV UNFOLD systematic uncertainty. (a) p_{T3}/p_{T2} distribution for the events with a small angle radiation ($\Delta R_{23} < 1.0$), (b) p_{T3}/p_{T2} distribution for the events with a large angle radiation ($\Delta R_{23} > 1.0$), (c) ΔR_{23} distribution for soft p_T radiation case ($p_{T3}/p_{T2} < 0.3$), (d) ΔR_{23} distribution for hard p_T radiation case ($p_{T3}/p_{T2} > 0.6$).

6.6 Summary of Systemic Uncertainties

Systematic uncertainties from the JES, JER, PU, MOD, and UNFOLD are estimated. Each systematic uncertainty is quoted as the maximum variation from the fluctuations due to the corresponding systematic effect. The systematic uncertainty from JES is found to be 0.15 % (0.24 % for $\sqrt{s} = 13$ TeV). Since the JER observed in data differs from that obtained from simulation, MC jets are smeared to get the same resolution as in data. Then, the systematic uncertainty is estimated to be 0.16 % (0.12 % for $\sqrt{s} = 13$ TeV) by varying the JER up and down by 1 standard deviation. To study the impact from PU, the number of PU events in the simulation is varied by shifting the min-bias cross section $\pm 5\%$. The PU uncertainty is estimated to be 0.1 % (0.17 % for $\sqrt{s} = 13$ TeV). The MOD dependence for unfolding is estimated using two MC samples. Both MADGRAPH and PYTHIA 8 samples are used to derive the response matrices, and both samples are unfolded. The mean of both unfolded data is used as the nominal values. The MOD uncertainty is found to be about 1.1 % (0.25 % for $\sqrt{s} = 13$ TeV), which is half of the variances of data points found by switching the response matrices between PYTHIA and MADGRAPH. The UNFOLD uncertainty is found to be about 1.12 % (0.72 % for $\sqrt{s} = 13$ TeV), which is the half of the deviations of data points found by changing the unfolding method among D'Agostini and SVD. In both MOD and UNFOLD studies, the systematic uncertainties in the $\sqrt{s} = 8$ TeV results are significantly larger than those of the $\sqrt{s} = 13$ TeV. The main difference appears to be the use of PYTHIA 8 versus PYTHIA 6 for the MadGraph matching in MadGraph, as we use PYTHIA 6 for $\sqrt{s} = 8$ TeV while we use PYTHIA 8 for $\sqrt{s} = 13$ TeV.

The table 6.2-6.3 show summary of systematic uncertainties and the figure 6.11-6.12 show their distributions.

Table 6.2: $\sqrt{s} = 8\,\text{TeV}$ Summary of systematic uncertainties

	p_{T3}/p_{T2} distribution				ΔR_{23} distribution			
	$\Delta R_{23} < 1.0$		$1.0 < \Delta R_{23}$		$p_{T3}/p_{T2} < 0.3$		$0.6 < p_{T3}/p_{T2}$	
Uncertainty	range	average	range	average	range	average	range	average
JES	0.07 - 0.14 %	0.10 %	0.03 - 0.18 %	0.12 %	0.03 - 0.23 %	0.13 %	0.11 - 0.33 %	0.22 %
JER	0.09 - 0.32 %	0.20 %	0.03 - 0.28 %	0.17 %	0.08 - 0.27 %	0.14 %	0.02 - 0.36 %	0.15 %
PU	0.03 - 0.17 %	0.07 %	0.00 - 0.10 %	0.04 %	0.02 - 0.21 %	0.12 %	0.04 - 0.28 %	0.14 %
MOD	0.50 - 2.25 %	1.47 %	0.18 - 1.29 %	0.62 %	0.19 - 1.58 %	0.71 %	0.33 - 3.18 %	1.55 %
UNFOLD	0.65 - 2.46 %	1.56 %	0.01 - 1.09 %	0.78 %	0.56 - 1.68 %	1.01 %	0.09 - 2.01 %	1.17 %
SYS	0.83 - 3.35 %	2.16 %	0.55 - 1.63 %	1.11 %	0.79 - 2.31 %	1.29 %	0.49 - 3.67 %	2.07 %
STA	0.29 - 0.58 %	0.44 %	0.32 - 0.62 %	0.46 %	0.40 - 0.65 %	0.57 %	0.69 - 0.93 %	0.83 %
Sys. + Sta.	0.88 - 3.38 %	2.21 %	0.63 - 1.68 %	1.21 %	1.02 - 2.36 %	1.43 %	1.02 - 3.76 %	2.29 %

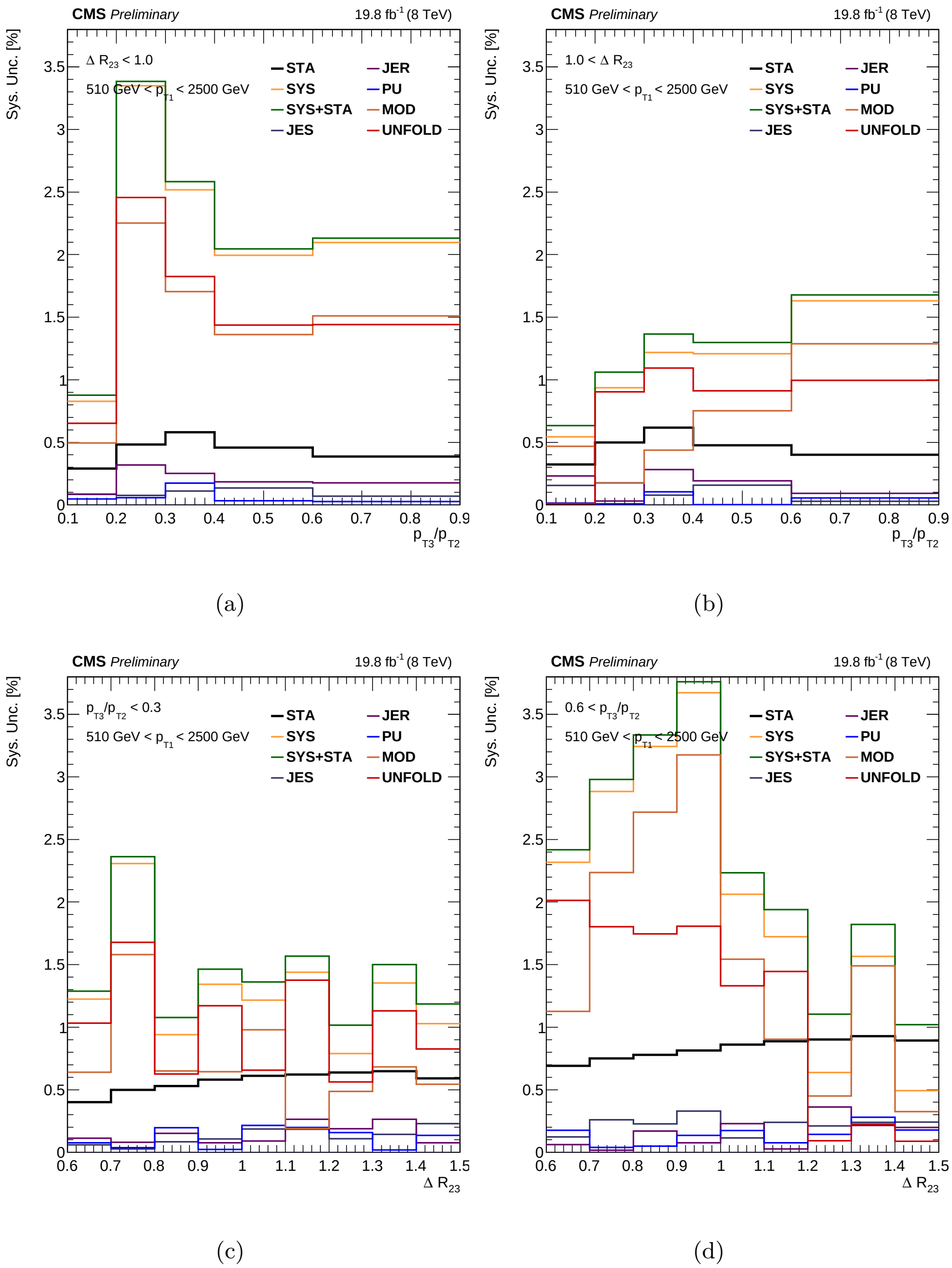

Figure 6.11: $\sqrt{s} = 8$ TeV the summary of systematic uncertainties. (a) p_{T3}/p_{T2} distribution for the events with a small angle radiation ($\Delta R_{23} < 1.0$), (b) p_{T3}/p_{T2} distribution for the events with a large angle radiation ($\Delta R_{23} > 1.0$), (c) ΔR_{23} distribution for soft p_T radiation case ($p_{T3}/p_{T2} < 0.3$), (d) ΔR_{23} distribution for hard p_T radiation case ($p_{T3}/p_{T2} > 0.6$).

Table 6.3: $\sqrt{s} = 13\,\text{TeV}$ Summary of systematic uncertainties

	p_{T3}/p_{T2} distribution				ΔR_{23} distribution			
	$\Delta R_{23} < 1.0$		$1.0 < \Delta R_{23}$		$p_{T3}/p_{T2} < 0.3$		$0.6 < p_{T3}/p_{T2}$	
Uncertainty	range	average	range	average	range	average	range	average
JES	0.15 - 0.39 %	0.26 %	0.14 - 0.58 %	0.25 %	0.05 - 0.42 %	0.19 %	0.16 - 0.52 %	0.29 %
JER	0.04 - 0.22 %	0.13 %	0.09 - 0.28 %	0.17 %	0.02 - 0.17 %	0.09 %	0.07 - 0.21 %	0.12 %
PU	0.02 - 0.12 %	0.06 %	0.03 - 0.36 %	0.12 %	0.01 - 0.61 %	0.17 %	0.05 - 0.66 %	0.25 %
MOD	0.01 - 0.54 %	0.32 %	0.17 - 0.89 %	0.39 %	0.00 - 0.51 %	0.23 %	0.05 - 0.49 %	0.18 %
UNFOLD	0.30 - 0.87 %	0.68 %	0.11 - 0.65 %	0.47 %	0.11 - 2.08 %	0.88 %	0.21 - 1.72 %	0.72 %
SYS	0.59 - 0.97 %	0.84 %	0.49 - 1.13 %	0.76 %	0.61 - 2.08 %	1.04 %	0.37 - 1.89 %	0.89 %
STA	0.39 - 0.74 %	0.56 %	0.49 - 0.89 %	0.66 %	0.55 - 0.93 %	0.82 %	0.87 - 1.24 %	1.10 %
Sys. + Sta.	0.71 - 1.16 %	1.01 %	0.74 - 1.44 %	1.01 %	1.05 - 2.20 %	1.35 %	1.18 - 2.13 %	1.46 %

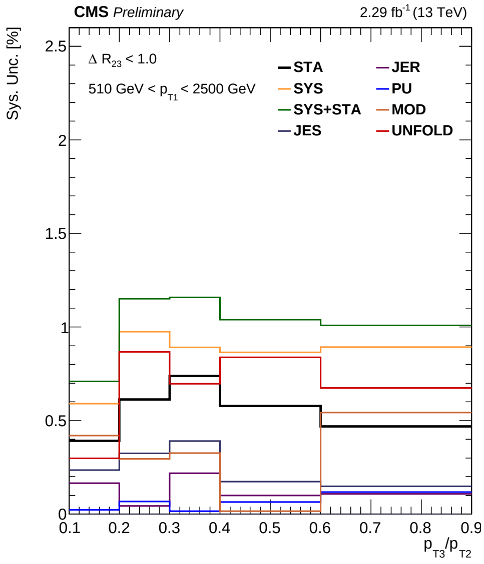

(a)

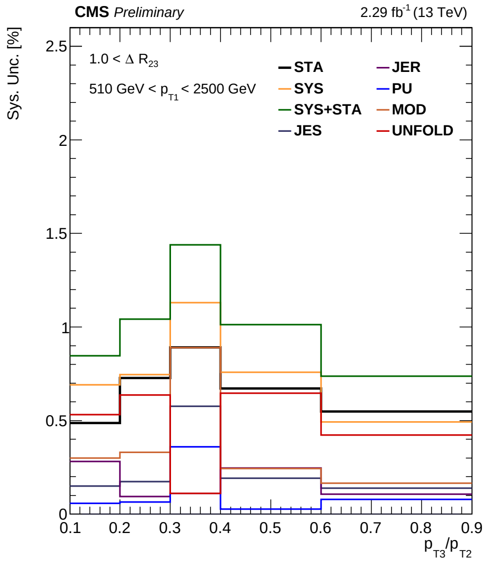

(b)

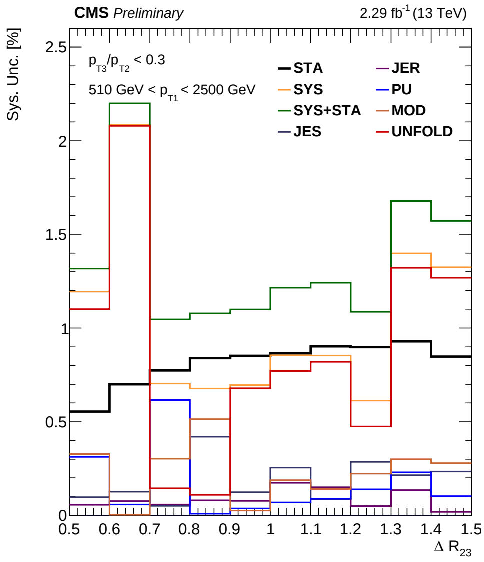

(c)

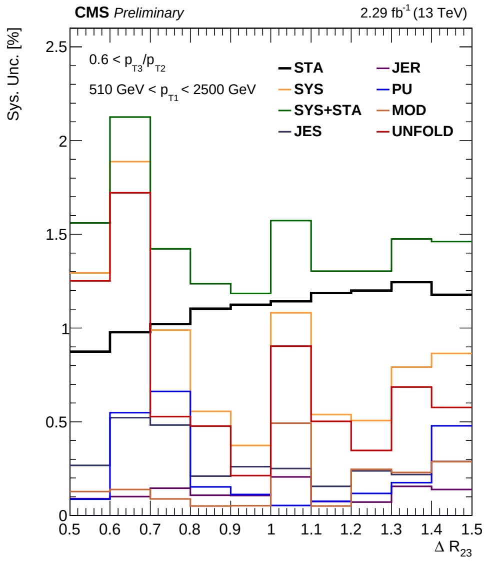

(d)

Figure 6.12: $\sqrt{s} = 13$ TeV the summary of systematic uncertainties. (a) p_{T3}/p_{T2} distribution for the events with a small angle radiation ($\Delta R_{23} < 1.0$), (b) p_{T3}/p_{T2} distribution for the events with a large angle radiation ($\Delta R_{23} > 1.0$), (c) ΔR_{23} distribution for soft p_T radiation case ($p_{T3}/p_{T2} < 0.3$), (d) ΔR_{23} distribution for hard p_T radiation case ($p_{T3}/p_{T2} > 0.6$).

7 Results

7.1 Theoretical prediction

Three Monte Carlo (MC) generators, PYTHIA 8 [26], POWHEG [29, 30, 31], and MadGraph [28] are used for the theoretical predictions. PYTHIA 8 (version 8.212) generates hard QCD processes using leading order (LO) $2 \to 2$ ME. POWHEG (version 2) generates hard QCD processes using next-to-leading order (NLO) $2 \to 2$ ME, i.e. order α_s^3 accuracy. MadGraph (version 5.2.4) generates hard QCD processes using LO $2 \to 2{+}3{+}4$ ME with a jet matching scale $Q_{\mathrm{cut}} = 14$ GeV. Both POWHEG and MadGraph use PYTHIA 8 for subsequent event evolution beyond the hard process. A CMS specific tune CUETP8M1 [27] is used with PYTHIA 8.

7.2 Comparison of data and predictions

We compare the $p_{\mathrm{T3}}/p_{\mathrm{T2}}$ distributions of data with predictions for the events with small angle radiation ($\Delta R_{23} < 1.0$) and separately for the events with large angle radiation ($\Delta R_{23} > 1.0$). We also compare the ΔR_{23} distributions of data with predictions for the events with a soft p_{T} radiation ($p_{\mathrm{T3}}/p_{\mathrm{T2}} < 0.3$) and for the events with a hard p_{T} radiation ($p_{\mathrm{T3}}/p_{\mathrm{T2}} > 0.6$). The events with $0.3 < p_{\mathrm{T3}}/p_{\mathrm{T2}} < 0.6$ are not used in the comparisons as we only want to see the effects in both limits, i.e., soft p_{T} and hard p_{T} radiation limits. This classification is summarized in Table 7.1 within the phase space defined as in table 4.12.

Criteria	Radiation type
$p_{\mathrm{T3}}/p_{\mathrm{T2}} < 0.3$	soft p_{T} radiation
$p_{\mathrm{T3}}/p_{\mathrm{T2}} > 0.6$	hard p_{T} radiation
$\Delta R_{23} < 1.0$	small angle radiation
$\Delta R_{23} > 1.0$	large angle radiation

Table 7.1: event classification according to the radiation type

The figure 7.1 (a) shows the $p_{\mathrm{T3}}/p_{\mathrm{T2}}$ for the small ΔR_{23} region. All theoretical predictions show significant deviations from the measurements. Interestingly, LO4jets+PS distribution shows an opposite behave when it compared with LO2jets+PS and NLO2jets+PS . We observe that the best description is given by calculations which include PS. In the figure 7.1 (b) the $p_{\mathrm{T3}}/p_{\mathrm{T2}}$ distribution is shown for large ΔR_{23}. This region of phase space is well described by LO4jets+PS calculations, while LO2jets+PS and NLO2jets+PS show large deviations from the measurements.

In the figure 7.1 (c, d) the ΔR_{23} distribution is shown for two regions of p_{T3}/p_{T2}. The figure 7.1 (c) shows the distribution for the small p_{T3}/p_{T2} region. The predictions from LO2jets+PS and NLO2jets+PS describe the measurement well, while the prediction from LO4jets+PS shows relatively larger deviations from the data. In the figure 7.1 (d) the ΔR_{23} distribution is shown for the large p_{T3}/p_{T2} region. The distribution of data is rather flat. In contrast to the figure 7.1 (c), the predictions LO2jets+PS shows a different shape compared to the measurement, while the predictions NLO2jets+PS and LO4jets+PS describe the measurement well. This indicates that in this region the contribution from higher order ME calculations supplemented with PS is necessary.

The same comparisons are performed for the $\sqrt{s} = 13$ TeV data with the corresponding MC samples and the results are shown in the figure 7.2. As one can easily see by comparing the figure 7.1 to the figure 7.2, there are no significant differences between the distributions from $\sqrt{s} = 8$ TeV and the ones from $\sqrt{s} = 13$ TeV.

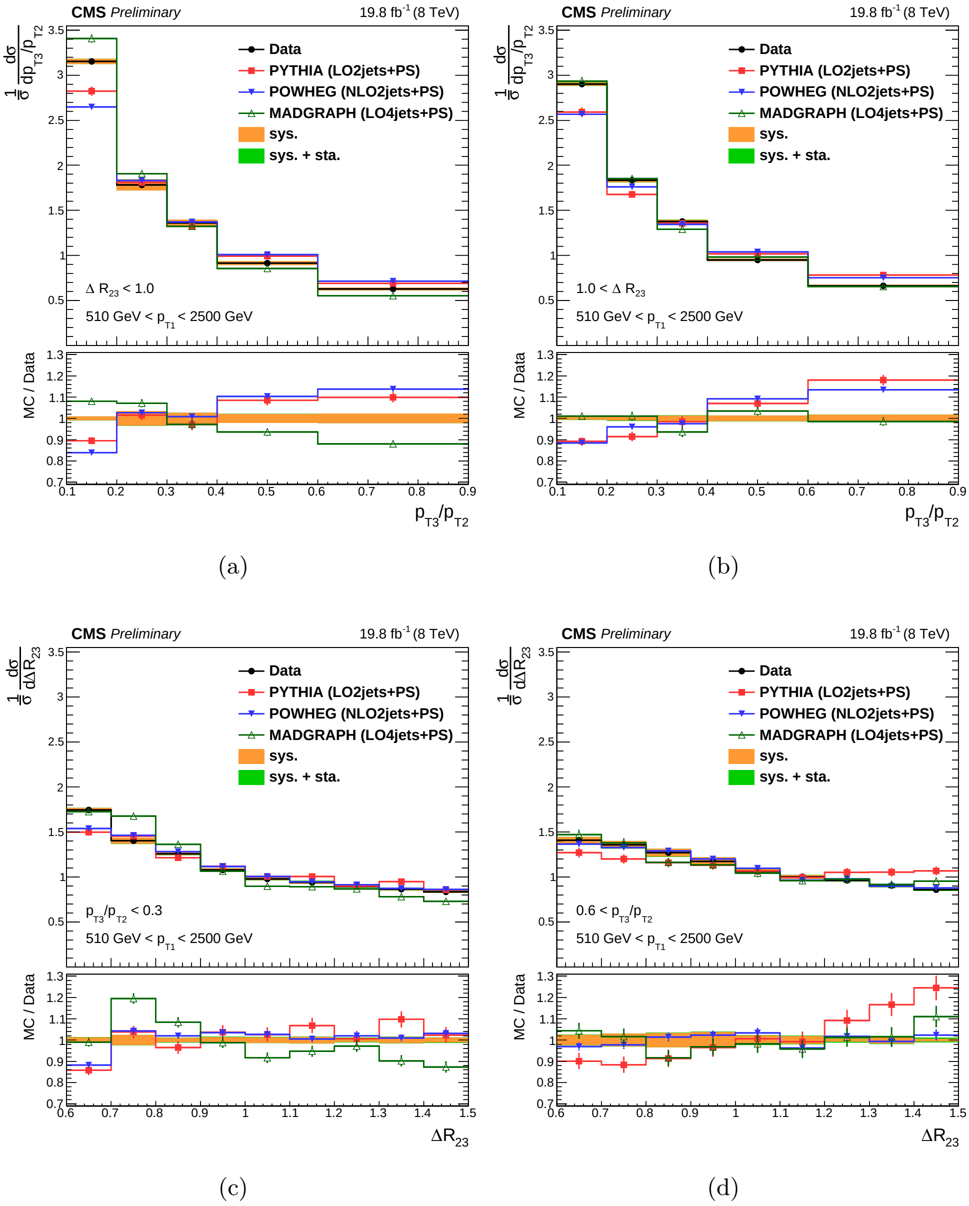

Figure 7.1: $\sqrt{s}$ = 8 TeV data and theoretical predictions comparisons. (a) $p_{\mathrm{T3}}/p_{\mathrm{T2}}$ distribution for the events with a small angle radiation ($\Delta R_{23} < 1.0$), (b) $p_{\mathrm{T3}}/p_{\mathrm{T2}}$ distribution for the events with a large angle radiation ($\Delta R_{23} > 1.0$), (c) ΔR_{23} distribution for soft p_{T} radiation case ($p_{\mathrm{T3}}/p_{\mathrm{T2}} < 0.3$), (d) ΔR_{23} distribution for hard p_{T} radiation case ($p_{\mathrm{T3}}/p_{\mathrm{T2}} > 0.6$).

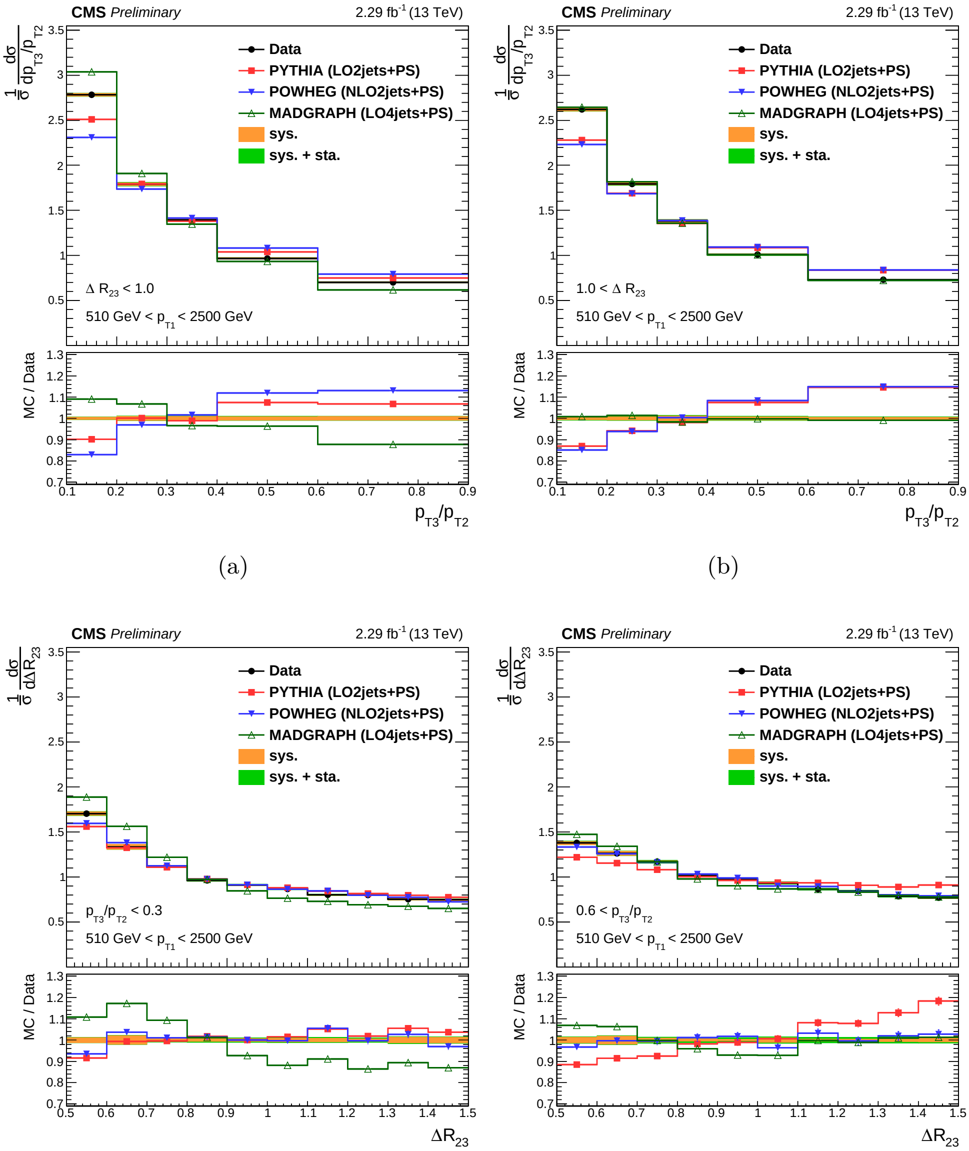

Figure 7.2: $\sqrt{s} = 13$ TeV data and theoretical predictions comparisons. (a) $p_{\mathrm{T3}}/p_{\mathrm{T2}}$ distribution for the events with a small angle radiation ($\Delta R_{23} < 1.0$), (b) $p_{\mathrm{T3}}/p_{\mathrm{T2}}$ distribution for the events with a large angle radiation ($\Delta R_{23} > 1.0$), (c) ΔR_{23} distribution for soft p_{T} radiation case ($p_{\mathrm{T3}}/p_{\mathrm{T2}} < 0.3$), (d) ΔR_{23} distribution for hard p_{T} radiation case ($p_{\mathrm{T3}}/p_{\mathrm{T2}} > 0.6$).

7.3 Chi-Square Fitting

The χ^2 between the experimental measurement and the theoretical predictions are investigated in the PS and the ME dominant regions for the comparison of the data and the various MC generators. In this study, the comparison of the χ^2 values between theoretical predictions has the statistical problem. Figures 7.3 - 7.4 show the fractional statistical uncertainties of data and theoretical predictions. Each theoretical predictions does not have the equivalent statistical uncertainties. This statistical problem leads to an incorrect χ^2 comparison between theoretical predictions. However, the χ^2 values are helpful for the comparison of the theoretical prediction performance between the PS and the ME dominant regions.

- $\chi^2 = M^T C^{-1} M$
- $M_i = (Data_i - MC_i)$
- $C = \mathrm{Cov}^{\mathrm{STA}} + \mathrm{Cov}^{\mathrm{JEC}} + \mathrm{Cov}^{\mathrm{JER}} + \mathrm{Cov}^{\mathrm{PU}} + \mathrm{Cov}^{\mathrm{MOD}} + \mathrm{Cov}^{\mathrm{UNFOLD}} + \mathrm{Cov}^{\mathrm{STA\ MC}}$

Table 7.2: Summary of χ^2/NDF for $\sqrt{s} = 8\,\mathrm{TeV}$

	$p_{\mathrm{T3}}/p_{\mathrm{T2}}$ distribution		ΔR_{23} distribution	
	$\Delta R_{23} < 1.0$	$1.0 < \Delta R_{23}$	$p_{\mathrm{T3}}/p_{\mathrm{T2}} < 0.3$	$0.6 < p_{\mathrm{T3}}/p_{\mathrm{T2}}$
PYTHIA (LO2jets+PS)	1.76	3.29	1.28	2.23
POWHEG (NLO2jets+PS)	4.18	2.86	0.80	0.18
MADGRAPH (LO4jets+PS)	2.05	0.32	2.29	0.54

Table 7.3: Summary of χ^2/NDF for $\sqrt{s} = 13\,\mathrm{TeV}$

	$p_{\mathrm{T3}}/p_{\mathrm{T2}}$ distribution		ΔR_{23} distribution	
	$dr < 1.0$	$1.0 < \Delta R_{23}$	$p_{\mathrm{T3}}/p_{\mathrm{T2}} < 0.3$	$0.6 < p_{\mathrm{T3}}/p_{\mathrm{T2}}$
PYTHIA (LO2jets+PS)	96.45	132.07	26.60	34.89
POWHEG (NLO2jets+PS)	172.86	97.73	6.35	1.38
MADGRAPH (LO4jets+PS)	131.35	1.57	197.21	15.21

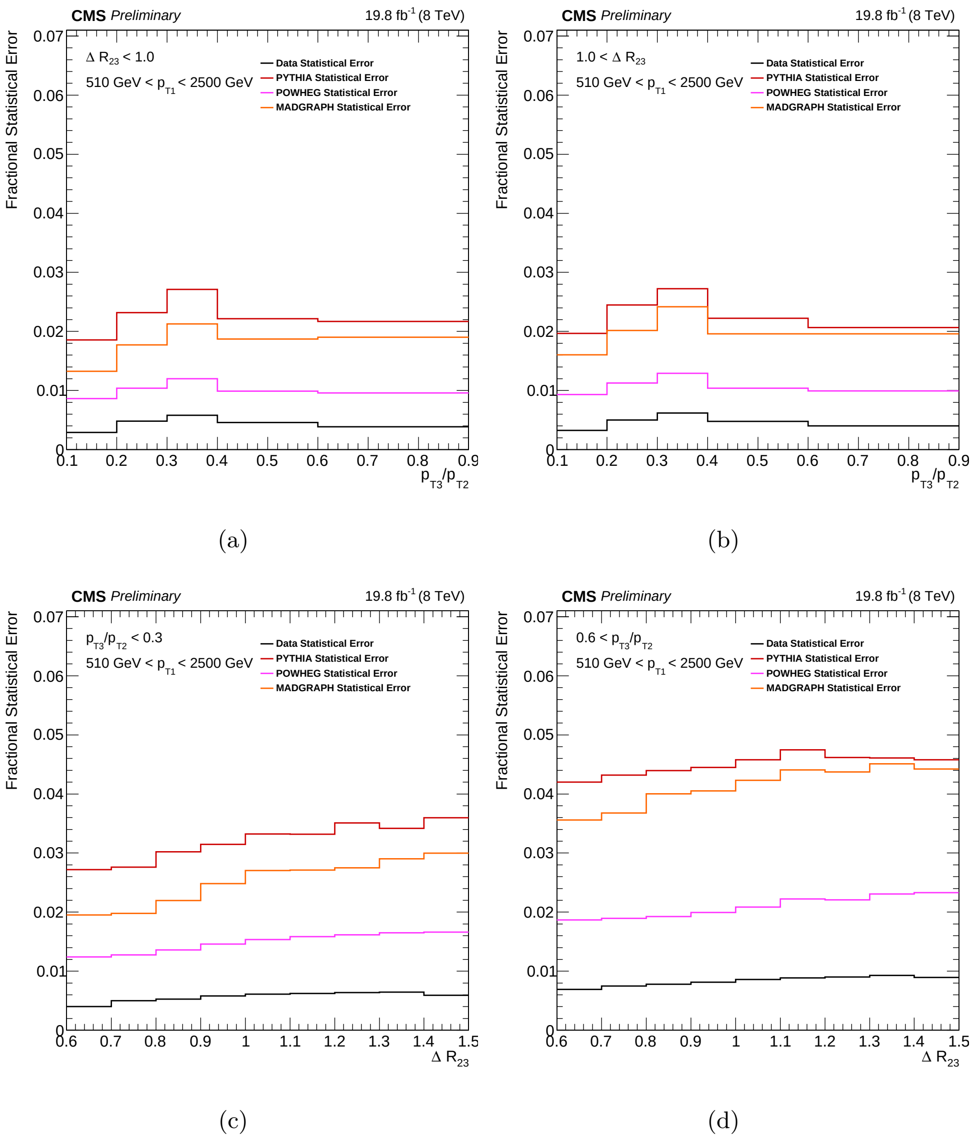

Figure 7.3: $\sqrt{s} = 8$ TeV the fractional statistical error of MC. (a) p_{T3}/p_{T2} distribution for the events with a small angle radiation ($\Delta R_{23} < 1.0$), (b) p_{T3}/p_{T2} distribution for the events with a large angle radiation ($\Delta R_{23} > 1.0$), (c) ΔR_{23} distribution for soft p_T radiation case ($p_{T3}/p_{T2} < 0.3$), (d) ΔR_{23} distribution for hard p_T radiation case ($p_{T3}/p_{T2} > 0.6$).

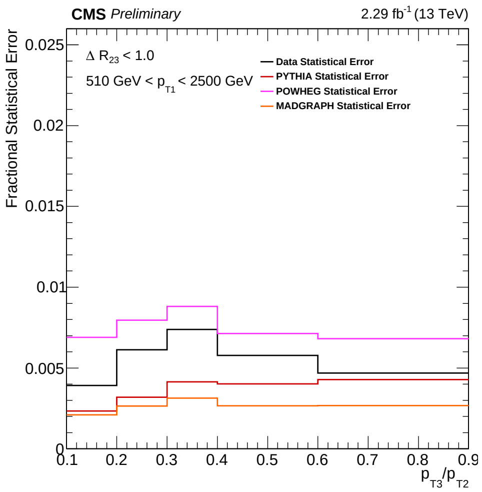

(a)

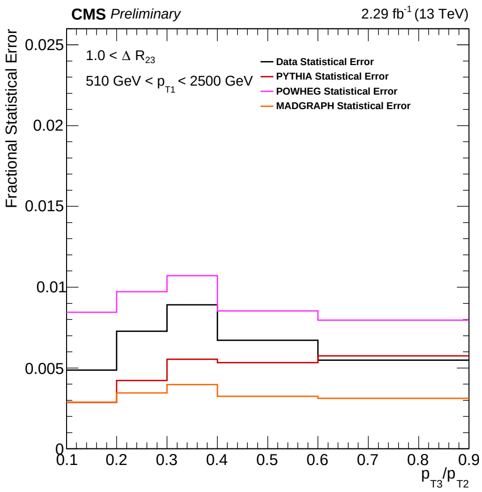

(b)

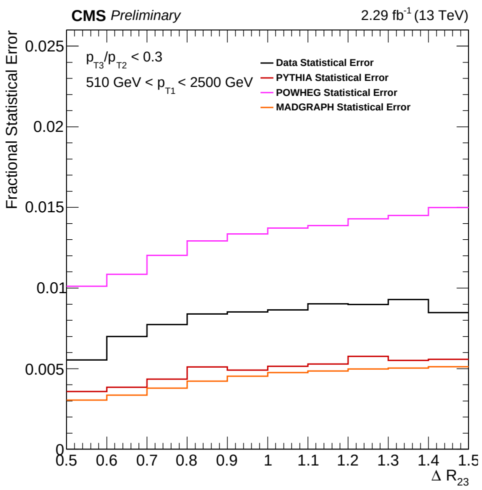

(c)

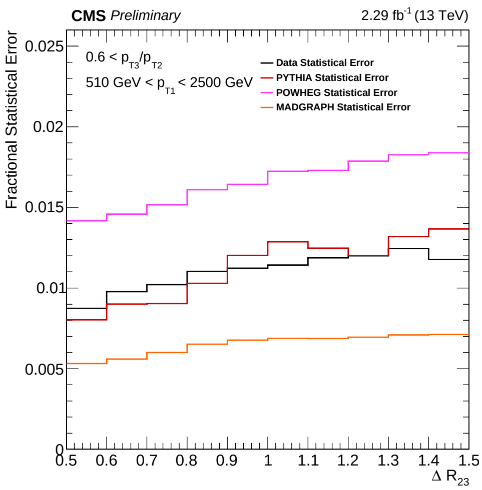

(d)

Figure 7.4: $\sqrt{s} = 13$ TeV the fractional statistical error of MC. (a) $p_{\mathrm{T3}}/p_{\mathrm{T2}}$ distribution for the events with a small angle radiation ($\Delta R_{23} < 1.0$), (b) $p_{\mathrm{T3}}/p_{\mathrm{T2}}$ distribution for the events with a large angle radiation ($\Delta R_{23} > 1.0$), (c) ΔR_{23} distribution for soft p_{T} radiation case ($p_{\mathrm{T3}}/p_{\mathrm{T2}} < 0.3$), (d) ΔR_{23} distribution for hard p_{T} radiation case ($p_{\mathrm{T3}}/p_{\mathrm{T2}} > 0.6$).

8 Summary and Conclusions

Two kinematic variables that are sensitive to the phase space of multi-jet final state are introduced. Events with three or more energetic jets are selected and the momenta and the angular separations between jets are measured. The variable p_{T3}/p_{T2} is used as a measure to distinguish between the soft and the hard p_T radiations. Another variable ΔR_{23} is adopted to classify events into the small angle and the large angle radiation types. We then compare the distributions of these two variables from the data with the ones from several different theoretical predictions. The integrated luminosity of 19.8 fb^{-1} at $\sqrt{s} = 8\,\text{TeV}$ data and the integrated luminosity of 2.29 fb^{-1} at $\sqrt{s} = 13\,\text{TeV}$ data, taken by CMS in 2012 and 2015 respectively, are used in the analysis. PYTHIA 8, MADGRAPH, and POWHEG are used to generate multi-jet events for the comparisons. No significant collision energy dependence is found. By comparisons with various theoretical predictions, we see the combinational use of the ME and the PS methods is crucial to describe the momentum and the angular distributions in data.

The $p_{\mathrm{T3}}/p_{\mathrm{T2}}$ distribution was compared to the theoretical predictions at large and small angle radiation region. At the small angle radiation region, the MadGraph behavior is opposite to pythia and powheg, and all predictions fail significantly. The pythia and the powheg resummation calculation need to improve in both region. At the large angle radiation region, the MadGraph is in good agreement with data. It shows the MadGraph based on ME method is entirely valid at well-separated parton calculations. The comparison of the ΔR_{23} distribution with the predictions is performed at soft and hard p_{T} radiation region. At the soft p_{T} radiation region, the pythia and the powheg show a good description of the ΔR_{23} distribution with the angular ordering shower method, and primarily the powheg describes the data well at the hard p_{T} radiation region. At the hard p_{T} radiation region, the MadGraph shows better performance than the soft p_{T} radiation region and pythia did not describe the data as well as the soft p_{T} radiation region. It shows the pythia based on PS method is fully valid at soft p_{T} radiation region and the MadGraph is quite valid at hard p_{T} radiation region. The powheg method of combining the parton shower has advantages compared to other methods.

The 3rd jet has strong correlations with 2nd jet because the 3rd jet is from FSR of the 2nd jet at dijet topology, and the 3rd jet is effected on color coherence. The correlations measurement of the 2nd jet and 3rd jet is an interesting tool to test theoretical predictions of multijet final states. This study identified the region where PS and ME method describes a better measurement and shows that jet matching needs to improve at another phase space. This results measured new phase space observables, and it shows differences between the predictions at PS and ME dominant regions. The jet matching can be improved with these measurements. Also, it needs to look different Q^2 region to see scale effects. Finally, the PS and ME jet matching scale would be dramatically improved that ME and PS matching calculation well describes data in both regions.

Bibliography

[1] G. Luisoni and S. Marzani, "QCD resummation for hadronic final states," *J. Phys.*, vol. G42, no. 10, p. 103101, 2015.

[2] F. Abe *et al.*, "Evidence for color coherence in $p\bar{p}$ collisions at $\sqrt{s} = 1.8$ TeV," *Phys. Rev.*, vol. D50, pp. 5562–5579, 1994.

[3] T. Sjöstrand, "Introduction to event generators," July 2016.

[4] T. Sjöstrand, "Status and developments of event generators," *PoS*, vol. LHCP2016, p. 007, 2016.

[5] H. Aihara *et al.*, "Tests of models for quark and gluon fragmentation in e^+e^- annihilation $\sqrt{s} = 29$ GeV," *Z. Phys.*, vol. C28, p. 31, 1985.

[6] F. Marcastel, "CERN's Accelerator Complex. La chaîne des accélérateurs du CERN," Oct 2013. General Photo.

[7] C. Patrignani and P. D. Group, "Review of particle physics," *Chinese Physics C*, vol. 40, no. 10, p. 100001, 2016.

[8] F. Halzen and A. Martin, *Quarks and leptons: an introductory course in modern particle physics.* Wiley, 1984.

[9] J. J. T. M. F.R.S., “Xl. cathode rays,” *The London, Edinburgh, and Dublin Philosophical Magazine and Journal of Science*, vol. 44, no. 269, pp. 293–316, 1897.

[10] P. E. R. F.R.S., “Lxxix. the scattering of α and β particles by matter and the structure of the atom,” *The London, Edinburgh, and Dublin Philosophical Magazine and Journal of Science*, vol. 21, no. 125, pp. 669–688, 1911.

[11] M. E. Peskin and D. V. Schroeder, *An Introduction to quantum field theory.* Reading, USA: Addison-Wesley, 1995.

[12] P. W. Higgs, “Broken Symmetries and the Masses of Gauge Bosons,” *Phys. Rev. Lett.*, vol. 13, pp. 508–509, 1964.

[13] F. Englert and R. Brout, “Broken Symmetry and the Mass of Gauge Vector Mesons,” *Phys. Rev. Lett.*, vol. 13, pp. 321–323, 1964.

[14] G. S. Guralnik, C. R. Hagen, and T. W. B. Kibble, “Global Conservation Laws and Massless Particles,” *Phys. Rev. Lett.*, vol. 13, pp. 585–587, 1964.

[15] A. Bettini, *Introduction to elementary particle physics.* Cambridge: Cambridge Univ. Press, 2008.

[16] J. J. Sakurai and J. Napolitano, *Modern quantum mechanics; 2nd ed.* San Francisco, CA: Addison-Wesley, 2011.

[17] M. Kobayashi and T. Maskawa, "CP Violation in the Renormalizable Theory of Weak Interaction," *Prog. Theor. Phys.*, vol. 49, pp. 652–657, 1973.

[18] N. Cabibbo, "Unitary Symmetry and Leptonic Decays," *Phys. Rev. Lett.*, vol. 10, pp. 531–533, 1963.

[19] A. Chudakov, "On an ionization effect related to the observation of electron-positron pairs at very high energies," *Izv. Akad. Nauk SSSR, Ser. Fiz.*, vol. 19, p. 650, 1955.

[20] Y. Dokshitzer, *Basics of perturbative QCD.* Atlantica Séguier Frontières, 1991.

[21] H. Aihara *et al.*, "Comparison of the particle flow in $q\bar{q}g$ and $q\bar{q}\gamma$ events in e^+e^- annihilation," *Phys. Rev. Lett.*, vol. 57, p. 945, 1986.

[22] B. Abbott *et al.*, "Color coherent radiation in multijet events from $p\bar{p}$ collisions at $\sqrt{s} = 1.8$ TeV," *Phys. Lett.*, vol. B414, pp. 419–427, 1997.

[23] S. Chatrchyan *et al.*, “Probing color coherence effects in pp collisions at $\sqrt{s} = 7\,\mathrm{TeV}$,” *Eur. Phys. J.*, vol. C74, no. 6, p. 2901, 2014.

[24] H. Kim, J. S. H. Lee, and I. Park, “Monte Carlo updates on color coherence at 7 TeV,” *J. Korean Phys. Soc.*, vol. 70, no. 5, pp. 465–468, 2017.

[25] M. Cacciari, G. P. Salam, and G. Soyez, “The Anti-k(t) jet clustering algorithm,” *JHEP*, vol. 04, p. 063, 2008.

[26] T. Sjöstrand, S. Ask, J. R. Christiansen, R. Corke, N. Desai, P. Ilten, S. Mrenna, S. Prestel, C. O. Rasmussen, and P. Z. Skands, “An Introduction to PYTHIA 8.2,” *Comput. Phys. Commun.*, vol. 191, pp. 159–177, 2015.

[27] V. Khachatryan *et al.*, “Event generator tunes obtained from underlying event and multiparton scattering measurements,” *Eur. Phys. J.*, vol. C76, no. 3, p. 155, 2016.

[28] J. Alwall, M. Herquet, F. Maltoni, O. Mattelaer, and T. Stelzer, “MadGraph 5 : Going Beyond,” *JHEP*, vol. 06, p. 128, 2011.

[29] P. Nason, “A New method for combining NLO QCD with shower Monte Carlo algorithms,” *JHEP*, vol. 11, p. 040, 2004.

[30] S. Frixione, P. Nason, and C. Oleari, "Matching NLO QCD computations with Parton Shower simulations: the POWHEG method," *JHEP*, vol. 11, p. 070, 2007.

[31] S. Alioli, P. Nason, C. Oleari, and E. Re, "A general framework for implementing NLO calculations in shower Monte Carlo programs: the POWHEG BOX," *JHEP*, vol. 06, p. 043, 2010.

[32] L. Evans and P. Bryant, "LHC Machine," *JINST*, vol. 3, p. S08001, 2008.

[33] A. M. Sirunyan *et al.*, "Particle-flow reconstruction and global event description with the CMS detector," *JINST*, vol. 12, no. 10, p. P10003, 2017.

[34] V. Khachatryan *et al.*, "Jet energy scale and resolution in the CMS experiment in pp collisions at 8 TeV," *JINST*, vol. 12, p. P02014, 2017.

[35] S. Chatrchyan *et al.*, "The CMS experiment at the CERN LHC," *JINST*, vol. 3, p. S08004, 2008.

[36] M. Cacciari, G. P. Salam, and G. Soyez, "FastJet User Manual," *Eur. Phys. J.*, vol. C72, p. 1896, 2012.

[37] CMS Collaboration, "Particle-flow event reconstruction in CMS and performance for jets, taus, and $E_{\mathrm{T}}^{\mathrm{miss}}$," CMS Physics Analysis Summary CMS-PAS-PFT-09-001, 2009.

[38] CMS Collaboration, "Commissioning of the particle-flow event reconstruction with the first LHC collisions recorded in the CMS detector," CMS Physics Analysis Summary CMS-PAS-PFT-10-001, 2010.

[39] "Recommended jet energy corrections and uncertainties for data and mc," 2018-06-22 (accessed June 2018). https://twiki.cern.ch/twiki/bin/viewauth/CMS/JECDataMC.

[40] V. Khachatryan *et al.*, "The CMS trigger system," *JINST*, vol. 12, p. P01020, 2017.

[41] T. Adye, "Unfolding algorithms and tests using RooUnfold," in *Proceedings, PHYSTAT 2011 Workshop on Statistical Issues Related to Discovery Claims in Search Experiments and Unfolding, CERN,Geneva, Switzerland 17-20 January 2011*, (Geneva), pp. 313–318, CERN, CERN, 2011.

국문초록

김 현 용

서울시립대학교

대학원 물리학과

(지도교수 : 박 인 규)

거대 강입자 충돌실험에서 멀티 제트 사건을 선택하여 두 종류의 동역학 관측량을 관측하여 제트의 상관 관계를 연구했다. 세개 이상의 제트를 가진 사건을 이용하여, 세번 째 제트의 횡단면 운동량과 두번 째 제트의 횡단명 운동량의 비를 구했으며, 두번 째 제트와 세번 째 제트의 각 분포를 구했다. 측정량은 데이터와 이론 계산과 비교되었다. 측정은 19.8 fb^{-1} 과 2.29 fb^{-1} 의 데이터를 이용하였으며, 각각 중심에너지 8 TeV 와 13 TeV 가 CMS 검출기에서 측정되었다.

주요어휘: 거대 강입자 충돌기, 양자색소역학, 제트